University of Naples Federico II

Department of Industrial Engineering

Ph.D. Dissertation

Doctoral Program in Industrial Engineering

XXXV Cycle

Ph.D. Coordinator: Prof. Eng. Michele Grassi

MODEL-BASED APPROACH FOR MECHANICAL SYSTEM MONITORING

Ph.D. Candidate

Eng. Ciro Tordela

(DR993907)

Supervisors

Prof. Eng. Salvatore Strano

(University of Naples "Federico II")

Prof. Eng. Mario Terzo

(University of Naples "Federico II")

Reviewers

Ph.D. Eng. Pablo Camocardi

(University of Surrey, Guildford – ARRIVAL Ltd)

Prof. Eng. Ingo Kaiser

(Universidad Antonio de Nebrija, Madrid)

“I need a new voice, a new law,

a new way

Take the time, re-evaluate…”

(Dream Theater – Take the time)

Thanks

to the ones who believed in me.

Acknowledgments

At the end of this three-year Ph.D., I would like to sincerely thank my supervisors, Professors Salvatore Strano and Mario Terzo, for supporting, guiding, and always stimulating me to give my best.

Thanks to them, I have grown both professionally and humanely.

I thank my fellow travellers, colleagues, and friends from the Department of Industrial Engineering, especially Chiara Cosenza and Enrico Fornaro.

Finally, I would like to thank Pablo Camocardi, which allowed me to interface with new challenges during my stay in Germany at the ARRIVAL company, and Damiano Cozza for his valuable advice and support.

Ciro Tordela

Table of Contents

List of Figures

List of Tables

Abstract

The aim of the present Ph.D. thesis is the development of model-based estimators for monitoring mechanical systems. Complex systems have mechanical ones as components, and those latter are intrinsically complex. Indeed, the growth in technology allowed the transformation from purely mechanical systems to mechatronics ones with many advantages in terms of interfacing with other systems, the external environment, and humans. Unfortunately, higher maintenance of components integrated into new mechanical systems, typically subjected to degradation, is required. The possibility of introducing the condition-based approach to maintenance activities is crucial for avoiding early replacements of components in good functioning or late intervention on them in faulty conditions. Different techniques for monitoring mechanical systems in real-time can be employed for realizing the condition-based maintenance.

In this work, model-based estimators constituted of Kalman Filters are employed for monitoring three types of mechanical systems: the railway vehicle, the road vehicle, and Curved Surfaces Sliding Isolators. The monitoring through a model-based approach for each class of previously mentioned mechanical systems is described. Anti-yaw suspension components, which constitute a part of the railway secondary suspension, are monitored to identify possible faults that cause stability and safety reduction in railway vehicles. Two different modelling approaches are employed for monitoring the tire-road conditions of road vehicles and for managing their performances by estimating the sideslip angle. The frictional behaviour related to both surfaces of Curved Surfaces Sliding Isolators is characterized through the proposed model-based approach, which is also suitable for monitoring the wear conditions of isolators during their operations.

An overview of different possible approaches to the diagnostic and monitoring of mechanical and mechatronic systems, functional for condition-based maintenance, is provided. In particular, a detailed description of Kalman Filters, employed as a model-based monitoring technique in this work, is included. By starting from the linear Kalman Filter, nonlinear formulations of this latter, such as the Extended Kalman Filter and the Constrained Unscented Kalman Filter, are explained. Kalman Filters make estimations based on the mathematical modelling of the system to be monitored. For each mechanical system studied in this work, an estimator design model is developed to include it in a Kalman Filter for activating the estimation process and, therefore, the model-based monitoring. The correct design of the previously mentioned model is crucial for obtaining reliable estimations by Kalman Filters. Formulations of estimator design models able to capture desired dynamical behaviours of mechanical systems to be monitored are provided.

Finally, results concerning estimations provided by the proposed monitoring approach for each mechanical system analysed are provided. The estimated quantities are compared with detailed simulation models and with experimental data. The obtained results confirm the suitability of the model-based monitoring approach for mechanical systems, allowing for deepening future research on their applicability in hardware equipment integrated onboard the explored mechanical systems for making real-time condition monitoring.

1. MODEL-BASED MONITORING OF MECHANICAL SYSTEMS: CONTEXT OF APPLICATIONS

Nowadays, the possibility of employing condition-based maintenance strategies instead of predictive or calendarized ones is crucial for promptly taking action on mechanical systems subjected to faults. Furthermore, two different enhancements are obtainable at the same time through condition-based maintenance:

- *increasing in the economic efficiency* – the maintenance becomes more cost-efficient because the components are only maintained when necessary. Thereby, the replacement of system components which are still in a good state is avoided allowing money saving and introducing benefits in terms of conservation and protection of the environment;
- *increasing in the operational safety* – the possibility of detecting faults in system components in time allows making their maintenance or replacement before a failure with catastrophic consequences happens.

The condition-based maintenance allows the substitution and the repair of devices within a time horizon in which faults or abnormal behaviours are detected through condition monitoring systems. Typically, the two previously mentioned enhancements obtainable by employing condition-based maintenance conflict with each other considering that, in many cases, a reduction of the operational costs comes at the price of diminished safety.
Therefore, monitoring systems are required to detect anomalies in mechanical systems, at each time instant, for condition-based maintenance purposes and for harmonizing the two conflicting aspects related to the condition-based maintenance approach.
The main aim of condition monitoring is to ensure the reliability of mechanical systems and safety for users of monitored systems. Different approaches, such as Sensor-based and Data-driven ones, are employed to implement monitoring systems and tools in electronic control units.

The employability of the model-based approach on the condition monitoring of mechanical systems is explored in this work.

Model-based approaches for condition monitoring are suitable for real-time implementations and allow the estimation of operative parameters and state variables for the health condition monitoring of a mechanical system.

Through the model-based monitoring approach, the following features are obtainable:

- information on the presence of a fault or the excessive wear of the overall system or its particular element at each time instant;
- reduce the number of expensive sensors mounted on the mechanical system to be monitored, substituting the measurement signals with their estimations.

One of the most employed algorithms in model-based monitoring of mechanical systems is the Kalman Filter in its various forms. The model-based concept is the heart of Kalman Filters. The physical-mathematical model of the mechanical system to be monitored is required by Kalman Filters for obtaining desired estimations.

The main contribution of this work is the development of new Estimator Design Models to be included in Kalman Filters for monitoring purposes of mechanical systems. Therefore, methodologies to build Estimator Design Models are described.

Specific parameters and state variables are selected for obtaining variables observable over time for recognizing abnormal behaviours of considered mechanical systems. The estimation of the previously mentioned variables of interest is allowed by including Estimator Design Models in Kalman Filters.

Different methodologies based on model-based and data-driven approaches for monitoring mechanical systems have been developed over the years, as described by publications cited in the following.

The considered mechanical systems are monitored through nonlinear Kalman Filters integrated with the newly developed Estimator Design Models in this work. In particular, for each application field, the monitoring is made through a single model-based estimator.

Three different application fields concerning the condition monitoring of mechanical systems are explored:

1) **railway field** – a Constrained Unscented Kalman Filter has been employed to monitor the secondary suspension, in particular the anti-yaw dampers, for taking action on a fault of anti-yaw dampers identified through the anti-yaw damping parameter estimation. Furthermore, the proposed monitoring tool has been extended for monitoring the conditions of anti-yaw suspension components constituted of dampers and springs [1,2];
2) **automotive field** – two Extended Kalman Filters have been employed to monitor the tire-road interaction conditions and improve the active safety systems of road vehicles through the sideslip angle estimation. Two different Estimator Design Models are presented for designing Extended Kalman Filters. The tire-road condition monitoring is made by estimating the lateral tire-road friction coefficient for obtaining information related to roadbed and tire conditions [3,4];
3) **seismic engineering field** – a Constrained Unscented Kalman Filter has been employed to monitor the conditions of surfaces of Curved Surfaces Sliding Isolators by estimating friction coefficients on both surfaces. The estimation of friction coefficients allows checking the degradation of sliding surfaces due to ageing and severe working conditions [5].

1.1. Railway vehicles: monitoring of anti-yaw suspension components

The reliability of the railway system is a fundamental task in order to improve safety and vehicle timing. In this context, the anti-yaw dampers play a particular role since they have a strong impact on the hunting motion of railway vehicles.

The hunting phenomenon itself is essential for the guidance of a railway vehicle. The desired behaviour of a railway vehicle consists of the wheelset returns from an initial displacement caused, e.g., by track irregularities to its equilibrium position involving a decaying hunting motion. Excessive hunting causes high lateral wheel-rail forces, which can seriously damage the track, increasing the risk of the derailment of railway vehicles.
The improvement of railway vehicles running stability is possible by equipping them with springs and dampers, as a part of the railway secondary suspension system, for reducing undesired hunting oscillations.
The previously mentioned springs and dampers, called anti-yaw suspension components, are subjected to deterioration. As consequence, their maintenance becomes strongly crucial.
In particular, hydraulic dampers, typically used in railway vehicles, need seals. Since in the seals a sliding contact between two solids occurs, the seals are inevitably prone to wear and thereby to degradation, even if the oil of the damper provides lubrication. In contrast to this, no sliding contact occurs springs. Therefore, the dampers are the more critical components regarding degradation than the springs. Furthermore, a degradation of the anti-yaw dampers can lead to excessive hunting at lower speeds and, thereby, to higher lateral wheel-rail forces. Therefore, the anti-yaw dampers and their proper functioning are essential for the safe operation of a railway vehicle.

The maintenance of railway vehicles is usually carried out following a calendar-based approach. In order to ensure safety, the maintenance intervals are often set relatively low. In some cases, such fixed maintenance intervals may lead to unnecessary maintenance actions. Here, a condition-based maintenance appears as a feasible alternative to reduce the maintenance effort and the related costs.
To this aim, the real-time condition monitoring represents a valid tool to operate the vehicle in a more efficient and smarter way.

The condition monitoring of railway vehicles is typically based on signal processing, knowledge-based and data-driven methods [6,7] based on the development of artificial Neural Networks or on the knowledge of empirical systems. In contrast to these last approaches, the model-based methods are characterized by the advantage to directly obtain the information required for monitoring. Indeed, mechanical models of railway vehicles can be employed in order to develop, for example, estimators designed to identify the wheel-rail contact forces or the wheel profile [8 – 11].

Moreover, the model-based approaches can be adopted to estimate suspension parameters such as secondary lateral damping and anti-yaw damping [12 – 17].
These techniques can be carried out thanks to the nature of the railway vehicle dynamics that is taken into account in the mathematical model: indeed, the derived model contains the key physical parameters, directly linked to the wheel-rail contact and to the suspension damping.

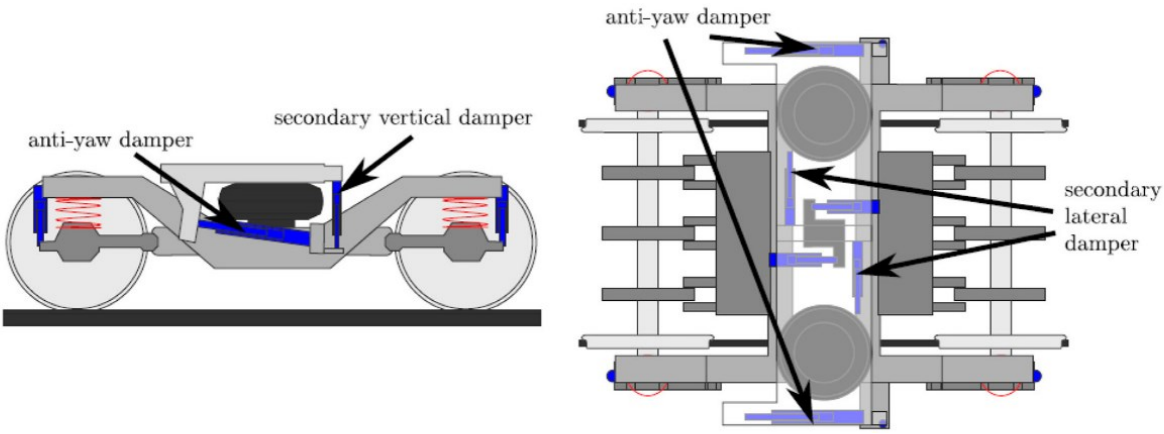

Figure 1.1. Positioning of anti-yaw dampers on the railway secondary suspension [18,19].

Model-based suspension condition monitoring relies typically on a modelling approach that don’t consider the wheelset dynamics [20] or use the Kalker linear theory for the determination of the wheel-rail contact forces [16,21,22].

From a theoretical point of view, critical issues of the hunting behaviour occur at high creepages due to the nonlinear relation between the creepages and the contact forces [23]; as a consequence, the modelling of the wheel-rail contact constitutes an important step for the estimator design model.

In this context, however, it has to be pointed out that the characteristics of the wheel-rail contact depends on several parameters, which can be uncertain and can vary considerably.
For instance, the geometry of the profiles of wheel and rail can vary due to the progress of wear, and the friction coefficient in the wheel-rail contact depends on temperature and humidity. Furthermore, variation of speed and irregularities, which also are uncertain, have an impact on the relative kinematics of wheel and rail and thereby also influence the wheel-rail forces. Therefore, the design of a specific reference model for the estimation could represent a challenging aspect.

A constrained model-based estimator is presented for monitoring anti-yaw dampers by estimating the anti-yaw damping. A random walk model for the estimation of contact forces and moments is included in the previously mentioned estimator.
The random approach is designed to estimate the wheel-rail contact interactions considering the scenario of running at a constant speed. Therefore, the longitudinal dynamics is neglected. At the same time, the random walk model approach is characterized by important advantages in terms of a priori no knowledge of both wheel-rail contact forces model and track irregularities.

The double target of the design is to obtain an estimator model able to reproduce the relevant physical phenomena but simple enough to limit the computational effort of the model-based observers [24 – 26].
The random variability of the interaction has been handled through a nonlinear constrained approach based on the Unscented Kalman Filter (UKF) [27,28], able to limit the variability of the estimated states compatibly with the constraints.

The UKF outperforms the extended Kalman filter (EKF) [27 – 31], but some issues still remain. More specifically, constraints on state variables cannot be taken into account and, consequently, the filter could fail in case of inaccurate system modelling or in presence of random variable model. Many approaches have been developed for UKF with constrained problems, also called constrained UKF (CUKF) [26,31 – 35].
Furthermore, the proposed methodology has been extended for monitoring anti-yaw suspension components, constituted of springs and dampers [2]. Therefore, the stiffness of springs included in the anti-yaw suspension components is estimated through the CUKF for condition monitoring purposes.

1.2. Road vehicles: monitoring of sideslip angle and tire-road interaction conditions

Over the past decades, driver assistance systems have become a standard in the automotive industry [36]. Nevertheless, the number of deaths caused each year in the world by road accidents exceeds one million.

This number is unacceptable related to technological advances. This very high value can be reduced by improving the performance of driver assistance systems if more state variables and parameters of road vehicles become available for onboard control and monitoring systems.

However, many of these variables, such as the sideslip angle, cannot be measured directly in road vehicles because the sensors are very expensive. Reliable vehicle control systems are developed typically around the vehicle sideslip angle determination [37 – 40].

Therefore, the knowledge of this kinematic variable is fundamental in this field, but its direct measurement is too expensive. Many studies aimed to provide reliable tools for the sideslip estimation based on the coupling between vehicle modelling and sensors. In [41,42], black-box and model-based approaches as Neural Networks and Extended Kalman Filter (EKF) [29] have been employed to make the sideslip angle estimation. Furthermore, the estimation of the tire-road friction coefficient is fundamental for improving the control and the safety of road vehicles. In autonomous vehicles, the tire-road friction coefficient can be estimated through environmental perception sensors installed on vehicles coupled with state observers [43].

Model-based estimation techniques can take into account inaccuracies of sensors. These approaches are based on vehicle models functional for the sideslip angle estimation and tire models to estimate, typically, the tire-road forces.

In literature, it is possible to distinguish mainly two approaches for developing vehicle state observers, employing readily available sensors to correct the estimation of variables which require the employment of expensive sensors.

The first approach uses a kinematic vehicle model, independent of tire parameters and road conditions, in combination with measurements obtainable from standard vehicle sensors. This estimation technique is sensitive to sensor errors (noise and bias). These errors generated by the GPS measurement can be reduced [44], but the required accuracy is not achievable by consumer-grade GPS, and reception may be lost.

The second approach is based on mechanical models of vehicles in combination with the measurements available from standard vehicle sensors. With this approach, the model can correct inaccuracies of sensors and unwanted measurements, but information on tire parameters and road conditions is needed for the tire model.

Different tire models have been chosen in [45 – 53] to design stochastic observers for the purposes previously described.

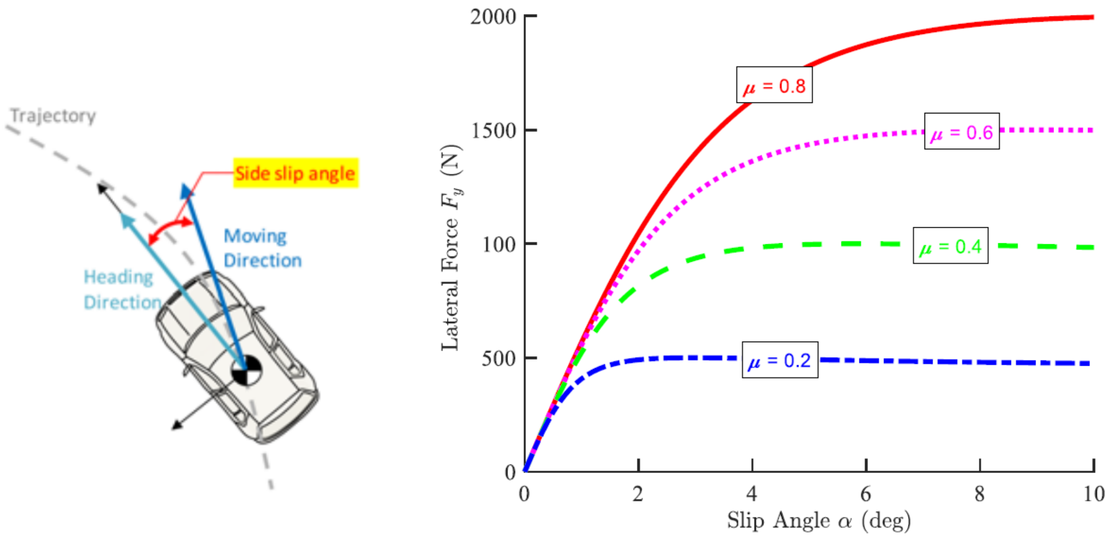

Figure 1.2. Lateral tire-road force VS slip angle under different road friction [54].

Issues referred to the required accurate parametrization of typically employed tire models are solved in [26,55,56] by integrating a Random Walk Model (RWM) approach with different types of Kalman Filters for tire-road forces estimation.

Two different model-based estimators based on the Extended Kalman Filter are proposed to monitor tire-road interaction conditions and to estimate the sideslip angle.

The first one has been designed around a double-track vehicle model coupled with a simple Magic formula characterized by four parameters obtained from extensive offline testing [57,58] for the tire modelling.

The lateral tire-road friction coefficient can be estimated on both left and right sides of the vehicle through this estimator for capturing information on different interaction conditions between tires and the roadbed. Therefore, it constitutes a monitoring tool able to differentiate the possible wear condition of tires on both sides of the vehicle and the presence of various types of roadbeds.

The second model-based estimator is able to identify the overall lateral tire-road friction coefficient. The estimator design model is based on a single-track vehicle model. A parametric estimation strategy has been employed to estimate the tire-road features with a priori no knowledge of specific tire models avoiding expensive experimental tests for their characterization. The estimation of the sideslip angle is provided by both the developed estimators.
The low computational load characterizing the proposed technique makes its implementation suitable for electronic control units onboard car vehicles.

Furthermore, the proposed model-based monitoring methodology is suitable for improving safety systems and driving aid tools in the automotive field.

1.3. Sliding seismic isolators: monitoring of instantaneous friction coefficients for the management of wear conditions

Base isolation is a recognized effective strategy to mitigate structural damages during strong earthquakes. A base isolation system consists of a flexible layer that separates the superstructure from its foundation and lengthens its fundamental period, with the final aim of reducing harmful vibrations induced by seismic ground shaking [59].
Among the different types of seismic isolators, Curved Surface Sliders (CSS) are widely used for the passive protection of buildings and bridges, thanks to their high load bearing capacity and large displacement capability combined with a compact design [60,61].
In their original design [62,63], the CSS isolators (Figure 1.3a) consist of a central pivot element forming, in combination with two outer concave plates, two sliding surfaces.

The primary sliding surface accommodates the horizontal displacements of the superstructure, providing a restoring effect through its curvature, and dissipating a certain amount of seismic energy through friction; the secondary sliding surface is aimed at accommodating relative rotations between the superstructure and the foundations. For sake of clarity, hereafter R_1, and μ_1 identify the radius of curvature, and the friction coefficient of the primary sliding surface, while R_2, and μ_2 relate to the radius of curvature, and the friction coefficient of the secondary sliding surface, respectively, whereas h denotes the height of the pivot element.

A double CSS, or DCSS, (Figure 1.3b) is a modification of the original single CSS design that includes two primary sliding surfaces ($R_1 = R_2$), each one encompassing all the above-mentioned functions. The main benefit of the double CSS design, over the original single CSS, is the reduction of its in-plan dimensions [64], as each concave plate is sized to accommodate one half of the total horizontal displacement.

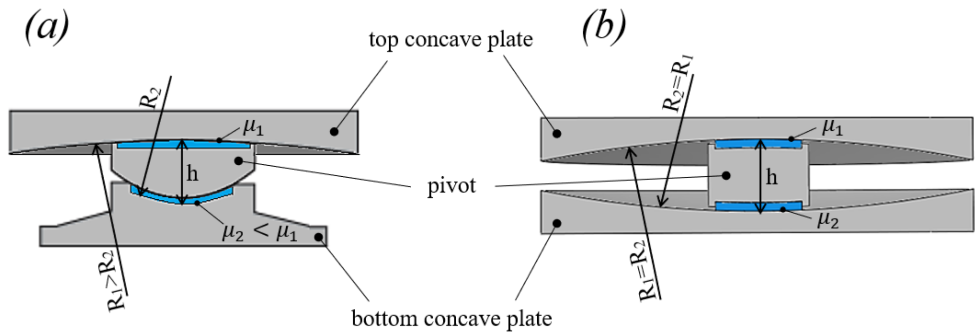

Figure 1.3. Schematic representation of single CSS (a) and DCSS (b), and definition of main parameters.

Theoretical and experimental studies [64 – 66] highlighted that the nonlinear lateral response of CSS units, i.e. effective stiffness, and equivalent viscous damping, depends on the geometrical and friction properties of the sliding elements.
The typical kinematic of a CSS in the horizontal plane is depicted in Figure 1.4. The relative displacement between top and bottom concave plates at any point of the motion trajectory can be resolved into its two components in x and y directions, and the centre of the pivot element lies on a straight line connecting the centres O and O’ of the two plates.
This relative displacement is partially resisted by restoring forces, produced by the effect of the gravity in combination with the curvature of the sliding surfaces [67 – 70].

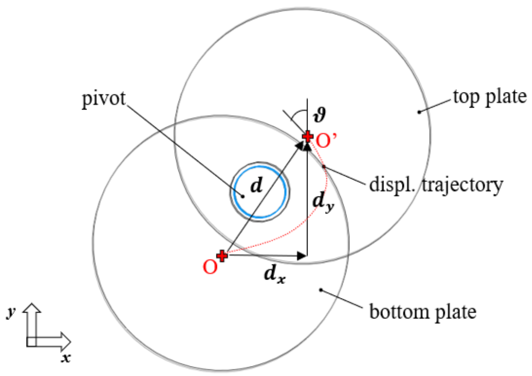

Figure 1.4. Plan-view of the typical kinematics of a CSS isolator.

The other source of resistance to motion is the friction force, which is of critical importance as it provides the energy dissipation of the isolation system and affects its recentring capability. In this respect, it is noted that energy dissipation and recentring capability represent two antithetic requirements of CSSs, as the first requires high friction coefficients which on the other side jeopardizes the restoring behaviour. The energy dissipation is ensured when CSSs are in sliding conditions, therefore, when the sliding velocity is different from zero. During sliding motions of CSSs, damping for dissipating the energy of the isolation system is obtainable. The damping design in a Coulomb friction context is tricky because of a transition between the two states of sliding and adhesion. In particular, by considering the dissipated power $P = \boldsymbol{F_{fric}} \cdot \boldsymbol{v}$ ($\boldsymbol{F_{fric}}$ is the friction force, while $\boldsymbol{v}$ is the sliding velocity), a negative value of the power is indicative of energy dissipation. When P is null, there is no dissipation. Therefore, in the state of adhesion, there is no damping. In low friction conditions, i.e., for a low friction coefficient, the friction force is low. Therefore, only little energy is dissipated. If the friction is too high, there is the risk of sticking. Therefore, isolators involve in the state of adhesion, in which the friction force is so high that the motion stops, and no further energy is dissipated. Therefore, a proper design of damping using Coulomb friction constitutes an optimization problem, where the friction coefficient has to be tuned in a relatively accurate way to achieve the desired behaviour of sliding isolators.

Special sliding material pads coupled with stainless steel surfaces are used in the sliding surfaces to control friction.

The sliding pads are usually made of a thermoplastic material, such as Polytetrafluoroethylene (PTFE) or Ultra High Molecular Weight Polyethylene (UHMWPE), that provides low friction resistance, high load-bearing capacity, stability the response during cycling, and durability.

Any deviation of the actual value of the coefficient of friction from its design value used in analyses and in design of the isolation system can negatively affect the expected response of the isolator and should be properly accounted for.

Such deviations are commonly observed during prototype testing of seismic isolators, which is a crucial step in the design and implementation of seismic isolation systems. Proper assessment of the isolator's performance is mandated by building standards to prove the adequacy of system performance to the desired levels of seismic protection. Modern standards, such as the American Society of Civil Engineering Standard ASCE-7 [71], the AASHTO Guide Specification for Seismic Isolation Design [72], and the European Standard EN 15129 [73], set

stringent limitations on the deviation from the design lateral performance of CSSs and DCSSs. This deviation is mostly ascribed to the variation of the coefficient of friction of the sliding material, which in turn may depend on standard material variability, manufacturing process, the effect of thermo-dynamical parameters, such as contact pressure, sliding velocity, and temperature, as well as contamination, wear and ageing of the sliding materials [74,75].
The experimental quantities measured during the tests consist in “global” quantities, such as forces and displacements, experienced by the entire isolation unit; however, such quantities do not allow to directly assess the actual friction performance of the individual sliding surfaces. The friction performance is indeed generally evaluated by means of an effective coefficient of friction, obtained from the measured lateral force and axial load on the isolation unit.

The effective coefficient of friction represents an average of the friction coefficients at the different sliding surfaces of the CSS unit, and, moreover, the contribution of each sliding surface is different from the actual coefficient of friction at that sliding surface because of the effect of the curvature [76].
Therefore, the estimate of the friction coefficient from testing is generally crude and not enough to accurately calibrate the friction property of each sliding surface, as required by theoretical predictive models for such isolators.
To overcome this limitation, an estimation technique for the coefficient of friction of the sliding surfaces of CSSs based on the Constrained Unscented Kalman filter (CUKF), is proposed.
The employment of the CUKF in various application fields [1,36,35,77] showed its superiority over the other Kalman filter algorithms from an estimation quality point of view thanks to the applicability of state constraints.

The estimator design model included in the CUKF algorithm is based on the Random Walk model [24,29,32,33,77]. The goal is the estimation of the coefficient of friction [78] and its variability on the individual surfaces during bidirectional motions without requiring any assumption on the underlying constitutive model.
Nowadays, bi-directional shaking table tests on structures implementing sliding isolators have never been carried out worldwide so far.
Although these data could be obtained through numerical analyses [79,80], the proposed tool has been customized to be applied to displacement-controlled loading protocols. This represents the most suitable configuration for testing machines, like the bi-directional testing bench of the EUCENTRE Lab (Pavia, Italy), and SRMD Lab (San Diego, California), dedicated to the

frictional characterization of the sliding isolators as required by International Standards (e.g. EN15129, AASHTO).
However, it is worth nothing that the suitability of a customized version of the proposed tool (CUKF coupled with RWM) for the estimation of the instantaneous frictional properties of sliding isolators under stochastic uniaxial displacements (recorded ground motions) has been already proven in [77].

The proposed model-based estimator can be employed as a monitoring tool for identifying degradation conditions of curved sliding surfaces of seismic isolators strictly dependent on their frictional properties.

2. OVERVIEW ON APPROACHES FOR MONITORING MECHANICAL SYSTEMS

As the complexity of industrial systems increases, fault diagnosis becomes crucial for maintaining system safety and reliability [81]. Many systems, such as printers, converters, seismic isolators, and vehicles (railway and automobiles), can be represented through physical-mathematical models.

For monitoring these systems, the estimation of state variables and parameters for verifying the health conditions of the considered one is required.

Therefore, different approaches, in particular model-based ones, for estimating variables functional to detect faults and monitor health conditions of mechanical systems have been developed over the years.

In general, a fault refers to an abnormal condition that may lead to reduction or loss of the capability of a system or its component to perform a required function.

On the other hand, a failure means the inability of a system or its component to perform its required functions within specified performance requirements.

System health monitoring is a key feature for failure prevention and Condition Based Maintenance (CBM). A health monitoring system needs to detect the development of a fault or failure promptly, and the faulty components can be replaced effectively to ensure the system's normal operation. In other words, health monitoring is a process which allows observing the behaviour of a system over time for identifying anomalies in its functioning. In the past few decades, maintenance strategies have evolved from early reactive maintenance to preventive maintenance, then to condition-based maintenance. Reactive maintenance is usually performed after system breakdown.

In order to prevent catastrophic failures, which cause emergency shutdowns, preventive maintenance is introduced. This maintenance strategy is carried out based on system operating time regardless of the current actual condition. Preventive maintenance consists of regularly scheduled maintenance activities to avoid future unforeseen failures.

In some cases, the failure of components of a system can have catastrophic consequences. Therefore, these crucial components are routinely maintained or replaced in fixed intervals. These intervals are chosen to carry out the maintenance before the risk of a catastrophic failure becomes too high. The scheduling of previously mentioned intervals requires accurate knowledge about how rapidly the degradation of a component proceeds, which might be complicated to gain.

Preventive maintenance may sometimes reduce unexpected failures, but it is not cost effective and cannot eliminate major failures. These conventional maintenance strategies do not satisfy the demands of high reliability in modern engineering systems.

Fortunately, CBM can be an effective alternative, and it tries to avoid unnecessary maintenance by taking maintenance actions when there is evidence of abnormality in a monitored system [82]. The monitoring is based on sensor measurements and does not interrupt normal operation. It attempts to avoid excessive or insufficient maintenance and ultimately results in higher system availability. Regarding the economic efficiency improvement, the CBM constitutes a good investment if the costs saved by the more efficient maintenance are higher than the costs for buying, installing, and operating the health monitoring system. The price of the health monitoring system also depends on the number and type of sensors employed for the health monitoring. Therefore, one of the tasks is to obtain reliable information about the system's current state by using a few inexpensive sensors, i.e., the number of the installed sensors should not be unnecessarily high, and the used sensors should not be necessarily expensive.

For instance, in the railway field [83], the forces acting in the wheel-rail contact are fundamental for the operational safety of a railway vehicle because excessive forces cause track damage, which in turn may cause accidents like, e.g., derailments. However, force sensors can't be installed in the wheel-rail contact of a rolling wheelset. Instrumented wheelsets, which can be seen as the most precise devices for measuring wheel-rail forces, are equipped with strain gauges so that the wheel-rail forces are measured indirectly by measuring structural deformations of the wheelset. Nevertheless, instrumented wheelsets are too expensive. Therefore, they are installed only for test runs (homologation of a new vehicle), but they are not suitable for regular railway vehicles used for commercial service. Therefore, for the health monitoring of previously mentioned railway vehicles used for commercial service, less expensive sensors, like accelerometers, must be used. Furthermore, as a general consideration, the sensors have to be installed to transmit the electric signals generated in the sensors to the recording unit in a simple, robust and inexpensive way.

In general, CBM includes three key steps: data collection, data processing and decision-making. These steps are shown in Figure 2.1. Data collection step is to obtain data related to system condition. Data processing is about handling and analyzing the data or signals collected for better understanding and interpretation.

The purpose of decision-making is to recommend efficient maintenance strategies. Diagnosis is fundamental in CBM. The objective of diagnosis is to indicate whether or not a fault has occurred and at the same time provide some information about the severity of the fault [84].

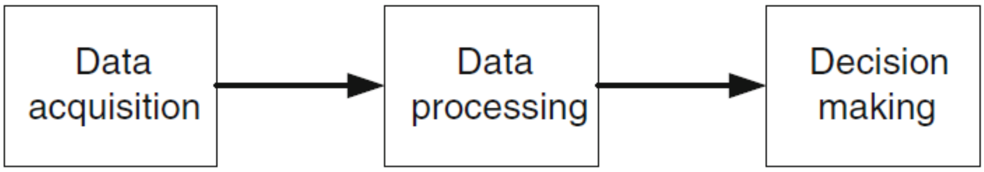

Figure 2.1. Three steps of Condition-Based Maintenance.

An overview of the principal monitoring approaches, focusing on the model-based ones based on Kalman Filters, is provided in this Chapter.

2.1. Monitoring methodologies

In general, there are three tasks for fault diagnosis, namely fault detection, fault isolation and fault identification [85].

1) ***Fault detection:*** it is the first step of fault diagnosis and tries to detect the presence of fault in the monitored system. Early detection of fault is very important before the fault possibly causes a catastrophic failure in the system.
2) ***Fault isolation:*** given that a fault has occurred and been detected, fault isolation aims to establish possible fault candidate that can explain the observed abnormal behaviour. For single fault diagnosis, the objective is to obtain a unique single fault that can lead to the observations. It may not always be possible to determine a unique candidate given the sensors available to the monitored system. As for multiple fault diagnosis, the goal is to acquire sets of faults that, occurring together, are able to explain the observations.
3) ***Fault identification:*** this step is to determine the magnitude of the fault and its type. For abrupt fault, if multiple fault sets remain after fault isolation, then identification is

required for each fault set and the fault set that matches the observations most closely is considered to be the true fault set. For incipient fault, the fault identification task is challenging since certain dynamic degradation behaviour for this fault must be assumed in advance and sometimes this prior knowledge is not easy to obtain. If the severity of the identified fault is acceptable, this severity will be used in the reconfiguration design of the system's control law to achieve fault tolerance. On the other hand, if the fault identification result indicates that the fault is too severe to be accommodated, then the corresponding faulty component has to be replaced.

The nature of possible faulty situations may be classified into three types as follows:

1) ***Incipient fault:*** slow developing and are usually related to the wear and tear of the system components as shown in Figure 2.2a. It is relatively difficult to detect the incipient fault due to its slowly developing nature of the fault and the compensation effect of the system's feedback control.
2) ***Abrupt fault:*** typically modelled as step-like deviation and is usually persistent as shown in Figure 2.2b, where t_0 is the time point at which the fault first starts. For abrupt fault, it is crucial that the fault diagnosis scheme is able to detect the sudden change in a timely manner to avoid catastrophic consequences. In such cases, early detection and accommodation are the key objectives of fault diagnosis.
3) ***Intermittent fault***: usually manifests itself intermittently in an unpredictable manner as shown in Figure 2.2c. For example, a worn-out roller in a printer may no longer be able to grip the paper consistently which in turn causes intermittent paper jams. A printer with a worn-out roller usually operates correctly but will infrequently slip and cause a paper jam. Intermittent faults are hard to handle for several reasons as follows. First, if diagnosis process is not performed continuously, it might due to the intermittent faults that are not present when diagnosis is active. Second, fault signals are not persistent and detection is not consistent. It is difficult, in this case, to distinguish between intermittent faults and other types of faults like abrupt faults and incipient faults.

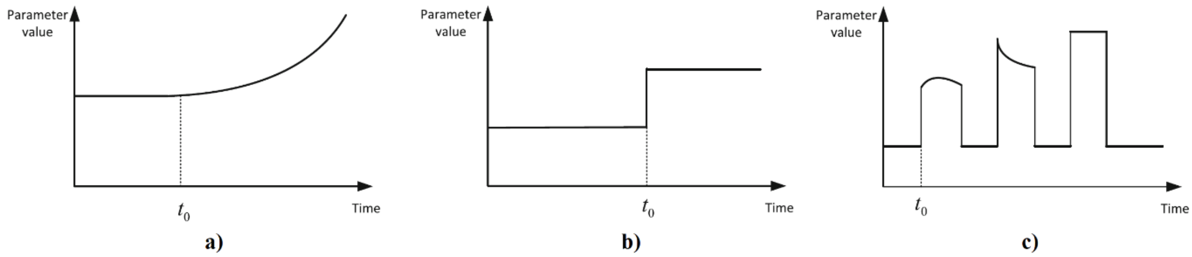

Figure 2.2. a) incipient fault profile; b) abrupt fault profile; c) intermittent fault profile.

Basically, abrupt and incipient faults belong to persistent faults, which means that once they appear, do not disappear, while intermittent faults do. In the following, various sources of faults in the monitored system will be discussed.

- ***Component fault:*** deviation of parameter value from its nominal one can cause condition change in the system. For example, a flat tire fault in a vehicle will increase the friction coefficient between ground and tire.
- ***Sensor fault:*** sensors provide signal measurements of a monitored system, and convey information related to a system's behaviour and its internal states. Sensor faults happen when there are discrepancies between measured signals and their actual values.
- ***Actuator fault:*** actuators are the control effectors of a system. For most electromechanical systems, control signals from the controllers cannot be directly applied to the system. Actuators are required to transform control signals to proper actuation signals such as torques and forces to drive the system. Actuator faults occur when there are discrepancies between desired actuator output and actual actuator output to the system.

These different fault sources are shown in Figure 2.3.

1) ***Uncertainties:*** uncertainties in modelling can be due to a bad estimation of dynamics in a system, a non-precise identification of the numerical values of the parameters or variation of their values because of heat, time or working conditions.
2) ***Disturbances:*** disturbances usually refer to noises in sensor measurements that are high frequency signals. Other factors like unmeasured friction, unknown inputs and backlash are also considered as disturbances.

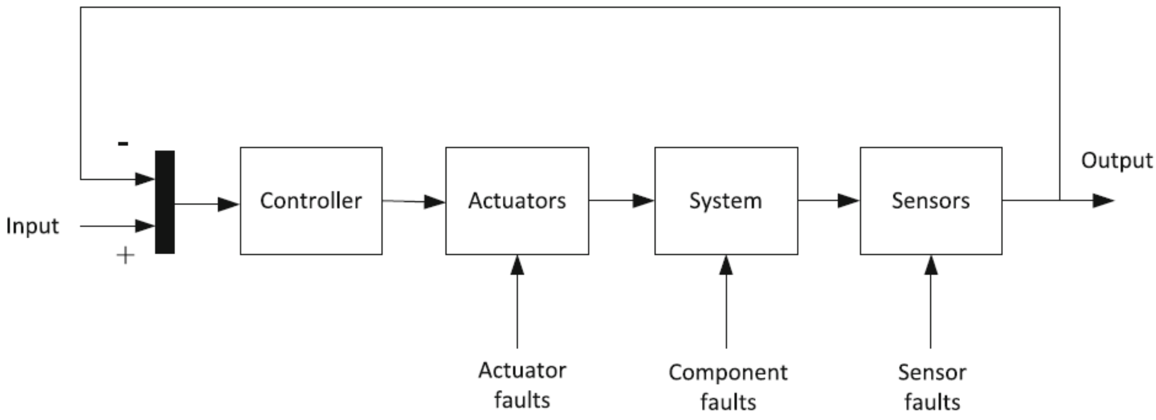

Figure 2.3. Different faults in a monitored system.

A good diagnostic system should be robust to various disturbances and uncertainties but still maintain its fault sensitivity.

Fault diagnosis methods can be broadly classified into two types (as shown in Figure 2.4): model-based method and data driven method.

For model-based methods, models serve as knowledge representation of a large amount of structural, functional and behavioural information and their relationship.

This knowledge representation is capitalized to create complex cause-effect reasoning leading to construction of powerful and robust automatic diagnosis and isolation systems [86]. Qualitative model-based approach provides an alternative when a numerical model of the system is unavailable. It utilizes qualitative abstractions to model complex systems while model structure is well defined.

The models used in qualitative methods are relatively simple compared with numerical models. The sensitivity of fault diagnosis system to modelling errors and sensor noises may be alleviated [87]. Qualitative Simulation (QSIM) is a widely used modelling tool to describe continuous model qualitatively [88].

This approach is intended to simulate the behaviour of physical systems using qualitative values, rather than providing explanations for behaviours of physical processes.

In [89], several faulty models are built using QSIM. The observed faulty behaviour is compared with that from the faulty models to choose the faults set which occur in the system. However, the faulty models determination needs prior knowledge.

In [90,91], QSIM based fault diagnosis is presented to handle multiple faults in continuous devices. The qualitative modelling framework quantizes the state space utilizing landmark values and specifies qualitative relations between the quantized states, which leads to a set of qualitative differential equations. A fuzzy qualitative simulation method is developed in [92]. The advantage of this method over QSIM based fault diagnosis is that if the observed behaviour cannot match the predicted behaviour of any faulty model, the candidate generator will check the modified models whose predicted behaviour can match the observed one.

Therefore, the modified models selected from the generator will be used to determine the fault candidates. The fuzzy qualitative simulation method can provide more precise information than QSIM based method because the utilization of fuzzy sets leads to a more accurate representation with respect to time. In continuous system diagnosis, time is an important factor to be considered during algorithm design.

However, it is difficult to choose appropriate fuzzy sets number and membership function which is a common problem for fuzzy logic system design. In addition, there is no efficient method to determine the number of modified models to be searched by candidate generator.

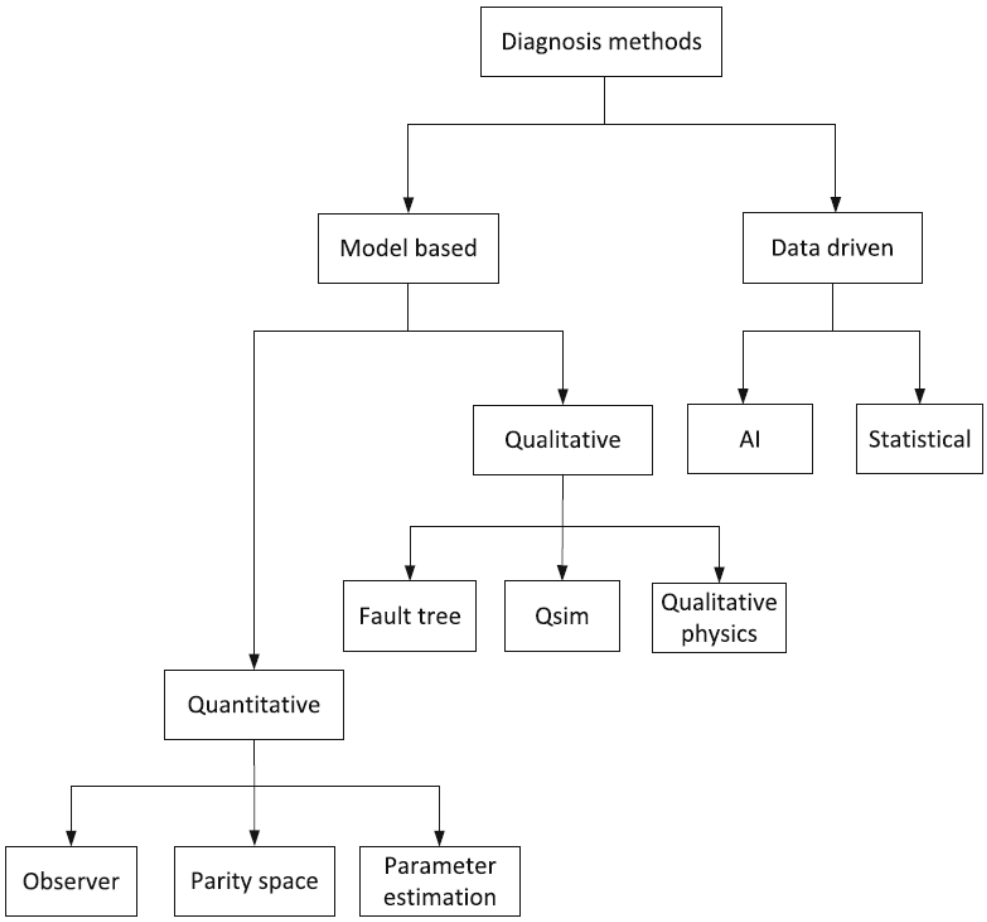

Figure 2.4. Classification of diagnosis methods.

Fault tree was originally introduced in 1961 at Bell Laboratories by H.A.Watson, under a U.S. Air Force Ballistics Systems Division project to evaluate the Minuteman I Intercontinental Ballistic Missile (ICBM) Launch Control System.

The Boeing Company modified the concept for computer utilization later. Fault tree is now widely used in many fields [93,94]. A fault tree is a model that graphically and logically represents the various combinations of possible events (faulty and normal), occurring in a system that lead to the top undesired event.

It is a structured methodology to determine the potential causes of an undesired event, referred to as the top event. The top event usually represents a major accident-causing safety hazards. While the top event is placed at the top of the tree, the tree is constructed downwards, dissecting the system with further detail until the primary events leading to the top event are known.

The tree usually has layers of nodes. At each node, different logic operations like AND and OR are performed for propagation as shown in Figure 2.5.

Generally, a fault tree analysis includes the following four steps: (i) system definition, (ii) fault tree construction, (iii) qualitative evaluation and (iv) quantitative evaluation [95].

Before the building of the fault tree, a detailed understanding of the system is required. To carry out consistent diagnosis from fault trees, the trees should completely represent the system causal relationships, i.e., explain all fault scenarios. However, no formal methods can be used to verify the accuracy of the fault tree established.

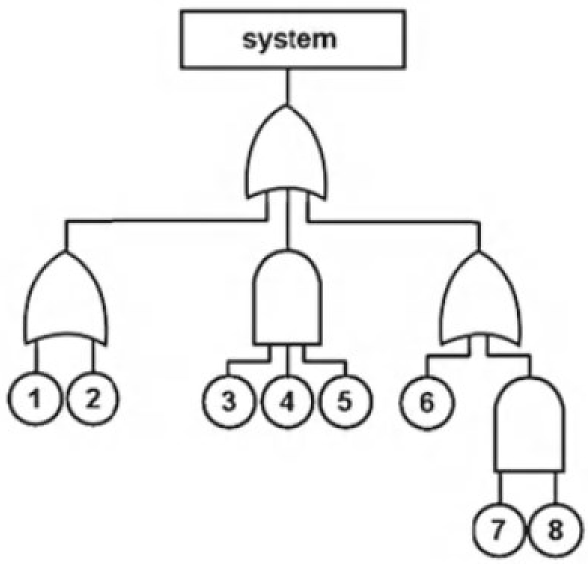

Figure 2.5. A faulty tree diagram.

Qualitative physics method usually derives qualitative equations from the differential equations. In [96], a Qualitative Bond Graph (QBG) method is developed based on the combination of qualitative reason and bond graph modelling theory in order to benefit from both methods. In QBG, qualitative equations form bond graph models instead of the differential equations are used for fault analysis.

These equations represent the components' physical variables, locations, and their functional relations that can be stated directly from the model.

This is particularly suitable for model-based fault diagnosis because possible faults can be localized through analysis of relations between the component states and observed abnormal behaviour qualitatively. Such qualitative algorithm is done using available measurement, i.e., the history of past data. Therefore, the qualitative behaviour equations are always written in differential causality [97].

Quantitative fault diagnosis method checks the consistency between actual system and its behaviour model. Consistency checking is usually achieved through a comparison between the information obtained from the real system and information computed from a behavioural model. The resultant differences are called residuals.

Each residual should be theoretically zero or near zero when the system is normal but should distinguishably deviate from zero when a fault happens [98].

A fault is detected by monitoring the trend of the residuals, which usually involves setting a fixed threshold on a residual quantity.

The models should be insensitive to modelling errors and at the same time sensitive to faults.

In general, quantitative model-based fault diagnosis method consists of two main stages: residual generation and residual evaluation as shown in Figure 2.6.

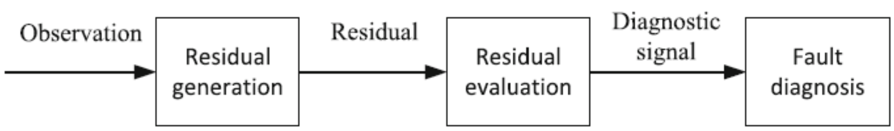

Figure 2.6. General flowchart of a quantitative model-based fault diagnosis method.

The residual generation is essentially a procedure for extracting fault symptoms from the system measurements. In the residual evaluation, the trend of the generated residuals is inspected which usually involves setting a fixed threshold on a residual quantity. A well-designed residual makes residual evaluation process simple.

Observer based fault diagnosis (Figure 2.7) is a well-known analytical model based FDI scheme, which compares the actual output from a system with reference output from an analytical model.

An observer-based residual is simply the output estimation error itself or a combination of the output estimation errors. Various nonlinear observer design techniques have been used for residual generation, since no single, universal, optimal nonlinear observer exists for all nonlinear systems.

The existing nonlinear observers have to be designed usually under certain assumptions on system structure, system inputs, and/or the degree of the system nonlinearity [99]. For deterministic framework, Hammouri et al. [100] utilized high-gain observers for fault detection of control affine nonlinear systems.

Ding and Frank [101] developed adaptive nonlinear observers for fault detection. Sliding mode observer is a useful tool for fault diagnosis.

Edwards et al. [102] used a sliding mode observer to reconstruct faults, with no explicit consideration of the disturbances or uncertainty.

Tan and Edwards [103] is based on the work of [104], i.e., using multiple observers in cascade. However, the observer that is used exploits a super-twisting structure which will give a higher degree of accuracy for the fault estimation.

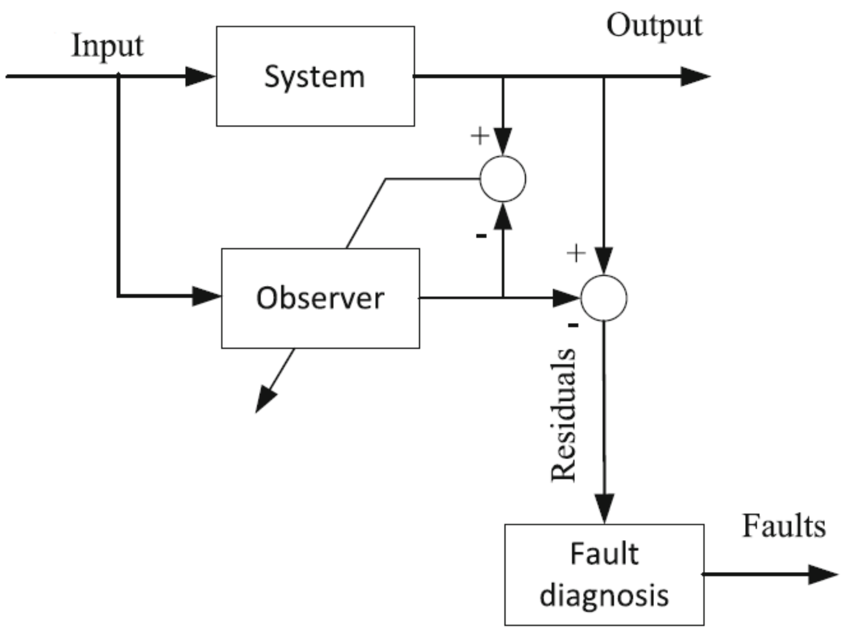

Figure 2.7. Observer based method for generating residuals.

Since the disturbances of system under monitoring are random fluctuations with only their statistical parameters known, one solution to the fault diagnosis problem in such systems is to entail optimal state estimate with minimum estimation error.
The Kalman filter in state space model is equivalent to an optimal predictor for a linear stochastic system using input-output model. It is well known that the Kalman filter is a recursive algorithm for state estimation, and it has found wide applications in industrial applications. Alessandri et al. [105] used extended Kalman filter for detection of actuator faults in unmanned underwater vehicles.
In [106], an extended Kalman filter is proposed for the estimation for an orbiting spacecraft. The developed methodology decides if a sensor fault has happened, locates the faulty sensor, and outputs the healthy sensor measurements.

Another approach for obtaining the residual generation is parameter estimation. This approach assumes that the faults of a dynamical system (mechanical systems, electrical systems, biological systems, etc.) can be reflected by the physical parameters such as mass, friction, resistance, etc. Faults described as time dependent parameter drifts can be handled through parameter estimation [107].
The most important issue related to parameter estimation method for fault diagnosis is the complexity of the model. If the process model is a complex nonlinear model, then the parameter estimation problem is essentially a nonlinear optimization problem.
Another element of quantitative based method is residual evaluation, which determines whether any faults have occurred by checking the residuals and their trends.
The decision-making rules usually are designed specifically for different process [108].
Robust fault diagnosis tries to minimize misdetection and false alarms by considering the residual noises. Misdetection means missing to detect the presence of an actually occurred fault. On the contrary, false alarm refers to an indication of fault which in fact does not happen. There are various approaches to generate robust residuals, which are insensitive to modelling uncertainties and measurement noises.
One of the robust methods, known as active approach, is based on generating residuals that are insensitive to modelling uncertainties, but sensitive to faults.
Some techniques like unknown input observer and robust parity equations are proposed to achieve active robust performance [109 – 111].
An alternative approach to achieve robust, called as passive, attempts to accomplish robust in the decision-making stage. In these methods, the effect of the parameter uncertainty is

propagated to the residuals and then an adaptive threshold is used to envelop these residuals to achieve robust [112,113].

It can be concluded that one of the major advantages of the quantitative model-based method is the ability to incorporate physical understanding of the underlying process into the monitoring scheme.
However, several issues such as system nonlinearity, process complexity and lack of accurate data make it difficult, sometimes even impractical, to construct an accurate analytical model for the system.
All these factors limit the usefulness of this approach in real industrial applications. In contrast to the model-based methods where a priori quantitative or qualitative knowledge about the system is required, only historical data is required by data driven based approaches.
There are different ways in which this data can be represented as a priori knowledge to a diagnostic system. This process is known as feature extraction.
Data driven diagnostic approaches can be broadly classified as statistical methods and Artificial Intelligence (AI) methods [114].
There are some limitations to those methods which are based solely on historic process data. One limitation is their generalization capability outside of the training data.
Besides its lack of generalization ability, neural networks also have a difficulty in dealing with multiple faults. This limitation leads to an outstanding distinction between model-based approaches and data driven methods.

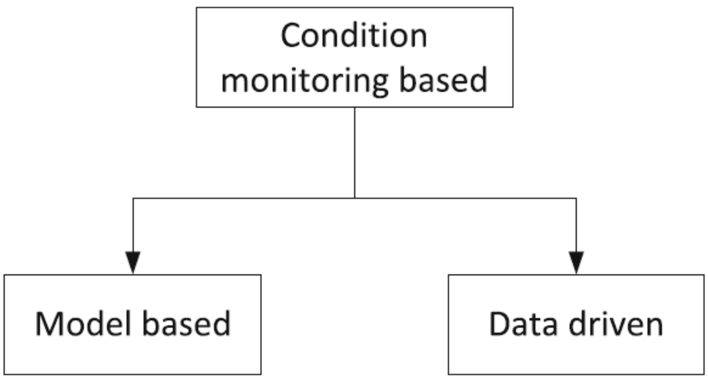

Figure 2.8. Typical methodologies for diagnostic purposes.

2.2. Model-based monitoring approach: the Kalman Filter

The condition monitoring of mechanical systems can be made through model-based techniques based on the Kalman Filter [29]. The Kalman Filter is a stochastic state observer employable for reconstructing the state of dynamical systems, in this case, of mechanical ones.
Kalman Filters are typically employed for monitoring purposes or to emulate sensors in feedback control systems.

The Kalman Filter is a two steps estimator. In the first step, called prediction, the filter allows for predicting the state variables for monitoring the desired system through a mathematical model of this latter.
The developed model, called estimator design model, must be able to capture, correctly, the fundamental dynamics of the system to be monitored.
In the second step, called correction, the predicted variables are corrected employing measurements obtainable from the real system equipped with sensors, typically affected by uncertainties and inaccuracies. The estimated state is assumed to be a Gaussian Random Variable (GRV).

The prediction-correction algorithm is recursive. The Kalman Filter is suitable for real-time applications. The same inputs affecting the real system and the measurements provided from this latter are required for employing the Kalman Filter as a real-time monitoring tool.
The Kalman Filter is largely applied in technology.
A common application is for guidance, navigation, and control of vehicles. In the mechanical system field, it can be applied for different systems as road vehicles, engines, civil structures, railway vehicles, etc.

In this work, the Kalman Filter has been employed for monitoring three types of mechanical systems: the railway vehicle, seismic sliding isolators and the road vehicle.
State variables and parameters functional for monitoring purposes have been estimated through nonlinear Kalman Filters. In particular, the Constrained Unscented Kalman Filter [1,2,5,26,33] and the Extended Kalman Filter [29] have been chosen for this purpose. Starting from the linear Kalman Filter, an overview on these model-based stochastic estimators is provided in their discrete-time form, particularly functional for the implementation in computational environments.

2.2.1. The linear Kalman Filter

When the system to be monitored can be modelled as a linear time-invariant (LTI) one [29], the linear Kalman Filter is suitable for state estimation.

Considering a linear discrete-time system given as follows [29]:

$$\begin{gathered} \boldsymbol{x}_k = \boldsymbol{F}_{k-1}\boldsymbol{x}_{k-1} + \boldsymbol{G}_{k-1}\boldsymbol{u}_{k-1} + \boldsymbol{w}_{k-1} \\ \boldsymbol{y}_k = \boldsymbol{H}_k\boldsymbol{x}_k + \boldsymbol{v}_k \end{gathered} \tag{2.1}$$

where:

- $\boldsymbol{x}_k$ is the state vector of size $[n \times 1]$, at the current instant *k*;
- $\boldsymbol{x}_{k-1}$ is the state vector of size $[n \times 1]$, at the instant *k-1* preceding the instant *k*;
- $\boldsymbol{u}_{k-1}$ is the input vector of size $[p \times 1]$, at the instant *k-1* preceding the instant *k*;
- $\boldsymbol{F}_{k-1}$ is the state transition matrix of size $[n \times n]$;
- $\boldsymbol{G}_{k-1}$ is the input matrix of size $[n \times p]$;
- $\boldsymbol{H}_k$ is the output matrix of size $[q \times n]$;
- $\boldsymbol{y}_k$ is the measurement vector of size $[q \times 1]$, at the current instant *k*;
- $\boldsymbol{w}_{\boldsymbol{k}}$ and $\boldsymbol{v}_k$ are Gaussian white noises representing the process and the measurement noises, respectively.

The noises $\boldsymbol{w}_k$ and $\boldsymbol{v}_k$ are characterized by known covariance matrices $\boldsymbol{Q}_k$ and $\boldsymbol{R}_k$, respectively.

$$\begin{gathered} \boldsymbol{w}_k \sim (\boldsymbol{0}, \boldsymbol{Q}_k) \\ \boldsymbol{v}_k \sim (\boldsymbol{0}, \boldsymbol{R}_k) \\ E[\boldsymbol{w}_k\boldsymbol{w}_j^T] = \boldsymbol{Q}_k\delta_{k-j} \\ E[\boldsymbol{v}_k\boldsymbol{v}_j^T] = \boldsymbol{R}_k\delta_{k-j} \\ E[\boldsymbol{v}_k\boldsymbol{w}_j^T] = \boldsymbol{0} \end{gathered} \tag{2.2}$$

where δ_{k-j} is the Kronecker delta function: that is, $\delta_{k-j} = 1$ if $k = j$, and $\delta_{k-j} = 0$ if $k \neq j$. The expected value of the generic random variable X is indicated with $E(X)$.

The aim of the Kalman Filter is to estimate the state $\boldsymbol{x}_k$ based on the knowledge of the considered system dynamics and the availability of the noisy measurements $\boldsymbol{y}_k$.

If all the measurements, including them at the time instant k, are available for making a correction of the prediction of $\boldsymbol{x}_k$, then it is possible to form the *a posteriori estimation*, denoted as $\hat{\boldsymbol{x}}_k^+$**.** The "+" superscript denotes that the estimation is a *posteriori.*

One way to form the a *posteriori* state estimation is to compute the expected value of $\boldsymbol{x}_k$ conditioned on all the measurements for each time instant t included in the range $1 \leq t \leq k$:

$$\text{a posteriori estimation: } \hat{\boldsymbol{x}}_k^+ = E[\boldsymbol{x}_k | y_1, y_2, \dots, y_k] \tag{2.3}$$

If all the measurements before (but not including) time k are available it is possible to form the a *priori estimation*, denoted with $\hat{\boldsymbol{x}}_k^-$**.** The "-" superscript denotes that the estimate is a *priori.* One way to form the a *priori* state estimation is to compute the expected value of $\boldsymbol{x}_k$**,** conditioned on all the for each time instant t included in the range $1 \leq t \leq k-1$:

$$\text{a priori estimation: } \hat{\boldsymbol{x}}_k^- = E[\boldsymbol{x}_k | y_1, y_2, \dots, y_{k-1}] \tag{2.4}$$

Therefore, it is intuitive for understanding that the estimation obtainable through $\hat{\boldsymbol{x}}_k^+$ is more accurate than $\hat{\boldsymbol{x}}_k^-$ for the greater quantity of information employable for its calculation. The initial estimation of $\boldsymbol{x} = \boldsymbol{x}_0$ is indicated with $\hat{\boldsymbol{x}}_0^+$, and it is computed as follows:

$$\hat{\boldsymbol{x}}_0^+ = E(\boldsymbol{x}_0) \tag{2.5}$$

$\boldsymbol{P}_k$ denotes the covariance of the estimation error, in particular:

- $\boldsymbol{P}_k^-$ denotes the covariance of the estimation error of $\hat{\boldsymbol{x}}_k^-$;
- $\boldsymbol{P}_k^+$ denotes the covariance of the estimation error of $\hat{\boldsymbol{x}}_k^+$.

The “a priori” and “a posteriori” covariance matrices of the estimation error, are computed as follows:

$$\begin{aligned} \boldsymbol{P}_k^- &= E[(\boldsymbol{x}_k - \hat{\boldsymbol{x}}_k^-)(\boldsymbol{x}_k - \hat{\boldsymbol{x}}_k^-)^T] \\ \boldsymbol{P}_k^+ &= E[(\boldsymbol{x}_k - \hat{\boldsymbol{x}}_k^+)(\boldsymbol{x}_k - \hat{\boldsymbol{x}}_k^+)^T] \end{aligned} \tag{2.6}$$

The estimation procedure through time is represented in Figure 2.9. After processing the measurement at time $(k-1)$, the estimation of $\boldsymbol{x}_{k-1}$ (denoted with $\hat{\boldsymbol{x}}_{k-1}^+$) and the covariance of the estimation error related to $\boldsymbol{x}_{k-1}$ (denoted with $\boldsymbol{P}_{k-1}^{+}$) are obtained. At the time instant k, precisely before the measurement processing at that time instant, the estimation of $\boldsymbol{x}_k$ (denoted with $\hat{\boldsymbol{x}}_k^{-}$) and the related covariance of the estimation error (denoted with $\boldsymbol{P}_k^{-}$) are computed. Finally, the measurement processing at time instant k for obtaining the corrected estimation of $\boldsymbol{x}_k$ is made**.** The obtained estimation of $\boldsymbol{x}_k$ is denoted with $\hat{\boldsymbol{x}}_k^{+}$, and its covariance is denoted with $\boldsymbol{P}_k^{+}$.

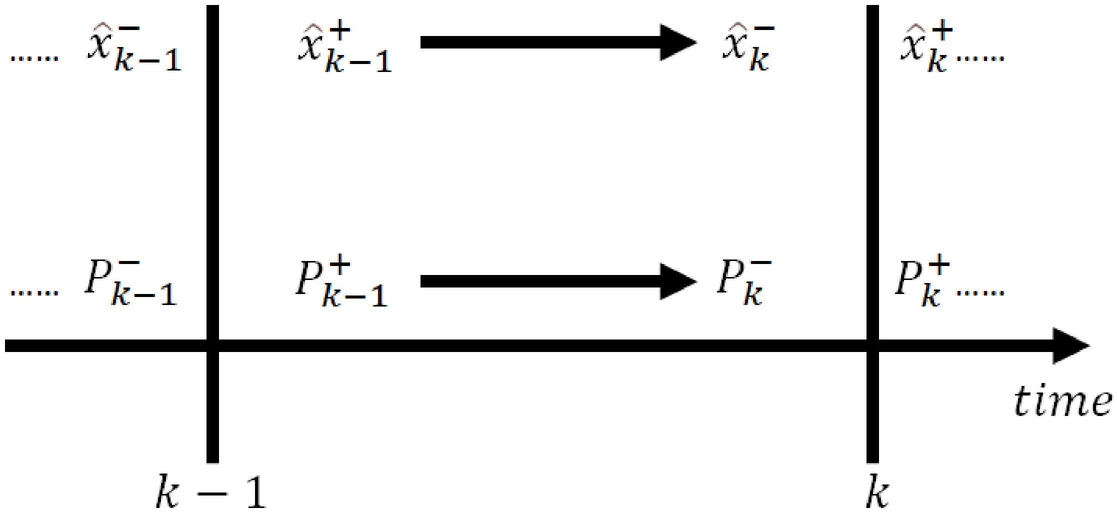

Figure 2.9. Timeline showing a prior and a posteriori state estimates and estimation error covariances.

The initialization of the Kalman Filter is made by imposing the initial condition $\boldsymbol{x}_0 = \hat{\boldsymbol{x}}_0^{+} = E(\boldsymbol{x}_0)$, where $\hat{\boldsymbol{x}}_0^{+}$ is the best estimation of the initial state $\boldsymbol{x}_0$. Therefore, the a priori estimation of $\boldsymbol{x}$ at time instant $k = 1$ can be obtained as follows:

$$\hat{\boldsymbol{x}}_1^{-} = \boldsymbol{F}_0 \hat{\boldsymbol{x}}_0^{+} + \boldsymbol{G}_0 \boldsymbol{u}_0 \tag{2.7}$$

Therefore, it is possible to extend the Equation (2.7) for each time instant k:

$$\hat{\boldsymbol{x}}_k^{-} = \boldsymbol{F}_{k-1} \hat{\boldsymbol{x}}_{k-1}^{+} + \boldsymbol{G}_{k-1} \boldsymbol{u}_{k-1} \tag{2.8}$$

The Equation 2.8 is called *prediction step of Kalman Filter* for obtaining the estimated state $\hat{\boldsymbol{x}}$. No measurements are employed for computing the prediction. Therefore, during the prediction step, only the knowledge on the system dynamics is required based on a mathematical model of the system to be monitored. The prediction step also includes the propagation of the covariance matrix of the estimation error $\boldsymbol{P}$. During the initialization of the Kalman Filter, the covariance of the estimation error is represented by the following Equation:

$$\boldsymbol{P}_0^+ = E[(\boldsymbol{x}_0 - \hat{\boldsymbol{x}}_0^+)(\boldsymbol{x}_0 - \hat{\boldsymbol{x}}_0^+)^T] \tag{2.9}$$

Therefore, $\boldsymbol{P}_0^+$ represents the uncertainty of the initial state estimation $\hat{\boldsymbol{x}}_0^+$. If the knowledge of the initial state $\boldsymbol{x}_0$ is perfect, then $\boldsymbol{P}_0^+$ can be selected as $\boldsymbol{P}_0^+ = 0\boldsymbol{I}$, where $\boldsymbol{I}$ is the identity matrix. If the knowledge of the initial state $\boldsymbol{x}_0$ is poor, then $\boldsymbol{P}_0^+$ can be assumed as $\boldsymbol{P}_0^+ \to \infty\boldsymbol{I}$. For obtaining the a priori covariance of the estimation error $\boldsymbol{P}_1^-$ based on the knowledge of $\boldsymbol{P}_0^+$, the following Equation is adopted:

$$\boldsymbol{P}_1^- = \boldsymbol{F}_0\boldsymbol{P}_0^+\boldsymbol{F}_0^T + \boldsymbol{Q}_0 \tag{2.10}$$

Equation 2.10 is obtained from the discrete-time Lyapunov equation [25], and it can be extended for each time instant k:

$$\boldsymbol{P}_k^- = \boldsymbol{F}_{k-1}\boldsymbol{P}_{k-1}^+\boldsymbol{F}_{k-1}^T + \boldsymbol{Q}_{k-1} \tag{2.11}$$

where, $\boldsymbol{Q}$ is defined as the covariance matrix of the process noise $\boldsymbol{w}_k$. The covariance matrix $\boldsymbol{Q}$ represents the confidence in the mathematical model representing the system to be monitored. High values of $\boldsymbol{Q}$ indicate the presence of big discrepancies between model and real system. Low values of $\boldsymbol{Q}$ indicate the accordance of the model with the real system.
The a priori estimation $\hat{\boldsymbol{x}}_k^-$ must be corrected through the available measurements for obtaining the a posteriori estimation $\hat{\boldsymbol{x}}_k^+$. Therefore, adopting the recursive least squares method [29], the *correction step of Kalman Filter* is described by the following Equations:

$$\begin{gathered}\boldsymbol{K}_k = \boldsymbol{P}_k^-\boldsymbol{H}_k^T(\boldsymbol{H}_k\boldsymbol{P}_k^-\boldsymbol{H}_k^T + \boldsymbol{R}_k)^{-1} \\ \hat{\boldsymbol{x}}_k^+ = \hat{\boldsymbol{x}}_k^- + \boldsymbol{K}_k(\boldsymbol{y}_k - \boldsymbol{H}_k\hat{\boldsymbol{x}}_k^-) \\ \boldsymbol{P}_k^+ = (\boldsymbol{I} - \boldsymbol{K}_k\boldsymbol{H}_k)\boldsymbol{P}_k^-(\boldsymbol{I} - \boldsymbol{K}_k\boldsymbol{H}_k)^T + \boldsymbol{K}_k\boldsymbol{R}_k\boldsymbol{K}_k^T\end{gathered} \tag{2.12}$$

where $\boldsymbol{K}_k$ is the Kalman Gain matrix. The difference $(\boldsymbol{y}_k - \boldsymbol{H}_k\hat{\boldsymbol{x}}_k^-)$, called *innovation*, represents the gap between the available measurements from sensors $\boldsymbol{y}_k$ and the estimated ones $\hat{\boldsymbol{y}}_k = \boldsymbol{H}_k\hat{\boldsymbol{x}}_k^-$.

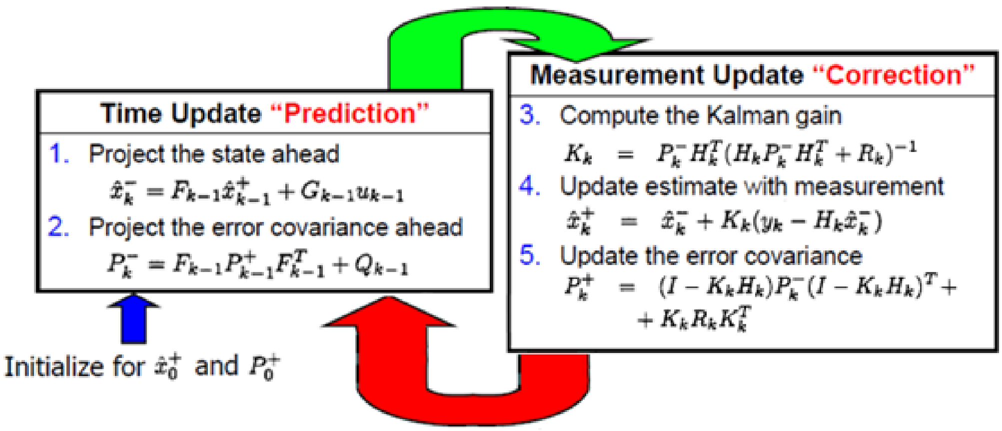

Figure 2.10. Recursive algorithm of the Kalman Filter.

If the innovation tends to zero, the Kalman Filter is able to estimate the available measurements correctly. Therefore, the contribution of the Kalman Gain is not significant for the correction step. If the innovation is represented by a great value, the estimated measurements are not in accordance with the available ones. Therefore, Therefore, the contribution of the Kalman Gain is fundamental for obtaining a reliable estimation of the state variables.

In the following, the complete recursive algorithm of the discrete-time linear Kalman Filter is shown:

1) the system dynamics are given by the following Equations:

$$\begin{gathered}
\boldsymbol{x}_k = \boldsymbol{F}_{k-1}\boldsymbol{x}_{k-1} + \boldsymbol{G}_{k-1}\boldsymbol{u}_{k-1} + \boldsymbol{w}_{k-1} \\
\boldsymbol{y}_k = \boldsymbol{H}_k\boldsymbol{x}_k + \boldsymbol{v}_k \\
E[\boldsymbol{w}_k\boldsymbol{w}_j^T] = \boldsymbol{Q}_k\delta_{k-j} \\
E[\boldsymbol{v}_k\boldsymbol{v}_j^T] = \boldsymbol{R}_k\delta_{k-j} \\
E[\boldsymbol{v}_k\boldsymbol{w}_j^T] = \boldsymbol{0}
\end{gathered} \tag{2.13}$$

2) the Kalman filter is initialized as follows:

$$\begin{gathered}
\hat{\boldsymbol{x}}_0^+ = E(\boldsymbol{x}_0) \\
\boldsymbol{P}_0^+ = E[(\boldsymbol{x}_0 - \hat{\boldsymbol{x}}_0^+)(\boldsymbol{x}_0 - \hat{\boldsymbol{x}}_0^+)^T]
\end{gathered} \tag{2.14}$$

3) the Kalman filter is given by the following Equations, which are computed for each time step $k = 1,2, \ldots$:

$$\begin{gathered}
\boldsymbol{P}_k^- = \boldsymbol{F}_{k-1}\boldsymbol{P}_{k-1}^+\boldsymbol{F}_{k-1}^T + \boldsymbol{Q}_{k-1} \\
\boldsymbol{K}_k = \boldsymbol{P}_k^-\boldsymbol{H}_k^T(\boldsymbol{H}_k\boldsymbol{P}_k^-\boldsymbol{H}_k^T + \boldsymbol{R}_k)^{-1} \\
\text{a priori state estimation: } \widehat{\boldsymbol{x}}_k^- = \boldsymbol{F}_{k-1}\widehat{\boldsymbol{x}}_{k-1}^+ + \boldsymbol{G}_{k-1}\boldsymbol{u}_{k-1} \\
\text{a posteriori state estimate: } \widehat{\boldsymbol{x}}_k^+ = \widehat{\boldsymbol{x}}_k^- + \boldsymbol{K}_k(\boldsymbol{y}_k - \boldsymbol{H}_k\widehat{\boldsymbol{x}}_k^-) \\
\boldsymbol{P}_k^+ = (\boldsymbol{I} - \boldsymbol{K}_k\boldsymbol{H}_k)\boldsymbol{P}_k^-(\boldsymbol{I} - \boldsymbol{K}_k\boldsymbol{H}_k)^T + \boldsymbol{K}_k\boldsymbol{R}_k\boldsymbol{K}_k^T
\end{gathered} \tag{2.15}$$

2.2.2. The Extended Kalman Filter

The Extended Kalman Filter (EKF) is one of the most famous nonlinear formulations of the Kalman Filter. The EKF is typically employed for the estimation of state variables of nonlinear systems. The nonlinear system is linearized around the Kalman Filter estimation based on the linearized system.

Considering a nonlinear discrete-time system given as follows [29]:

$$\begin{gathered}
\boldsymbol{x}_k = \boldsymbol{f}_{k-1}(\boldsymbol{x}_{k-1}, \boldsymbol{u}_{k-1}, \boldsymbol{w}_{k-1}) \\
\boldsymbol{y}_k = \boldsymbol{h}_k(\boldsymbol{x}_k, \boldsymbol{v}_k) \\
\boldsymbol{w}_k \sim (\boldsymbol{0}, \boldsymbol{Q}_k) \\
\boldsymbol{v}_k \sim (\boldsymbol{0}, \boldsymbol{R}_k)
\end{gathered} \tag{2.16}$$

where $\boldsymbol{f}_{k-1}$ and $\boldsymbol{h}_k$ are the nonlinear state transition function and the measurement function, respectively. The state equation $\boldsymbol{x}_k = \boldsymbol{f}_{k-1}(\boldsymbol{x}_{k-1}, \boldsymbol{u}_{k-1}, \boldsymbol{w}_{k-1})$ can be expanded in Taylor series around $\boldsymbol{x}_{k-1} = \widehat{\boldsymbol{x}}_{k-1}^+$ and $\boldsymbol{w}_{k-1} = \boldsymbol{0}$. Therefore, the following form of the state equation is obtained:

$$\begin{aligned}
\boldsymbol{x}_k &= \boldsymbol{f}_{k-1}(\widehat{\boldsymbol{x}}_{k-1}^+, \boldsymbol{u}_{k-1}, \boldsymbol{0}) + \left.\frac{\partial \boldsymbol{f}_{k-1}}{\partial \boldsymbol{x}}\right|_{\widehat{\boldsymbol{x}}_{k-1}^+} (\boldsymbol{x}_{k-1} - \widehat{\boldsymbol{x}}_{k-1}^+) + \left.\frac{\partial \boldsymbol{f}_{k-1}}{\partial \boldsymbol{w}}\right|_{\widehat{\boldsymbol{x}}_{k-1}^+} \boldsymbol{w}_{k-1} \\
&= \boldsymbol{f}_{k-1}(\widehat{\boldsymbol{x}}_{k-1}^+, \boldsymbol{u}_{k-1}, \boldsymbol{0}) + \boldsymbol{F}_{k-1}(\boldsymbol{x}_{k-1} - \widehat{\boldsymbol{x}}_{k-1}^+) + \boldsymbol{L}_{k-1}\boldsymbol{w}_{k-1} \\
&= \boldsymbol{F}_{k-1}\boldsymbol{x}_{k-1} + [\boldsymbol{f}_{k-1}(\widehat{\boldsymbol{x}}_{k-1}^+, \boldsymbol{u}_{k-1}, \boldsymbol{0}) - \boldsymbol{F}_{k-1}\widehat{\boldsymbol{x}}_{k-1}^+] + \boldsymbol{L}_{k-1}\boldsymbol{w}_{k-1} \\
&= \boldsymbol{F}_{k-1}\boldsymbol{x}_{k-1} + \widetilde{\boldsymbol{u}}_{k-1} + \widetilde{\boldsymbol{w}}_{k-1}
\end{aligned} \tag{2.17}$$

where $\boldsymbol{F}_{k-1} = \left.\frac{\partial \boldsymbol{f}_{k-1}}{\partial \boldsymbol{x}}\right|_{\widehat{\boldsymbol{x}}_{k-1}^+}$, and $\boldsymbol{L}_{k-1} = \left.\frac{\partial \boldsymbol{f}_{k-1}}{\partial \boldsymbol{w}}\right|_{\widehat{\boldsymbol{x}}_{k-1}^+}$. The transformed process noise $\widetilde{\boldsymbol{w}}_{k-1}$, and the known input signal $\widetilde{\boldsymbol{u}}_{k-1}$ are computed as follows:

$$\begin{gathered}\tilde{\boldsymbol{u}}_k = \boldsymbol{f}_k(\hat{\boldsymbol{x}}_k^+, \boldsymbol{u}_k, \boldsymbol{0}) - \boldsymbol{F}_k\hat{\boldsymbol{x}}_k^+ \\ \tilde{\boldsymbol{w}}_k \sim (0, \boldsymbol{L}_k\boldsymbol{Q}_k\boldsymbol{L}_k^T)\end{gathered} \tag{2.18}$$

The measurement function is linearized around $\boldsymbol{x}_k = \hat{\boldsymbol{x}}_k^-$ and $\boldsymbol{v}_k = \boldsymbol{0}$ as follows:

$$\begin{aligned}\boldsymbol{y}_k &= \boldsymbol{h}_k(\hat{\boldsymbol{x}}_k^-, \boldsymbol{0}) + \left.\frac{\partial \boldsymbol{h}_k}{\partial \boldsymbol{x}}\right|_{\hat{x}_k^-}(\boldsymbol{x}_k - \hat{\boldsymbol{x}}_k^-) + \left.\frac{\partial \boldsymbol{h}_k}{\partial \boldsymbol{v}}\right|_{\hat{x}_k^-}\boldsymbol{v}_k \\ &= \boldsymbol{h}_k(\hat{\boldsymbol{x}}_k^-, \boldsymbol{0}) + \boldsymbol{H}_k(\boldsymbol{x}_k - \hat{\boldsymbol{x}}_k^-) + \boldsymbol{M}_k\boldsymbol{v}_k \\ &= \boldsymbol{H}_k\boldsymbol{x}_k + [\boldsymbol{h}_k(\hat{\boldsymbol{x}}_k^-, \boldsymbol{0}) - \boldsymbol{H}_k\hat{\boldsymbol{x}}_k^-] + \boldsymbol{M}_k\boldsymbol{v}_k \\ &= \boldsymbol{H}_k\boldsymbol{x}_k + \boldsymbol{z}_k + \tilde{\boldsymbol{v}}_k\end{aligned} \tag{2.19}$$

where $\boldsymbol{H}_k = \left.\frac{\partial \boldsymbol{h}_k}{\partial x}\right|_{\hat{x}_k^-}$, and $\boldsymbol{M}_k = \left.\frac{\partial \boldsymbol{h}_k}{\partial v}\right|_{\hat{x}_k^-}$. The transformed measurement noise $\tilde{\boldsymbol{v}}_k$ is defined as follows:

$$\tilde{\boldsymbol{v}}_k \sim (\boldsymbol{0}, \boldsymbol{M}_k\boldsymbol{R}_k\boldsymbol{M}_k^T) \tag{2.20}$$

Equations (2.17) and (2.19) represent a linear state-space system and a linear measurement function. Therefore, Equations of the linear discrete-time Kalman filter can be employed for the state estimation. The recursive algorithm of the EKF is defined as follows:

PREDICTION

$$\begin{gathered}\hat{\boldsymbol{x}}_k^- = \boldsymbol{f}_{k-1}(\hat{\boldsymbol{x}}_{k-1}^+, \boldsymbol{u}_{k-1}, \boldsymbol{0}) \\ \boldsymbol{P}_k^- = \boldsymbol{F}_{k-1}\boldsymbol{P}_{k-1}^+\boldsymbol{F}_{k-1}^T + \boldsymbol{L}_{k-1}\boldsymbol{Q}_{k-1}\boldsymbol{L}_{k-1}^T\end{gathered} \tag{2.21}$$

CORRECTION

$$\begin{gathered}\boldsymbol{z}_k = \boldsymbol{h}_k(\hat{\boldsymbol{x}}_k^-, \boldsymbol{0}) - \boldsymbol{H}_k\hat{\boldsymbol{x}}_k^- \\ \boldsymbol{K}_k = \boldsymbol{P}_k^-\boldsymbol{H}_k^T(\boldsymbol{H}_k\boldsymbol{P}_k^-\boldsymbol{H}_k^T + \boldsymbol{M}_k\boldsymbol{R}_k\boldsymbol{M}_k^T)^{-1} \\ \hat{\boldsymbol{x}}_k^+ = \hat{\boldsymbol{x}}_k^- + \boldsymbol{K}_k(\boldsymbol{y}_k - \boldsymbol{H}_k\hat{\boldsymbol{x}}_k^- - \boldsymbol{z}_k) = \hat{\boldsymbol{x}}_k^- + \boldsymbol{K}_k\big(\boldsymbol{y}_k - \boldsymbol{h}_k(\hat{\boldsymbol{x}}_k^-, \boldsymbol{0})\big) \\ \boldsymbol{P}_k^+ = (\boldsymbol{I} - \boldsymbol{K}_k\boldsymbol{H}_k)\,\boldsymbol{P}_k^-\end{gathered} \tag{2.22}$$

The EKF consists of a predictor-corrector stochastic state estimator. The representative algorithm is summarized as follows:

1) state transition and measurement functions are given as follows:

$$\begin{gathered} \boldsymbol{x}_k = \boldsymbol{f}_{k-1}(\boldsymbol{x}_{k-1}, \boldsymbol{u}_{k-1}, \boldsymbol{w}_{k-1}) \\ \boldsymbol{y}_k = \boldsymbol{h}_k(\boldsymbol{x}_k, \boldsymbol{v}_k) \\ \boldsymbol{w}_k \sim (\boldsymbol{0}, \boldsymbol{Q}_k) \\ \boldsymbol{v}_k \sim (\boldsymbol{0}, \boldsymbol{R}_k) \end{gathered} \tag{2.23}$$

2) the EKF is initialized as follows:

$$\begin{gathered} \widehat{\boldsymbol{x}}_0^+ = E(\boldsymbol{x}_0) \\ \boldsymbol{P}_0^+ = E[(\boldsymbol{x}_0 - \widehat{\boldsymbol{x}}_0^+)(\boldsymbol{x}_0 - \widehat{\boldsymbol{x}}_0^+)^T] \end{gathered} \tag{2.24}$$

3) for $k = 1,2, \ldots$, perform the following:
   a) compute the following partial derivative matrices:

$$\begin{gathered} \boldsymbol{F}_{k-1} = \left.\frac{\partial \boldsymbol{f}_{k-1}}{\partial \boldsymbol{x}}\right|_{\widehat{\boldsymbol{x}}_{k-1}^+} \\ \boldsymbol{L}_{k-1} = \left.\frac{\partial \boldsymbol{f}_{k-1}}{\partial \boldsymbol{w}}\right|_{\widehat{\boldsymbol{x}}_{k-1}^+} \end{gathered} \tag{2.25}$$

   b) perform the prediction step as follows:

$$\begin{gathered} \boldsymbol{P}_k^- = \boldsymbol{F}_{k-1}\boldsymbol{P}_{k-1}^+\boldsymbol{F}_{k-1}^T + \boldsymbol{L}_{k-1}\boldsymbol{Q}_{k-1}\boldsymbol{L}_{k-1}^T \\ \widehat{\boldsymbol{x}}_k^- = \boldsymbol{f}_{k-1}(\widehat{\boldsymbol{x}}_{k-1}^+, \boldsymbol{u}_{k-1}, \boldsymbol{0}) \end{gathered} \tag{2.26}$$

   c) compute the following partial derivative matrices:

$$\begin{gathered} \boldsymbol{H}_k = \left.\frac{\partial \boldsymbol{h}_k}{\partial \boldsymbol{x}}\right|_{\widehat{\boldsymbol{x}}_k^-} \\ \boldsymbol{M}_k = \left.\frac{\partial \boldsymbol{h}_k}{\partial \boldsymbol{v}}\right|_{\widehat{\boldsymbol{x}}_k^-} \end{gathered} \tag{2.27}$$

   d) perform the correction step as follows:

$$\begin{gathered} \boldsymbol{K}_k = \boldsymbol{P}_k^-\boldsymbol{H}_k^T(\boldsymbol{H}_k\boldsymbol{P}_k^-\boldsymbol{H}_k^T + \boldsymbol{M}_k\boldsymbol{R}_k\boldsymbol{M}_k^T)^{-1} \\ \widehat{\boldsymbol{x}}_k^+ = \widehat{\boldsymbol{x}}_k^- + \boldsymbol{K}_k\big(\boldsymbol{y}_k - \boldsymbol{h}_k(\widehat{\boldsymbol{x}}_k^-, \boldsymbol{0})\big) \\ \boldsymbol{P}_k^+ = (\boldsymbol{I} - \boldsymbol{K}_k\boldsymbol{H}_k)\,\boldsymbol{P}_k^- \end{gathered} \tag{2.28}$$

In Figure 2.11 the algorithm of the EKF is represented considering both the process and measurement noises covariances $\boldsymbol{Q}$ and $\boldsymbol{R}$ as diagonals and constants.

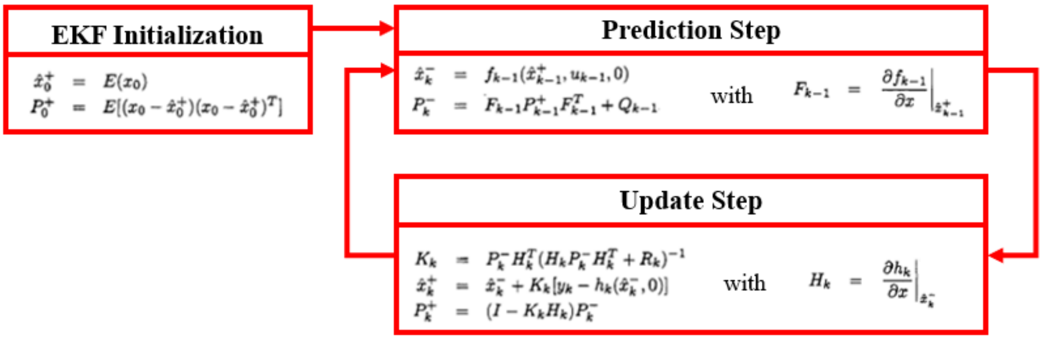

Figure 2.11. The EKF algorithm.

2.2.3. The Unscented Kalman Filter

The EKF is the most widely applied state estimation algorithm for nonlinear systems. When the system nonlinearities are severe, the EKF gives unreliable estimations.
The principal cause is the system linearization for propagating the statistics of the system state. A more accurate state estimation can be obtained by employing the Unscented Kalman Filter (UKF) to reduce the typical linearization errors produced by the EKF.

The UKF [29] has been proposed by [27] and further improved [28]. Since UKF does not require evaluating Jacobian and Hessian matrices, and has superior accuracy compared to EKF in terms of approximating the statistics of highly nonlinear systems, it is suitable for estimating fairly complex system dynamics.
The statistical properties of a random variable in the unscented transformation are described with sigma points. As a consequence, the statistical behaviour of the transformed random variable is obtained by applying the nonlinear transformation to the sigma points.
The UKF algorithm is briefly described in the following, since it has been employed for a comparative analysis. Consider the following discretized nonlinear state space system:

$$\begin{aligned} \boldsymbol{x}_{k+1} &= \boldsymbol{f}(\boldsymbol{x}_k, \boldsymbol{u}_k) + \boldsymbol{w}_k \\ \boldsymbol{y}_{k+1} &= \boldsymbol{h}(\boldsymbol{x}_{k+1}, \boldsymbol{u}_{k+1}) + \boldsymbol{v}_{k+1} \end{aligned} \tag{2.29}$$

where $\boldsymbol{x} \in \boldsymbol{R}^{\boldsymbol{n}}$ is the n-dimensional vector of system state, $\boldsymbol{f}$ and $\boldsymbol{h}$ are nonlinear functions, $\boldsymbol{u}$ is the input vector, $\boldsymbol{w}$ is the process noise characterized by the covariance $\boldsymbol{Q}$, $\boldsymbol{y} \in \boldsymbol{R}^{\boldsymbol{m}}$ is the mdimensional vector of measurement, $\boldsymbol{y}$ is the Gaussian white measurement noise with covariance $\boldsymbol{R}$ and k is the k-th time step.

The main task is to estimate the system state, i.e., calculate the mean as well as the covariance of system state at the (k+1)-th step, based on the state estimation at the k-th step and the measurements at the current (k+1)-th step.

A set of $2n+1$ sigma points $\boldsymbol{X}_{k|\,k,i}$ with associated weights $\boldsymbol{W}_i$ are chosen symmetrically about $\hat{\boldsymbol{x}}_{k|\,k}$ as follows:

$$\begin{aligned} \boldsymbol{X}_{k|\,k,0} &= \hat{\boldsymbol{x}}_{k|\,k}, \qquad \boldsymbol{W}_0 = \tfrac{k}{n+k} \\ \boldsymbol{X}_{k|\,k,i} &= \hat{\boldsymbol{x}}_{k|\,k} + \left(\sqrt{(n+k)\boldsymbol{P}_{k|\,k}}\right)_i, \qquad \boldsymbol{W}_i = \tfrac{1}{2(n+k)} \\ \boldsymbol{X}_{k|\,k,i+n} &= \hat{\boldsymbol{x}}_{k|\,k} - \left(\sqrt{(n+k)\boldsymbol{P}_{k|\,k}}\right)_i, \qquad \boldsymbol{W}_{i+n} = \tfrac{1}{2(n+k)} \end{aligned} \tag{2.30}$$

where $\left(\sqrt{\boldsymbol{P}_{k|\,k}}\right)_i$ is the ith column of the matrix square root of the error covariance matrix $\boldsymbol{P}_{k|\,k}$, $\boldsymbol{W}_i$ is the weight associated with the corresponding point and k is a tuning parameter. The set $\boldsymbol{X}$ and $\hat{\boldsymbol{x}}_{k|\,k}$ have the same weighted mean due the symmetric placement of the sigma points and since the weights $\boldsymbol{W}_i$ sum is one. Therefore, the weighted covariance matrix of the sample $\boldsymbol{X}$ is equal to $\boldsymbol{P}_{k|\,k}$:

$$\boldsymbol{P}_{k|\,k} = \sum_{i=0}^{2n} \boldsymbol{W}_{k,i}(\boldsymbol{X}_{k|\,k,i} - \hat{\boldsymbol{x}}_{k|\,k})\,(\boldsymbol{X}_{k|\,k,i} - \hat{\boldsymbol{x}}_{k|\,k})^T \tag{2.31}$$

The predicted set of sigma points are obtained by applying the nonlinear state transition function $\boldsymbol{f}(\cdot)$ to the sigma points:

$$\boldsymbol{X}_{k+1\,|\,k,i} = \boldsymbol{f}(\boldsymbol{X}_i, \boldsymbol{u}_k), \qquad i = 0,1\,, \dots, 2n \tag{2.32}$$

Given the filtered state estimates $\hat{\boldsymbol{x}}_{k|\,k}$, which have been obtained using all the measurements made up to time t_k, and the input $\boldsymbol{u}_k$, the predicted state estimates $\hat{\boldsymbol{x}}_{k+1|\,k}$ and the error covariance matrix $\boldsymbol{P}_{k+1\,|\,k}$ can be obtained as follows:

$$\begin{aligned} \hat{\boldsymbol{x}}_{k+1\,|\,k} &= \sum_{i=0}^{2n} \boldsymbol{W}_{k,i} \boldsymbol{X}_{k+1\,|\,k,i} \\ \boldsymbol{P}_{k+1\,|\,k} &= \sum_{i=0}^{2n} \boldsymbol{W}_{k,i} (\boldsymbol{X}_{k+1\,|\,k,i} - \hat{\boldsymbol{x}}_{k+1\,|\,k})\,(\boldsymbol{X}_{k+1\,|\,k,i} - \hat{\boldsymbol{x}}_{k+1\,|\,k})^T + \boldsymbol{Q}_k \end{aligned} \tag{2.33}$$

Propagation of the sigma points through the nonlinear measurement function $\boldsymbol{h}(\cdot)$ provides the predicted measurements:

$$\boldsymbol{Y}_{k+1\,|\,k,i} = \boldsymbol{h}(\boldsymbol{X}_{k+1\,|\,k,i}, \boldsymbol{u}_{k+1}), \qquad i = 0,1\,, \dots, 2n \tag{2.34}$$

and the covariance matrix of innovations and the cross-covariance matrix between predicted state estimate errors and innovations are computed as

$$\begin{aligned} \boldsymbol{P}_{yy,k+1\,|\,k} &= \sum_{i=0}^{2n} \boldsymbol{W}_{k,i} (\boldsymbol{Y}_{k+1\,|\,k,i} - \hat{\boldsymbol{y}}_{k+1\,|\,k})\,(\boldsymbol{Y}_{k+1\,|\,k,i} - \hat{\boldsymbol{y}}_{k+1\,|\,k})^T + \boldsymbol{R}_{k+1} \\ \boldsymbol{P}_{xy,k+1\,|\,k} &= \sum_{i=0}^{2n} \boldsymbol{W}_{k,i} (\boldsymbol{X}_{k+1\,|\,k,i} - \hat{\boldsymbol{x}}_{k+1\,|\,k})\,(\boldsymbol{Y}_{k+1\,|\,k,i} - \hat{\boldsymbol{y}}_{k+1\,|\,k})^T \end{aligned} \tag{2.35}$$

where

$$\hat{\boldsymbol{y}}_{k+1\,|\,k} = \sum_{i=0}^{2n} \boldsymbol{W}_{k,i} \boldsymbol{Y}_{k+1\,|\,k,i} \tag{2.36}$$

Finally, the updated state estimates and the error covariance matrix of updated state estimates are

$$\begin{aligned} \hat{\boldsymbol{x}}_{k+1\,|\,k+1} &= \hat{\boldsymbol{x}}_{k+1\,|\,k} + \boldsymbol{K}_{k+1} (\boldsymbol{y}_{k+1} - \hat{\boldsymbol{y}}_{k+1\,|\,k}) \\ \boldsymbol{P}_{k+1\,|\,k+1} &= \boldsymbol{P}_{k+1\,|\,k} - \boldsymbol{K}_{k+1} \boldsymbol{P}_{yy,k+1\,|\,k} \boldsymbol{K}_{k+1}^T \end{aligned} \tag{2.37}$$

where

$$\boldsymbol{K}_{k+1} = \boldsymbol{P}_{xy,k+1\,|\,k} (\boldsymbol{P}_{yy,k+1\,|\,k})^{-1} \tag{2.38}$$

is the Kalman gain matrix.

2.2.4. The Constrained Unscented Kalman Filter

The CUKF is used to improve the accuracy of estimation of the UKF, taking into account constraints of state variables. The employment of this estimator is required to take into account the non-linearities of the system that are introduced as elements of an augmented state vector [29]. The CUKF is a two-step estimator, particularly functional for real-time process [29,35]. It uses the unscented transformation to propagate the state and the estimation error covariance over time. The state distribution is represented by a Gaussian Random Variable (GRV) and the unscented transformation completely captures, through the sigma points, the true mean and covariance of the GRV that characterizes the state.

The sigma points are propagated through a nonlinear transformation to obtain the statistical behaviour of the transformed GRV of the state.

The CUKF algorithm is briefly described in the following. Consider the following discretized nonlinear state space system:

$$\begin{aligned} \boldsymbol{x}_{k+1} &= \boldsymbol{f}(\boldsymbol{x}_k, \boldsymbol{u}_k) + \boldsymbol{w}_k \\ \boldsymbol{y}_{k+1} &= \boldsymbol{h}(\boldsymbol{x}_{k+1}, \boldsymbol{u}_{k+1}) + \boldsymbol{v}_{k+1} \end{aligned} \tag{2.39}$$

where $\boldsymbol{x} \in \mathbb{R}^n$ is the n-dimensional vector of system state, $\boldsymbol{f}$ and $\boldsymbol{h}$ are nonlinear functions, $\boldsymbol{u}$ is the input vector, $\boldsymbol{w}$ is the white process noise characterized by the covariance $\boldsymbol{Q}$, $\boldsymbol{y} \in \mathbb{R}^{\boldsymbol{m}}$ is the m-dimensional vector of measurement, $\boldsymbol{v}$ is the Gaussian white measurement noise with covariance $\boldsymbol{R}$ and k is the k-th time step. $(\hat{\bullet})$ being the estimations, the following initializing conditions are considered for the estimated state (2.40) and for the error covariance (2.41):

$$\hat{\boldsymbol{x}}_0 = E(\boldsymbol{x}_0) \tag{2.40}$$

$$P_0 = E(\boldsymbol{x}_0 - \hat{\boldsymbol{x}}_0)(\boldsymbol{x}_0 - \hat{\boldsymbol{x}}_0)^T \tag{2.41}$$

with E the expected value. These two conditions can be determined if all the measurements before (but not including) time k are available. In addition to Equation (2.39), bound constraints are applied to the states as:

$$\boldsymbol{x}_L \leq \boldsymbol{x} \leq \boldsymbol{x}_U \tag{2.42}$$

The employment of state constraints, expressed by the Eq. (2.42), allows to limit the variability of the estimated states, taking into account their physical acceptance limits.

The sigma points [30] are a set of points, whose sample mean and sample covariance are $\hat{\boldsymbol{x}}_{k \mid k}$ and $\boldsymbol{P}_{k \mid k}$, respectively. A set of $2n+1$ sigma points $\boldsymbol{X}_{k|k,i}$ are selected along the following directions to compute the statistics of $\hat{\boldsymbol{x}}$:

$$\boldsymbol{s}_{i,k} = \left(\sqrt{\boldsymbol{P}_{k \mid k}}\right)_i ; \quad \boldsymbol{s}_{n+1,k} = -\left(\sqrt{\boldsymbol{P}_{k \mid k}}\right)_i \tag{2.43}$$

where $\left(\sqrt{\boldsymbol{P}_{k \mid k}}\right)_i$ is the i-th column of the matrix square root of the error covariance matrix $\boldsymbol{P}_{k \mid k}$ corresponding to the estimated state $\hat{\boldsymbol{x}}_{k \mid k}$ at time instant 'k'. The step sizes $\boldsymbol{\theta}_{k,i}$ for all sigma points, for the simple case when only bound constraints are considered, can be performed as follows [33]:

$$\begin{aligned}
&\boldsymbol{\theta}_{k,i} = \boldsymbol{\theta}_{k,n+i} = min(\boldsymbol{\theta}^C_{k,i}, \boldsymbol{\theta}^C_{k,n+i}), && i = 1, \dots, n \\
&\boldsymbol{\theta}^C_{k,i} = min(\sqrt{n+\kappa}, \boldsymbol{\theta}^U_{k,i}, \boldsymbol{\theta}^L_{k,i}), && i = 1, \dots, 2n \\
&\boldsymbol{\theta}^U_{k,i} = min\left(\infty, \frac{(\boldsymbol{x}_U)_j - (\hat{\boldsymbol{x}}_{k \mid k})_j}{(\boldsymbol{s}_{k,i})_j}\right), \text{ if } (\boldsymbol{s}_{k,i})_j > 0, && i = 1, \dots, 2n \\
&\boldsymbol{\theta}^L_{k,i} = min\left(\infty, \frac{(\boldsymbol{x}_L)_j - (\hat{\boldsymbol{x}}_{k \mid k})_j}{(\boldsymbol{s}_{k,i})_j}\right), \text{ if } (\boldsymbol{s}_{k,i})_j < 0, && i = 1, \dots, 2n
\end{aligned} \tag{2.44}$$

where the subscript j represents the j-th element of vector $\boldsymbol{x}$ and κ is a tuning parameter that incorporates high order information.

The CUKF algorithm ensures that all the sigma points are within the bounds on state variables. Using a linear weighting method proposed in [32], the weights of all of sigma points are defined as follows:

$$\begin{aligned}
\boldsymbol{W}_{k,0} &= b, \quad i = 0 \\
\boldsymbol{W}_{k,i} &= a\boldsymbol{\theta}_{k,i} + b, \quad i = 1, \dots, 2n
\end{aligned} \tag{2.45}$$

where

$$\begin{aligned}
a &= \frac{2\kappa\text{-}1}{2(n+\kappa)[s_k - (2n+1)\sqrt{n+\kappa}]} \\
b &= \frac{1}{2(n+\kappa)} - \frac{2\kappa\text{-}1}{2\sqrt{n+\kappa}[s_k - (2n+1)\sqrt{n+\kappa}]}
\end{aligned} \tag{2.46}$$

$$s_k = \sum_{i=1}^{2n} \boldsymbol{\theta}_{k,i}$$

The sigma points are calculated, therefore, as follows:

$$\begin{gathered} \boldsymbol{X}_{k\,|\,k,0} = \widehat{\boldsymbol{x}}_{k\,|\,k} \\ \boldsymbol{X}_{k\,|\,k,i} = \widehat{\boldsymbol{x}}_{k\,|\,k} + \boldsymbol{\theta}_{k,i}\boldsymbol{s}_{i,k} \end{gathered}$$

and

$$\boldsymbol{X}_{k\,|\,k,i+n} = \widehat{\boldsymbol{x}}_{k\,|\,k} + \boldsymbol{\theta}_{k,i}\boldsymbol{s}_{n+1,k} \tag{2.47}$$

The weighted covariance matrix of the sample $\boldsymbol{X}$ is equal to $\boldsymbol{P}_{k\,|\,k}$:

$$\boldsymbol{P}_{k|\,k} = \sum_{i=0}^{2n} \boldsymbol{W}_{k,i}(\boldsymbol{X}_{k|\,k,i} - \widehat{\boldsymbol{x}}_{k|\,k})\,(\boldsymbol{X}_{k|\,k,i} - \widehat{\boldsymbol{x}}_{k|\,k})^T \tag{2.48}$$

Applying the nonlinear state transition function to the sigma points, the predicted set of sigma points are obtained as follows:

$$\boldsymbol{X}_{k+1\,|\,k,i} = \boldsymbol{f}(\boldsymbol{X}_{k\,|\,k,i}, \boldsymbol{u}_k), \qquad i = 0,1\,, \dots, 2n \tag{2.49}$$

and the predicted state estimation and the relative error covariance matrix are

$$\begin{gathered} \widehat{\boldsymbol{x}}_{k+1\,|\,k} = \sum_{i=0}^{2n} \boldsymbol{W}_{k,i}\boldsymbol{X}_{k+1\,|\,k,i} \\ \boldsymbol{P}_{k+1\,|\,k} = \sum_{i=0}^{2n} \boldsymbol{W}_{k,i}(\boldsymbol{X}_{k+1\,|\,k,i} - \widehat{\boldsymbol{x}}_{k+1\,|\,k})\,(\boldsymbol{X}_{k+1\,|\,k,i} - \widehat{\boldsymbol{x}}_{k+1\,|\,k})^T + \boldsymbol{Q}_k \end{gathered} \tag{2.50}$$

The sigma points that are not contained within the bound constraints are moved onto the bounds during the prediction step, while the sigma points within the boundary are moved consequently to make the distribution of the new set of sigma points around the GRV $\boldsymbol{x}$.

Propagation of the sigma points through the nonlinear measurement equation provides the predicted measurements:

$$\boldsymbol{\Upsilon}_{k+1\,|\,k,i} = \boldsymbol{h}(\boldsymbol{X}_{k+1\,|\,k,i}, \boldsymbol{u}_{k+1}), \qquad i = 0,1\,,\dots,2n \tag{2.51}$$

and the covariance matrix of innovations and the cross-covariance matrix between predicted state estimation errors and innovations are computed as:

$$\begin{gathered}
\boldsymbol{P}_{yy,k+1\,|\,k} = \sum_{i=0}^{2n} \boldsymbol{W}_{k,i}(\boldsymbol{\Upsilon}_{k+1\,|\,k,i} - \widehat{\boldsymbol{y}}_{k+1\,|\,k})\,(\boldsymbol{\Upsilon}_{k+1\,|\,k,i} - \widehat{\boldsymbol{y}}_{k+1\,|\,k})^T + \boldsymbol{R}_{k+1} \\
\boldsymbol{P}_{xy,k+1\,|\,k} = \sum_{i=0}^{2n} \boldsymbol{W}_{k,i}(\boldsymbol{X}_{k+1\,|\,k,i} - \widehat{\boldsymbol{x}}_{k+1\,|\,k})\,(\boldsymbol{\Upsilon}_{k+1\,|\,k,i} - \widehat{\boldsymbol{y}}_{k+1\,|\,k})^T
\end{gathered} \tag{2.52}$$

where

$$\widehat{\boldsymbol{y}}_{k+1\,|\,k} = \sum_{i=0}^{2n} \boldsymbol{W}_{k,i}\boldsymbol{\Upsilon}_{k+1\,|\,k,i} \tag{2.53}$$

Finally, by computing the Kalman Gain

$$\boldsymbol{K}_{k+1} = \boldsymbol{P}_{xy,k+1\,|\,k}(\boldsymbol{P}_{yy,k+1\,|\,k})^{-1} \tag{2.54}$$

it is possible to update the estimated states and the relative error covariance matrix. The transformed sigma points, for the constrained state estimation, are determined by means of Kalman updating equation:

$$\boldsymbol{X}_{k+1\,|\,k+1,i} = \boldsymbol{X}_{k+1\,|\,k,i} + \boldsymbol{K}_{k+1}\,(\boldsymbol{y}_{k+1} - \boldsymbol{\Upsilon}_{k+1\,|\,k,i}), \;\; i = 0,1\,,\dots,2n \tag{2.55}$$

in accordance with the method proposed in [32].

The transformed sigma points are obtained by the updating equation in the correction step. When the update state estimation exceeds the boundary, some transformed sigma points that violate bound constraints are projected to constraints [34].

With $\boldsymbol{X}_{k+1\,|\,k+1,i}$ calculated by Equation (2.55), the state update $\widehat{\boldsymbol{x}}_{k+1\,|\,k+1}$ and its covariance $\boldsymbol{P}_{k+1\,|\,k+1}$ can be calculated using the following equations:

$$
\begin{aligned}
\hat{\boldsymbol{x}}_{k+1\,|\,k+1} &= \sum_{i=0}^{2n} \boldsymbol{W}_{k,i} \boldsymbol{X}_{k+1\,|\,k+1,i} \\
\boldsymbol{P}_{k+1\,|\,k+1} &= \sum_{i=0}^{2n} \boldsymbol{W}_{k,i} \left(\boldsymbol{X}_{k+1\,|\,k+1,i} - \hat{\boldsymbol{x}}_{k+1\,|\,k+1}\right)\left(\boldsymbol{X}_{k+1\,|\,k+1,i} - \hat{\boldsymbol{x}}_{k+1\,|\,k+1}\right)^T \\
&\quad + \boldsymbol{Q}_k + \boldsymbol{K}_{k+1} \boldsymbol{R}_{k+1} \boldsymbol{K}_{k+1}^T
\end{aligned}
\tag{2.56}
$$

The choice of constraints in the CUKF is naturally connected to the estimation model and the variability of these states.

Figure 2.12 summarizes the discrete-time form of the CUKF algorithm.

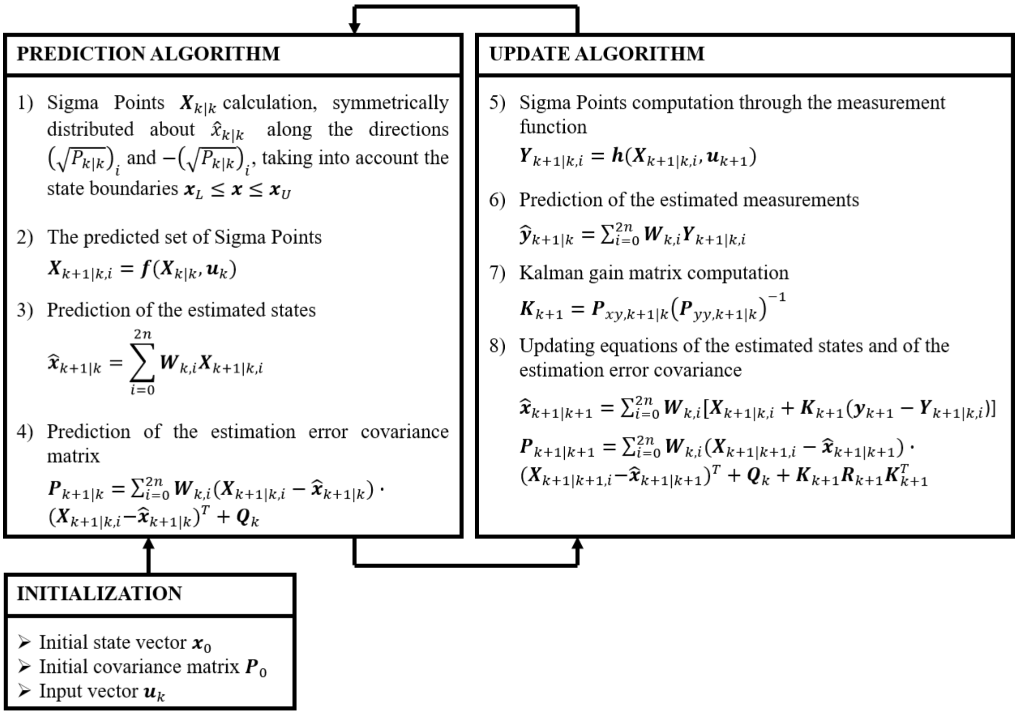

Figure 2.12. The CUKF algorithm.

2.2.5 Parameter estimation through nonlinear Kalman Filters

State estimation theory can be employed to estimate states and unknown parameters of a system [29]. The state transition function representative of the system to be monitored becomes nonlinear when unknown parameters are introduced in the estimation process.

The state transition function is also called the estimator design model.

Consider a discrete-time system model having system matrices dependent in a nonlinear way on an unknown parameter vector $\boldsymbol{p}$:

$$\begin{gathered}\boldsymbol{x}_{k+1} = \boldsymbol{F}_k(\boldsymbol{p})\boldsymbol{x}_k + \boldsymbol{G}_k(\boldsymbol{p})\boldsymbol{u}_k + \boldsymbol{L}_k(\boldsymbol{p})\boldsymbol{w}_k \\ \boldsymbol{y}_k = \boldsymbol{H}_k(\boldsymbol{p})\boldsymbol{x}_k + \boldsymbol{v}_k\end{gathered} \tag{2.57}$$

For notational convenience in the model (Equation (2.57)) is assumed that the measurement is independent of $\boldsymbol{p}$. The dependence of $\boldsymbol{y}_k$ on $\boldsymbol{p}$ can be included easily for parameter estimation purposes.

For obtaining the estimation of the parameter $\boldsymbol{p}$, the vector $\boldsymbol{p}$ is inserted in the state vector $\boldsymbol{x}$, to obtain the augmented state vector $\boldsymbol{x}'$

$$\boldsymbol{x}'_k = \begin{bmatrix}\boldsymbol{x}_k \\ \boldsymbol{p}_k\end{bmatrix} \tag{2.58}$$

If $\boldsymbol{p}_k$ is constant, then

$$\boldsymbol{p}_{k+1} = \boldsymbol{p}_k + \boldsymbol{w}_{pk} \tag{2.59}$$

where $\boldsymbol{p}_k$ is the estimated parameter vector at time instant *k*, and $\boldsymbol{w}_{pk}$ is a small artificial noise term that allows the Kalman filter to change its estimation of $\boldsymbol{p}_k$.

The augmented system model can be written as

$$\boldsymbol{x}'_{k+1} = \begin{bmatrix} \boldsymbol{F}_k(\boldsymbol{p}_k)\boldsymbol{x}_k + \boldsymbol{G}_k(\boldsymbol{p}_k)\boldsymbol{u}_k + \boldsymbol{L}_k(\boldsymbol{p}_k)\boldsymbol{w}_k \\ \boldsymbol{p}_k + \boldsymbol{w}_{pk} \end{bmatrix} = \boldsymbol{f}(\boldsymbol{x}'_k, \boldsymbol{u}_k, \boldsymbol{w}_k, \boldsymbol{w}_{pk})$$
$$\boldsymbol{y}_k = [\boldsymbol{H}_k \quad \boldsymbol{0}] \begin{bmatrix} \boldsymbol{x}_k \\ \boldsymbol{p}_k \end{bmatrix} + \boldsymbol{v}_k \tag{2.60}$$

The augmented state transition function $\boldsymbol{f}(\boldsymbol{x}'_k, \boldsymbol{u}_k, \boldsymbol{w}_k, \boldsymbol{w}_{pk})$ is a nonlinear function of the augmented state $\boldsymbol{x}'_k$. Therefore, the linear Kalman Filter cannot be employed for estimating unknown system parameters included in the augmented state $\boldsymbol{x}'_k$.
Any nonlinear Kalman Filter can be used to estimate the augmented state $\boldsymbol{x}'_k$.

The possibility to estimate system parameters constitutes a methodology for monitoring mechanical systems.
The knowledge at each time instant of one or more parameters values allows to monitor mechanical systems, as an example, based on a known value of the monitoring parameter. Abnormal variations of the estimated parameters from the known one is indicative of fault or malfunctions presences.

3. DEVELOPMENT OF ESTIMATOR DESIGN MODELS FOR MODEL-BASED MONITORING SYSTEMS

Model-based estimation techniques for monitoring purposes, such as Kalman Filters, require the modelling of the system to be monitored for making estimations.

In particular, the prediction step of Kalman Filters is based on the previously mentioned modelling constituting the state transition function, typically called the estimator design model. The condition monitoring of mechanical systems through model-based estimators is made by estimating state variables and parameters indicative of operative, health and degradation conditions of systems to be monitored.

The development of estimator design models able to capture the fundamental dynamics of the real system is crucial for obtaining reliable estimations through model-based monitoring systems such as Kalman Filters. Therefore, three general aspects have to be taken into account for developing reliable model-based estimators for monitoring purposes of mechanical systems:

- *sufficient accuracy and reliability of estimations*: the monitoring system must be able to indicate the current actual state of vital components with sufficient accuracy, ensuring the prompt detection of faults and false alarms, which negatively impact economic efficiency and cull the reliability of the monitored mechanical system. Furthermore, the model-based estimator must be able to detect the current state of components to be monitored without having direct access to those latter through information obtainable from the estimator design model and sensors not connected to the components concerned;
- *low computational effort*: the algorithm, representing the model-based estimator, must be carried out very fast to obtain the typically sought requirement of real-time applicability. Mobile systems, such as railway and road vehicles, must carry small and lightweight electronic control units with reduced energy consumption;
- *recursive-based modelling approach*: the estimator design model must be developed in a strictly connected way with the requirement of a low computational effort. Therefore, the estimator design model must be simple by describing the dynamics of mechanical systems to be monitored through physical or stochastics reduced order models. The estimator design model constitutes the state transition function of Kalman Filters.

Therefore, the estimator design model must respect the recursiveness of Kalman Filters algorithms, avoiding iterative modelling approaches. Indeed, estimator design models are typically developed through physical law based on ordinary differential equations, which preserve the recursiveness property.

In this work, nonlinear Kalman Filters are employed as monitoring tools for mechanical systems concerning railway vehicles, road vehicles and seismic isolators.
A description of the developed estimator design models to be included in nonlinear Kalman Filters for monitoring purposes of previously mentioned mechanical systems is provided in this chapter.

3.1 Estimator design model for monitoring railway anti-yaw suspension components

The model-based monitoring approach developed for monitoring the health conditions of anti-yaw dampers of railway vehicles consists of a Constrained Unscented Kalman Filter (CUKF). The estimator design model developed for inclusion in the CUKF for making estimations has to be able to describe the railway vehicle dynamics with sufficient accuracy.
At the same time, it has to be simple to enable a low computational load. Some physical considerations are important to design the estimator correctly.
Different types of hunting motions are observable in railway vehicles. Carbody hunting motion is characterized by relatively large lateral and yaw ones of the carbody and a relatively low hunting frequency of around 1 Hz [115]. Bogie hunting is characterized by small motions of the carbody and a higher hunting frequency starting around 4 Hz and grows notably with the running speed. For a higher hunting frequency, the lateral acceleration of wheelsets and, therefore, the lateral wheel-rail guiding forces increase (Figure 3.1). Due to the higher lateral wheel-rail forces, bogie hunting is more dangerous than carbody hunting. Carbody and bogie hunting motions strictly depend on different factors related to the mechanical design of the vehicle, including the stiffness and damping parameters of the suspension, the wheel-rail contact geometry and the running speed.

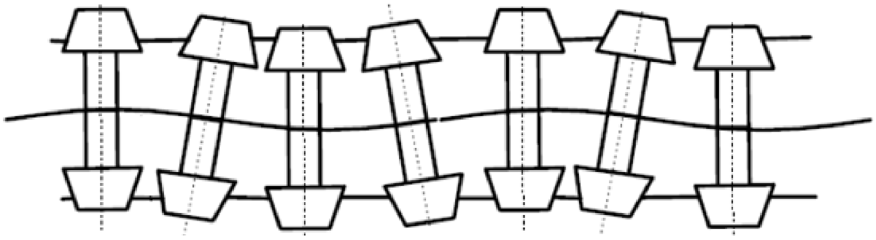

Figure 3.1. Hunting oscillation of a wheelset.

The estimator design model is developed considering bogie hunting because it is more dangerous than the carbody one due to the higher lateral wheel-rail forces. The bogie hunting motion is more critical regarding operational safety. The bogie hunting generates small motions of the carbody, which weakens the coupling between the carbody and the two bogies. Therefore, the interaction between the two bogies can be neglected, allowing for considering only one bogie in the estimator design model.

The estimator design model is constituted by a half vehicle body. The assumption of employing the half carbody is acceptable for developing the estimator design model because it is designed in a scenario of bogie hunting, in which the lateral translation and the yaw rotation of the carbody are very small. Therefore, the lateral translation is considered, observed and measured at the pivot (connection point between the carbody and the leading bogie in Figure 3.2). The yaw rotation of the half carbody is neglected. The half carbody, the leading bogie frame, and two wheelsets of a detailed full-body railway vehicle model are the components of the estimator design model. The half vehicle body model has seven degrees of freedom (DOF). The considered DOF for each body are summarized in Table 3.1. Furthermore, the considered lateral and yaw motions in the estimator design model are coupled by the hunting motion of the wheelsets, defined as a motion composed of lateral translations and yaw rotations, and by the design of the bogie.

Table 3.1. DOF for each body of the estimator design model.

Body	***DOF***
Half carbody (bd)	Lateral displacement (y_{bd})
Leading bogie frame (b)	Lateral displacement (y_b) Yaw angle (ψ_b)
Leading wheelset (w_1)	Lateral displacement (y_{w1}) Yaw angle (ψ_{w1})
Trailing wheelset (w_2)	Lateral displacement (y_{w2}) Yaw angle (ψ_{w2})

The half vehicle body model has been considered to describe the fundamental lateral and yaw dynamics that affect the guidance of the railway vehicle, resulting forces and moments acting between the wheelsets and the track, and the measurements that can be made on board.

Therefore, the longitudinal dynamics is neglected based on its decoupling from both lateral translations and yaw rotations due to the symmetric structure of the bogie concerning the longitudinal-vertical plane and the linearity of springs and dampers of primary and secondary suspensions considered in the estimator design model. With reference to Figure 3.2, the estimator design model is based on the railway vehicle dynamics [23,116]. The developed estimator design model is a mechanical model based on the multibody approach, which constitutes the standard method for modelling the dynamics of railway vehicles. The half vehicle body model is described by the following equations:

$$\begin{cases} m_{bd}\,\ddot{y}_{bd} = k_{dy}\,y_b - k_{dy}\,y_{bd} - C_{dy}\,\dot{y}_{bd} + C_{dy}\,\dot{y}_b \\ m_b\,\ddot{y}_b = k_y\,y_{w1} + k_y\,y_{w2} - 2k_y\,y_b - k_{dy}\,y_b + k_{dy}\,y_{bd} + C_y\,\dot{y}_{w1} + C_y\,\dot{y}_{w2} - 2C_y\,\dot{y}_b - C_{dy}\,\dot{y}_b + C_{dy}\,\dot{y}_{bd} \\ I_b\,\ddot{\psi}_b = a\,k_y\,y_{w1} + k_x\,b^2\,\psi_{w1} - a\,k_y\,y_{w2} + k_x\,b^2\,\psi_{w2} + a\,C_y\,\dot{y}_{w1} - a\,C_y\,\dot{y}_{w2} + C_x\,b^2\,\dot{\psi}_{w1} + \\ \qquad C_x\,b^2\,\dot{\psi}_{w2} - K_{axd}\,{l_{wb1}}^2\,\psi_b - C_{axd}\,{l_{wb}}^2\,\dot{\psi}_b - 2k_x\,b^2\,\psi_b - 2k_y\,a^2\,\psi_b - 2C_x\,b^2\,\dot{\psi}_b - 2C_y\,a^2\,\dot{\psi}_b \\ m_{w1}\,\ddot{y}_{w1} = F_{yw1} - k_y\,y_{w1} + k_y\,y_b + a\,k_y\,\psi_b - C_y\,\dot{y}_{w1} + C_y\,\dot{y}_b + a\,C_y\,\dot{\psi}_b \\ m_{w2}\,\ddot{y}_{w2} = F_{yw2} - k_y\,y_{w2} + k_y\,y_b - a\,k_y\,\psi_b - C_y\,\dot{y}_{w2} + C_y\,\dot{y}_b - a\,C_y\,\dot{\psi}_b \\ I_{w1}\,\ddot{\psi}_{w1} = M_{w1} - k_x\,b^2\,\psi_{w1} + k_x\,b^2\,\psi_b - C_x\,b^2\,\dot{\psi}_{w1} + C_x\,b^2\,\dot{\psi}_b \\ I_{w2}\,\ddot{\psi}_{w2} = M_{w2} - k_x\,b^2\,\psi_{w2} + k_x\,b^2\,\psi_b - C_x\,b^2\,\dot{\psi}_{w2} + C_x\,b^2\,\dot{\psi}_b \end{cases} \tag{3.1}$$

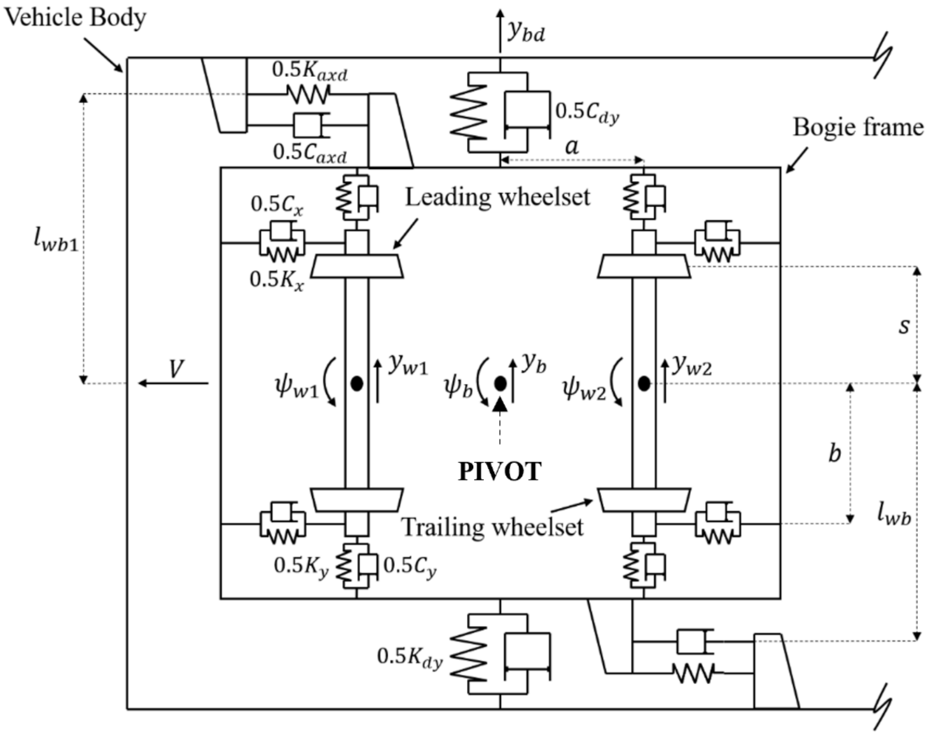

Figure 3.2. Plan view of half vehicle body.

where F_{ywi} is the resulting lateral contact force (normal and tangential) acting on the wheelset (i=1 for the leading wheelset and i=2 for the trailing wheelset) including both contacts, M_{wi} is the total moment due to the contact forces on the wheelset, y_{wi} is the lateral displacement of the wheelset, y_b and y_{bd} are the lateral displacements of the bogie frame and vehicle body, respectively, ψ_{wi} is the yaw angle of the wheelset, ψ_b is the yaw angle of the bogie frame.

This kind of model has to be completed with a wheel-rail contact force and anti-yaw damping estimator in order to have a complete estimator design model.

A random walk model (RWM) approach, already known in other fields of the engineering [26,55], has been employed to estimate the wheel-rail contact forces without using a specific contact force model.

This approach takes into account of the parameters variation that influence the wheel-rail contact and is independent of track irregularities. The RWM is based on a model characterized by random approach on the force and moments and on their first-time derivative:

$$\begin{bmatrix} \dot{f}_1 \\ \dot{f}_0 \end{bmatrix} = \begin{bmatrix} 0 & 0 \\ 1 & 0 \end{bmatrix} \begin{bmatrix} f_1 \\ f_0 \end{bmatrix} + \boldsymbol{w}_f \tag{3.2}$$

where f_0 represents the force (or moment) to be estimated, f_1 its first-time derivative, and $\boldsymbol{w}_f$ is the random white noise.

The RWM technique allows for equipping the estimator with no specific model of the wheel-rail contact behaviour.

The wheel-rail contact forces, moments and their first-time derivative are considered as states of an augmented state vector [29].

The augmented state approach is also used to estimate the anti-yaw damping by means of a parametric estimation strategy [29]. At this step, the complete estimator design model, based on the introduced random walk model and on the parametric estimation of the anti-yaw damping, in continuous time domain can be given by:

$$
\begin{cases}
m_{bd}\,\ddot{y}_{bd} = k_{dy}\,y_b - k_{dy}\,y_{bd} - C_{dy}\,\dot{y}_{bd} + C_{dy}\,\dot{y}_b \\
m_b\,\ddot{y}_b = k_y\,y_{w1} + k_y\,y_{w2} - 2k_y\,y_b - k_{dy}\,y_b + k_{dy}\,y_{bd} + C_y\,\dot{y}_{w1} + C_y\,\dot{y}_{w2} - 2C_y\,\dot{y}_b - C_{dy}\,\dot{y}_b + C_{dy}\,\dot{y}_{bd} \\
I_b\,\ddot{\psi}_b = a\,k_y\,y_{w1} + k_x\,b^2\,\psi_{w1} - a\,k_y\,y_{w2} + k_x\,b^2\,\psi_{w2} + a\,C_y\,\dot{y}_{w1} - a\,C_y\,\dot{y}_{w2} + C_x\,b^2\,\dot{\psi}_{w1} + \\
\qquad C_x\,b^2\,\dot{\psi}_{w2} - K_{axd}\,{l_{wb1}}^2\,\psi_b - C_{axd}\,{l_{wb}}^2\,\dot{\psi}_b - 2k_x\,b^2\,\psi_b - 2k_y\,a^2\,\psi_b - 2C_x\,b^2\,\dot{\psi}_b - 2C_y\,a^2\,\dot{\psi}_b \\
m_{w1}\,\ddot{y}_{w1} = F_{yw1} - k_y\,y_{w1} + k_y\,y_b + a\,k_y\,\psi_b - C_y\,\dot{y}_{w1} + C_y\,\dot{y}_b + a\,C_y\,\dot{\psi}_b \\
m_{w2}\,\ddot{y}_{w2} = F_{yw2} - k_y\,y_{w2} + k_y\,y_b - a\,k_y\,\psi_b - C_y\,\dot{y}_{w2} + C_y\,\dot{y}_b - a\,C_y\,\dot{\psi}_b \\
I_{w1}\,\ddot{\psi}_{w1} = M_{w1} - k_x\,b^2\,\psi_{w1} + k_x\,b^2\,\psi_b - C_x\,b^2\,\dot{\psi}_{w1} + C_x\,b^2\,\dot{\psi}_b \\
I_{w2}\,\ddot{\psi}_{w2} = M_{w2} - k_x\,b^2\,\psi_{w2} + k_x\,b^2\,\psi_b - C_x\,b^2\,\dot{\psi}_{w2} + C_x\,b^2\,\dot{\psi}_b \\
\dot{F}_{yw1d} = 0 \\
\dot{F}_{yw1} = F_{yw1d} \\
\dot{F}_{yw2d} = 0 \\
\dot{F}_{yw2} = F_{yw2d} \\
\dot{M}_{w1d} = 0 \\
\dot{M}_{w1} = M_{w1d} \\
\dot{M}_{w2d} = 0 \\
\dot{M}_{w2} = M_{w2d} \\
\dot{C}_{axd} = 0
\end{cases}
\tag{3.3}
$$

F_{ywi} is the resulting lateral contact force acting on the wheelset and F_{ywid} is its first-time derivative, M_{wi} is the total moment on the wheelset due to the contact forces and M_{wid} is its first-time derivative (i=1,2 for the front and the rear wheelset, respectively).

So, the state vector of the proposed estimator design model is given by:

$$
\boldsymbol{x} = \begin{bmatrix} \dot{y}_{bd}, y_{bd}, \dot{y}_b, y_b, \dot{\psi}_b, \psi_b, \dot{y}_{w1}, y_{w1}, \dot{y}_{w2}, y_{w2}, \dot{\psi}_{w1}, \psi_{w1}, \dot{\psi}_{w2}, \psi_{w2}, F_{yw1d}, F_{yw1}, F_{yw2d}, \\ F_{yw2}, M_{w1d}, M_{w1}, M_{w2d}, M_{w2}, C_{axd} \end{bmatrix}^T
\tag{3.4}
$$

The symbols and the parameters values are given in Table 3.2 and refer to a simplified model of the Eurofima passenger coach [117], which is based on a detailed model described in a report [118] by the European Railway Research Institute (ERRI).

Table 3.2. Parameters of Eurofima railway vehicle for the estimator design model.

Symbol	***Description***	***Value***
m_{w1}, m_{w2}	leading wheelsets mass	1503 kg
I_{w1}, I_{w2}	leading wheelsets yaw inertia	810 kg m^2
m_b	bogie frame mass	2615 kg
I_b	bogie frame yaw inertia	3087 kg m^2
m_{bd}	half vehicle body mass	0.5×32000 kg
k_x	primary longitudinal stiffness per wheelset	2×31391 kN/m
k_y	primary lateral stiffness per wheelset	2×3884 kN/m
C_x	primary longitudinal damping per wheelset	2×15 kNs/m
C_y	primary lateral damping per wheelset	2×15 kNs/m
k_{axd}	anti-yaw stiffness per bogie frame	2×161.7 kN/m
k_{dy}	secondary lateral stiffness per bogie frame	2×160 kN/m
C_{dy}	secondary lateral damping per bogie frame	2×20 kNs/m
C_{axd}	anti-yaw damping per bogie frame in no fault condition	2×175 kNs/m
a	distance of the wheelset from the bogie frame centre of gravity	1.28 m
b	lateral semi distance of primary suspension	1 m
l_{wb}	lateral position of bogie frame end of anti-yaw damper from bogie frame centre	1.41 m
l_{wb1}	lateral position of bogie frame end of secondary lateral stiffness from bogie frame centre	1 m
s	half of wheelset contact distance	0.75 m

The CUKF has been designed from Equation (3.3) taking into account that the measurements come from two different configurations of sensors mounted on the vehicle.

The first configuration is composed of four accelerometers, which measure translational accelerations, and one gyroscope, which measures angular velocities. These five sensors in total measure the lateral accelerations $\ddot{y}_{w1}$ and $\ddot{y}_{w2}$ of the two wheelsets, the lateral acceleration $\ddot{y}_b$ and the yaw angular velocity $\dot{\psi}_b$ of the bogie frame and the lateral acceleration $\ddot{y}_{bd}$ of the vehicle body at the pivot. The second configuration is composed of three sensors: one gyroscope and two accelerometers to measure the motions of the bogie frame $\ddot{y}_b$ and $\dot{\psi}_b$ and of the carbody $\ddot{y}_{bd}$, but not the accelerations $\ddot{y}_{w1}$ and $\ddot{y}_{w2}$ of the two wheelsets.

The configuration with three sensors has been considered to avoid possible corrupted measurements obtainable between wheelsets and rails through accelerometers. Axle boxes, constituting unsuspended masses in railway vehicles, are included in the structure of wheelsets. Typically, accelerometers are mounted on axle boxes. Therefore, since the wheel-rail contact is very stiff, there is practically no suspension action between the wheelset and the track. As a result, the wheelsets follow each track's irregularity, and, especially at high running speeds, very high accelerations occur, corrupting measurements produced by accelerometers.

The measurement vector of the proposed estimator design model using the five sensors configuration, is given by:

$$\boldsymbol{y} = [\ddot{y}_{bd}, \ddot{y}_b, \ddot{y}_{w1}, \ddot{y}_{w2}, \dot{\psi}_b]^T \tag{3.5}$$

while the measurement vector by considering a three sensors configuration is:

$$\boldsymbol{y} = [\ddot{y}_{bd}, \ddot{y}_b, \dot{\psi}_b]^T \tag{3.6}$$

Measurements are provided to the CUKF by obtaining them from a detailed multibody model of an entire railway vehicle developed with the software SIMPACK [119].
The discrete time form of the estimator design model is described by the following equations:

$$\begin{aligned} \boldsymbol{x}_{k+1} &= \boldsymbol{f}(\boldsymbol{x}_k) + \boldsymbol{w}_k \\ \boldsymbol{y}_{k+1} &= \boldsymbol{h}(\boldsymbol{x}_{k+1}) + \boldsymbol{v}_{k+1} \end{aligned} \tag{3.7}$$

where $\boldsymbol{f}$ and $\boldsymbol{h}$ are the state transition function and the measurement function, $\boldsymbol{x}$ and $\boldsymbol{y}$ are the state and measurement vectors, $\boldsymbol{w}$ and $\boldsymbol{v}$ are the Gaussian white process and measurement noises. The process and measurement Gaussian white noises $\boldsymbol{w}$ and $\boldsymbol{v}$ are characterized by a null mean with diagonal covariance matrices $\boldsymbol{Q}$ and $\boldsymbol{R}$, respectively [29].

The state space equation in discrete form is formulated integrating the system equation (Equation (3.3)) from time t_k to time t_{k+1}, and can be written as follows:

$$
\boldsymbol{x}_{k+1} = \begin{bmatrix}
x_{1,k} + \frac{\Delta t}{m_{bd}}(k_{dy}\, x_{4,k} - k_{dy}\, x_{2,k} - C_{dy}\, x_{1,k} + C_{dy}\, x_{3,k}) \\
x_{2,k} + x_{1,k}\,\Delta t \\
x_{3,k} + \frac{\Delta t}{m_b}(k_y\, x_{8,k} + k_y\, x_{10,k} - 2k_y\, x_{4,k} - k_{dy}\, x_{4,k} + k_{dy}\, x_{2,k} + C_y\, x_{7,k} + C_y\, x_{9,k} - 2C_y\, x_{3,k} - C_{dy}\, x_{3,k} + C_{dy}\, x_{1,k}) \\
x_{4,k} + x_{3,k}\,\Delta t \\
x_{5,k} + \frac{\Delta t}{I_b}(a\, k_y\, x_{8,k} + k_x\, b^2\, x_{12,k} - a\, k_y\, x_{10,k} + k_x\, b^2\, x_{14,k} + a\, C_y\, x_{7,k} - a\, C_y\, x_{9,k} + C_x\, b^2\, x_{11,k} + \\
C_x\, b^2\, x_{13,k} - K_{axd}\, {l_{wb1}}^2\, x_{6,k} - x_{23,k}\, {l_{wb}}^2\, x_{5,k} - 2k_x\, b^2\, x_{6,k} - 2k_y\, a^2\, x_{6,k} - 2C_x\, b^2\, x_{5,k} - 2C_y\, a^2\, x_{5,k}) \\
x_{6,k} + x_{5,k}\,\Delta t \\
x_{7,k} + \frac{\Delta t}{m_{w1}}(x_{16,k} - k_y\, x_{8,k} + k_y\, x_{4,k} + a\, k_y\, x_{6,k} - C_y\, x_{7,k} + C_y\, x_{3,k} + a\, C_y\, x_{5,k}) \\
x_{8,k} + x_{7,k}\,\Delta t \\
x_{9,k} + \frac{\Delta t}{m_{w2}}(x_{18,k} - k_y\, x_{10,k} + k_y\, x_{4,k} + a\, k_y\, x_{6,k} - C_y\, x_{9,k} + C_y\, x_{3,k} + a\, C_y\, x_{5,k}) \\
x_{10,k} + x_{9,k}\,\Delta t \\
x_{11,k} + \frac{\Delta t}{I_{w1}}(x_{20,k} - k_x\, b^2\, x_{12,k} + k_x\, b^2\, x_{6,k} - C_x\, b^2\, x_{11,k} + C_x\, b^2\, x_{5,k}) \\
x_{12,k} + x_{11,k}\,\Delta t \\
x_{13,k} + \frac{\Delta t}{I_{w2}}(x_{22,k} - k_x\, b^2\, x_{14,k} + k_x\, b^2\, x_{6,k} - C_x\, b^2\, x_{13,k} + C_x\, b^2\, x_{5,k}) \\
x_{15,k} \\
x_{16,k} + x_{15,k}\,\Delta t \\
x_{17,k} \\
x_{18,k} + x_{17,k}\,\Delta t \\
x_{19,k} \\
x_{20,k} + x_{19,k}\,\Delta t \\
x_{21,k} \\
x_{22,k} + x_{21,k}\,\Delta t \\
x_{23,k}
\end{bmatrix} + \boldsymbol{w}_k \qquad (3.8)
$$

where a process noise $\boldsymbol{w}$ has been added, and Δt is the sampling time. The measurement vector $\boldsymbol{y}_{k+1}$ for the first configuration of sensors can be written as follows:

$$
\boldsymbol{y}_{k+1} = \begin{bmatrix}
\frac{1}{m_{bd}}(k_{dy}\, x_{4,k+1} - k_{dy}\, x_{2,k+1} - C_{dy}\, x_{1,k+1} + C_{dy}\, x_{3,k+1}) \\
\frac{1}{m_b}(k_y\, x_{8,k+1} + k_y\, x_{10,k+1} - 2k_y\, x_{4,k+1} - k_{dy}\, x_{4,k+1} + k_{dy}\, x_{2,k+1} \\
+C_y\, x_{7,k+1} + C_y\, x_{9,k+1} - 2C_y\, x_{3,k+1} - C_{dy}\, x_{3,k+1} + C_{dy}\, x_{1,k+1}) \\
\frac{1}{m_{w1}}(x_{16,k+1} - k_y\, x_{8,k+1} + k_y\, x_{4,k+1} + a\, k_y\, x_{6,k+1} - C_y\, x_{7,k+1} + C_y\, x_{3,k+1} + a\, C_y\, x_{5,k+1}) \\
\frac{1}{m_{w2}}(x_{18,k+1} - k_y\, x_{10,k+1} + k_y\, x_{4,k+1} + a\, k_y\, x_{6,k+1} - C_y\, x_{9,k+1} + C_y\, x_{3,k+1} + a\, C_y\, x_{5,k+1}) \\
x_{5,k+1}
\end{bmatrix} + \boldsymbol{v}_{k+1} \qquad (3.9)
$$

and for the second configuration of sensors:

$$
\boldsymbol{y}_{k+1} = \begin{bmatrix}
\frac{1}{m_{bd}}(k_{dy}\, x_{4,k+1} - k_{dy}\, x_{2,k+1} - C_{dy}\, x_{1,k+1} + C_{dy}\, x_{3,k+1}) \\
\frac{1}{m_b}(k_y\, x_{8,k+1} + k_y\, x_{10,k+1} - 2k_y\, x_{4,k+1} - k_{dy}\, x_{4,k+1} + k_{dy}\, x_{2,k+1} \\
+C_y\, x_{7,k+1} + C_y\, x_{9,k+1} - 2C_y\, x_{3,k+1} - C_{dy}\, x_{3,k+1} + C_{dy}\, x_{1,k+1}) \\
x_{5,k+1}
\end{bmatrix} + \boldsymbol{v}_{k+1} \qquad (3.10)
$$

where a measurement noise $\boldsymbol{v}$ has been added.

The developed estimator design model represented by Equation (3.8) can be extended for estimating both anti-yaw damping C_{axd} and stiffness K_{axd}.

Therefore, the anti-yaw stiffness is estimated through a parametric estimation approach, including it in the state vector of the estimator design model.

The discrete-time form of the estimator design model, functional for the entire CUKF algorithm implementation, is presented as follows:

$$
\boldsymbol{x}_{k+1} = \begin{bmatrix}
x_{1,k} + \frac{\Delta t}{m_{bd}}(k_{dy}\,x_{4,k} - k_{dy}\,x_{2,k} - C_{dy}\,x_{1,k} + C_{dy}\,x_{3,k}) \\
x_{2,k} + x_{1,k}\,\Delta t \\
x_{3,k} + \frac{\Delta t}{m_b}(k_y\,x_{8,k} + k_y\,x_{10,k} - 2k_y\,x_{4,k} - k_{dy}\,x_{4,k} + k_{dy}\,x_{2,k} + \\
C_y\,x_{7,k} + C_y\,x_{9,k} - 2C_y\,x_{3,k} - C_{dy}\,x_{3,k} + C_{dy}\,x_{1,k}) \\
x_{4,k} + x_{3,k}\,\Delta t \\
x_{5,k} + \frac{\Delta t}{I_b}(a\,k_y\,x_{8,k} + k_x\,b^2\,x_{12,k} - a\,k_y\,x_{10,k} + k_x\,b^2\,x_{14,k} + \\
a\,C_y\,x_{7,k} - a\,C_y\,x_{9,k} + C_x\,b^2\,x_{11,k} + C_x\,b^2\,x_{13,k} + \\
-x_{24,k}\,{l_{wb1}}^2\,x_{6,k} - x_{23,k}\,{l_{wb}}^2\,x_{5,k} - 2k_x\,b^2\,x_{6,k} + \\
-2k_y\,a^2\,x_{6,k} - 2C_x\,b^2\,x_{5,k} - 2C_y\,a^2\,x_{5,k}) \\
x_{6,k} + x_{5,k}\,\Delta t \\
x_{7,k} + \frac{\Delta t}{m_{w1}}(x_{16,k} - k_y\,x_{8,k} + k_y\,x_{4,k} + a\,k_y\,x_{6,k} - C_y\,x_{7,k} + \\
C_y\,x_{3,k} + a\,C_y\,x_{5,k}) \\
x_{8,k} + x_{7,k}\,\Delta t \\
x_{9,k} + \frac{\Delta t}{m_{w2}}(x_{18,k} - k_y\,x_{10,k} + k_y\,x_{4,k} + a\,k_y\,x_{6,k} - C_y\,x_{9,k} + \\
C_y\,x_{3,k} + a\,C_y\,x_{5,k}) \\
x_{10,k} + x_{9,k}\,\Delta t \\
x_{11,k} + \frac{\Delta t}{I_{w1}}\left(x_{20,k} - k_x\,b^2\,x_{12,k} + k_x\,b^2\,x_{6,k} - C_x\,b^2\,x_{11,k} + C_x\,b^2\,x_{5,k}\right) \\
x_{12,k} + x_{11,k}\,\Delta t \\
x_{13,k} + \frac{\Delta t}{I_{w2}}\left(x_{22,k} - k_x\,b^2\,x_{14,k} + k_x\,b^2\,x_{6,k} - C_x\,b^2\,x_{13,k} + C_x\,b^2\,x_{5,k}\right) \\
x_{15,k} \\
x_{16,k} + x_{15,k}\,\Delta t \\
x_{17,k} \\
x_{18,k} + x_{17,k}\,\Delta t \\
x_{19,k} \\
x_{20,k} + x_{19,k}\,\Delta t \\
x_{21,k} \\
x_{22,k} + x_{21,k}\,\Delta t \\
x_{23,k} \\
x_{24,k}
\end{bmatrix} + \boldsymbol{w}_k \tag{3.11}
$$

where an additive process noise $\boldsymbol{w}$ is considered. The presented estimator design model has been obtained by introducing the anti-yaw stiffness in the estimation process. Therefore, the augmented state vector related to the estimator design model becomes:

$$\boldsymbol{x} = \begin{bmatrix} \dot{y}_{bd}, y_{bd}, \dot{y}_b, y_b, \dot{\psi}_b, \psi_b, \dot{y}_{w1}, y_{w1}, \dot{y}_{w2}, y_{w2}, \dot{\psi}_{w1}, \psi_{w1}, \dot{\psi}_{w2}, \psi_{w2}, \\ F_{yw1d}, F_{yw1}, F_{yw2d}, F_{yw2}, M_{w1d}, M_{w1}, M_{w2d}, M_{w2}, C_{axd}, K_{axd} \end{bmatrix}^T \tag{3.12}$$

where the renamed state variables result:

$$\boldsymbol{x} = [x_1, \dots, x_{24}]^T \tag{3.13}$$

Considering the set of measurements described by Equation (3.9), the CUKF for monitoring the anti-yaw suspension components by estimating both damping C_{axd}, and stiffness K_{axd} is designed by coupling Equations (3.9) and (3.11).

In Figure 3.3 the estimation procedure is summarized. The input variables for railway vehicle model developed in SIMPACK and the measurements obtained through the latter functional to improve the estimation provided by the CUKF are pointed out.

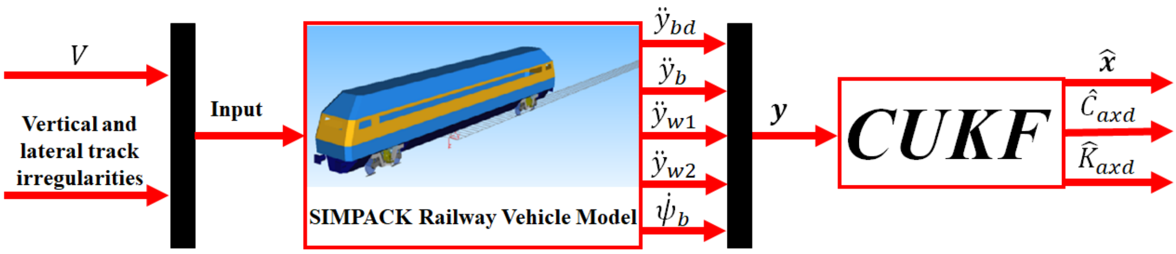

Figure 3.3. Estimation flow for monitoring the anti-yaw suspension components through CUKF with five measurements.

3.2. Estimator design models for sideslip angle estimation and monitoring of tire-road interaction

3.2.1. Estimator design model for the estimation of vehicle sideslip angle and lateral friction coefficients

The aim of the proposed model-based estimator, based on an Extended Kalman Filter (EKF), is the coupled estimation of vehicle sideslip angle and lateral friction coefficients of a road vehicle for tire-road interaction monitoring.
The estimator design model is based on the Double-track vehicle model [120].
The Double-track vehicle model is schematized in Figures 3.4a and 3.4b.
The first subscript (i) indicates the axle (front/rear), while the second subscript (j) indicates the position (left/right) of wheels.

δ is the steering wheel angle; r is the yaw rate; $\boldsymbol{V}_G$ is the centre of gravity (COG) velocity vector. v_y and v_x are, respectively, the COG vehicle velocity components in lateral and longitudinal directions.

$\dot{v}_y$ and $\dot{r}$ represent the first-time derivatives of v_y and r.
The slip angles α_{ij} of front left, front right, rear left and rear right tires are defined as follows:

$$
\begin{aligned}
\alpha_{11} &= \delta - \operatorname{atan}\left(\frac{v_y + r\,a}{v_x - r\,\frac{tw}{2}}\right)\\
\alpha_{12} &= \delta - \operatorname{atan}\left(\frac{v_y + r\,a}{v_x + r\,\frac{tw}{2}}\right)\\
\alpha_{21} &= -\operatorname{atan}\left(\frac{v_y - r\,b}{v_x - r\,\frac{tw}{2}}\right)\\
\alpha_{22} &= -\operatorname{atan}\left(\frac{v_y - r\,b}{v_x + r\,\frac{tw}{2}}\right)
\end{aligned}
\tag{3.14}
$$

The sideslip angle β is defined as follows:

$$
\beta = \operatorname{atan}\left(\frac{v_y}{v_x}\right) \tag{3.15}
$$

F_{xij} and F_{yij} are the longitudinal and lateral tire-road interaction forces.

The other parameters of the Double-track vehicle model extracted by a complete and detailed Multibody vehicle model developed in ADAMS Car [121] are listed in Table 3.3.

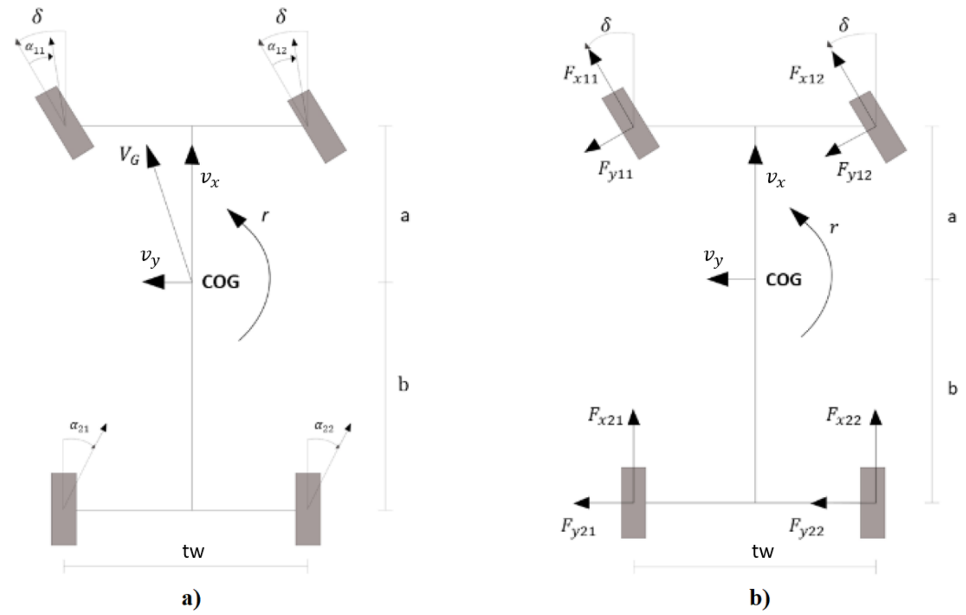

Figure 3.4. a) The Double-track model: velocity vectors, slip angles and steering wheels angles; b) The Double-track model: velocity vectors and pneumatic-road tangential interaction forces.

Table 3.3. List of vehicle main physical parameters.

Parameter name	***Value***
Vehicle mass (m)	2217 kg
Distance from COG to front wheels (a)	1.397 m
Distance from COG to rear wheels (b)	1.263 m
Height of COG (h)	0.65 m
Yaw moment of inertia (J)	3231 kg m^2
Track width (tw)	1.492 m

By neglecting the longitudinal dynamic, the lateral and yaw dynamics of the double-track model are described by the following equations:

$$\begin{cases} \dot{v}_y = \dfrac{1}{m}\left(F_{y11}\cos\delta + F_{y12}\cos\delta + F_{y21} + F_{y22}\right) - v_x\, r \\ \dot{r} = \dfrac{1}{J}\left(a\, F_{y11}\cos\delta + a\, F_{y12}\cos\delta - F_{y21}\, b - F_{y22}\, b + \dfrac{tw}{2}\, F_{y11}\sin\delta - \dfrac{tw}{2}\, F_{y12}\sin\delta\right) \end{cases} \tag{3.16}$$

A four-parameter version of the Pacejka Magic Formula [57] (stiffness factor $B = 11.56$, form factor $C = 1.359$, peak value D, curvature factor $E = -0.08696$) is used for modelling the tire/road interaction forces to complete the description of the mechanical model related to the vehicle:

$$F_y(\alpha) = D\sin\{C\,\mathrm{atan}[B\,\alpha - E(B\,\alpha - \mathrm{atan}(B\,\alpha))]\} \tag{3.17}$$

The parameter D is placed as the product between the vertical load F_z acting on a wheel and the lateral friction coefficient μ [57]:

$$D = \mu\, F_z \tag{3.18}$$

For each wheel of each axle, the parameter D_{ij} is defined as follows:

$$\begin{matrix} D_{i1} = \mu_l\, F_{zi1} \\ D_{i2} = \mu_r\, F_{zi2} \end{matrix} \qquad \mathit{for}\ i = 1{,}2 \tag{3.19}$$

where μ_l and μ_r are the lateral tire-road friction coefficients referred to the left and right sides of the vehicle, respectively. Therefore, the parameters D_{ij} referred to the Pacejka Magic Formula described by Equation (3.17) are:

$$\begin{matrix} D_{11} = \mu_l\, F_{z11} \\ D_{21} = \mu_l\, F_{z21} \\ D_{12} = \mu_r\, F_{z12} \\ D_{22} = \mu_r\, F_{z22} \end{matrix} \tag{3.20}$$

The vertical loads acting on each wheel affected by lateral load transfers [120] are defined as follows (Figure 3.5):

$$
\begin{aligned}
F_{z11} &= \frac{m\,b}{2(a+b)}\,g - \frac{m\,h}{2(a+b)}\,a_x - \frac{m\,a_y\,(a+b)}{2tw}\frac{b}{(a+b)}\left(\frac{d_1}{(a+b)} + \frac{K_{\varphi 1}\,(h-d)}{K_\varphi\,\left((a+b)-a\right)}\right)\\
F_{z21} &= \frac{m\,a}{2(a+b)}\,g + \frac{m\,h}{2(a+b)}\,a_x - \frac{m\,a_y\,(a+b)}{2tw}\frac{a}{(a+b)}\left(\frac{d_2}{(a+b)} + \frac{K_{\varphi 2}\,(h-d)}{K_\varphi\,((a+b)-b)}\right)\\
F_{z12} &= \frac{m\,b}{2(a+b)}\,g - \frac{m\,h}{2(a+b)}\,a_x + \frac{m\,a_y\,(a+b)}{2tw}\frac{b}{(a+b)}\left(\frac{d_1}{(a+b)} + \frac{K_{\varphi 1}\,(h-d)}{K_\varphi\,((a+b)-a)}\right)\\
F_{z22} &= \frac{m\,a}{2(a+b)}\,g + \frac{m\,h}{2(a+b)}\,a_x + \frac{m\,a_y\,(a+b)}{2tw}\frac{a}{(a+b)}\left(\frac{d_2}{(a+b)} + \frac{K_{\varphi 2}\,(h-d)}{K_\varphi\,((a+b)-b)}\right)
\end{aligned}
\tag{3.21}
$$

where:

- $K_{\varphi 1} = K_{\varphi 2} = 0.5$ Nm/rad are, respectively, front and rear axles roll stiffness;
- $K_{phi} = 1$ Nm/rad is the roll stiffness;
- $d_1 = d_2 = 0.325$ m are heights of the front axle and rear axle roll centre;
- $d = 0.325$ m is the height of the roll centre;
- a_x is the longitudinal acceleration, and $g = 9.806$ m/s^2 is the gravity acceleration.

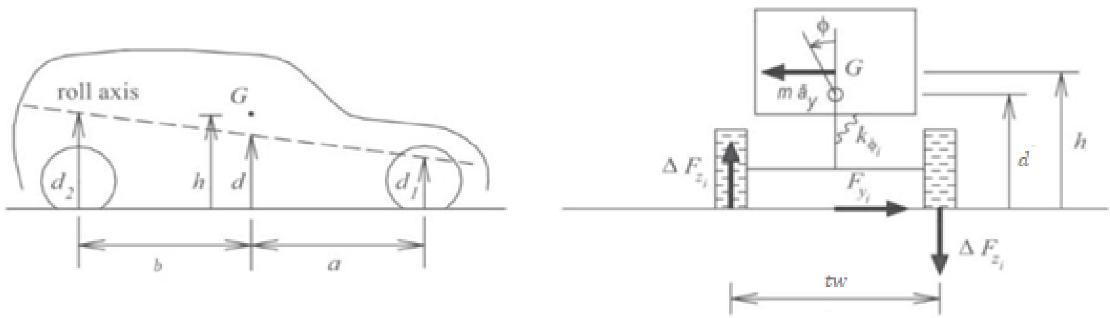

Figure 3.5. Schematization of the lateral load transfer: equilibrium conditions about the roll axis.

Therefore, the lateral tire-road forces are computed as follows based on the Pacejka Magic Formula (Equation (3.17)):

$$
\begin{aligned}
F_{y_{11}}(\alpha_{11}) &= D_{11}\sin\{C\,\mathrm{atan}[B\,\alpha_{11} - E(B\,\alpha_{11} - \mathrm{atan}(B\,\alpha_{11}))]\}\\
F_{y_{21}}(\alpha_{21}) &= D_{21}\sin\{C\,\mathrm{atan}[B\,\alpha_{21} - E(B\,\alpha_{21} - \mathrm{atan}(B\,\alpha_{21}))]\}\\
F_{y_{12}}(\alpha_{12}) &= D_{12}\sin\{C\,\mathrm{atan}[B\,\alpha_{12} - E(B\,\alpha_{12} - \mathrm{atan}(B\,\alpha_{12}))]\}\\
F_{y_{22}}(\alpha_{22}) &= D_{22}\sin\{C\,\mathrm{atan}[B\,\alpha_{22} - E(B\,\alpha_{22} - \mathrm{atan}(B\,\alpha_{22}))]\}
\end{aligned}
\tag{3.22}
$$

where B, C and E have been identified through offline tests.

The estimation of lateral tire-road friction coefficients μ_l and μ_r is made by employing a parametric estimation strategy, including them in an augmented state vector [29].
Considering the following Equation for estimating lateral tire-road friction coefficients:

$$\dot{\mu}_l = 0;\ \dot{\mu}_r = 0 \tag{3.23}$$

the complete estimator design model in the continuous-time form is obtained by coupling Equations (3.16) and (3.23):

$$\begin{cases} \dot{v}_y = \dfrac{1}{m}\left(F_{y11}\cos\delta + F_{y12}\cos\delta + F_{y21} + F_{y22}\right) - v_x\, r \\ \dot{r} = \dfrac{1}{J}\left(a\, F_{y11}\cos\delta + a\, F_{y12}\cos\delta - F_{y21}\, b - F_{y22}\, b + \dfrac{tw}{2}\, F_{y11}\sin\delta - \dfrac{tw}{2}\, F_{y12}\sin\delta\right) \\ \dot{\mu}_l = 0 \\ \dot{\mu}_r = 0 \end{cases} \tag{3.24}$$

Therefore, the state vector is given by:

$$\boldsymbol{x} = \left[v_y, r, \mu_l, \mu_r\right]^T = [x_1, x_2, x_3, x_4]^T \tag{3.25}$$

The EKF is designed around Equation (3.24) and considering a set of measurements constituted by the lateral acceleration a_y and the yaw rate r:

$$\boldsymbol{y} = \left[a_y, r\right]^T = \left[\dot{v}_y + v_x r, r\right]^T \tag{3.26}$$

The employment of measurements provided by sensors allows making the correction step of the EKF, producing corrected estimations of predicted state variables through the estimator design model.
The input vector $\boldsymbol{u} = [\delta, v_x]^T$ composed by the steering angle δ and the longitudinal speed v_x.
The discrete time form of the estimator design model is described by the following equations:

$$\begin{gathered} \boldsymbol{x}_{k+1} = \boldsymbol{f}(\boldsymbol{x}_k) + \boldsymbol{w}_k \\ \boldsymbol{y}_{k+1} = \boldsymbol{h}(\boldsymbol{x}_{k+1}) + \boldsymbol{v}_{k+1} \end{gathered} \tag{3.27}$$

where $\boldsymbol{f}$ and $\boldsymbol{h}$ are the state transition function and the measurement function, $\boldsymbol{x}$ and $\boldsymbol{y}$ are the state and measurement vectors, $\boldsymbol{w}$ and $\boldsymbol{v}$ are the Gaussian white process and measurement noises. The process and measurement Gaussian white noises $\boldsymbol{w}$ and $\boldsymbol{v}$ are characterized by a null mean with diagonal covariance matrices $\boldsymbol{Q}$ and $\boldsymbol{R}$, respectively [29].

The state space equation in discrete form is formulated integrating Equation (3.24) from time t_k to time t_{k+1}, and can be written as follows:

$$\boldsymbol{x}_{k+1} = \begin{bmatrix} x_{1,k} + \frac{\Delta t}{m}\left(F_{y11,k}\cos\delta_{,k} + F_{y12,k}\cos\delta_{,k} + F_{y21,k} + F_{y22,k}\right) - \Delta t\, v_x\, x_{2,k} \\ x_{2,k} + \frac{\Delta t}{J}\left(a\, F_{y11,k}\cos\delta_{,k} + a\, F_{y12,k}\cos\delta_{,k} - F_{y21,k}\, b - F_{y22,k}\, b + \frac{tw}{2}\, F_{y11,k}\sin\delta_{,k} - \frac{tw}{2}\, F_{y12,k}\sin\delta_{,k}\right) \\ x_{3,k} \\ x_{4,k} \end{bmatrix} + \boldsymbol{w}_k \tag{3.28}$$

where a process noise $\boldsymbol{w}$ has been added, and Δt is the sampling time.

The measurement vector $\boldsymbol{y}_{k+1}$ can be written as follows:

$$\boldsymbol{y}_{k+1} = \begin{bmatrix} \frac{1}{m}\left(F_{y11,k}\cos\delta_{,k} + F_{y12,k}\cos\delta_{,k} + F_{y21,k} + F_{y22,k}\right) \\ x_{2,k+1} \end{bmatrix} + \boldsymbol{v}_{k+1} \tag{3.29}$$

where a measurement noise $\boldsymbol{v}$ has been added.

The discrete-time form of the estimator design model makes suitable the implementation of the EKF in electronic control units and other types of digital systems. In Figure 3.6, a conceptual scheme of the estimation procedure is shown, pointing out the input variables for both the EKF and vehicle model developed in ADAMS Car and the measurements obtained through the latter functional to improve the estimation provided by the EKF.

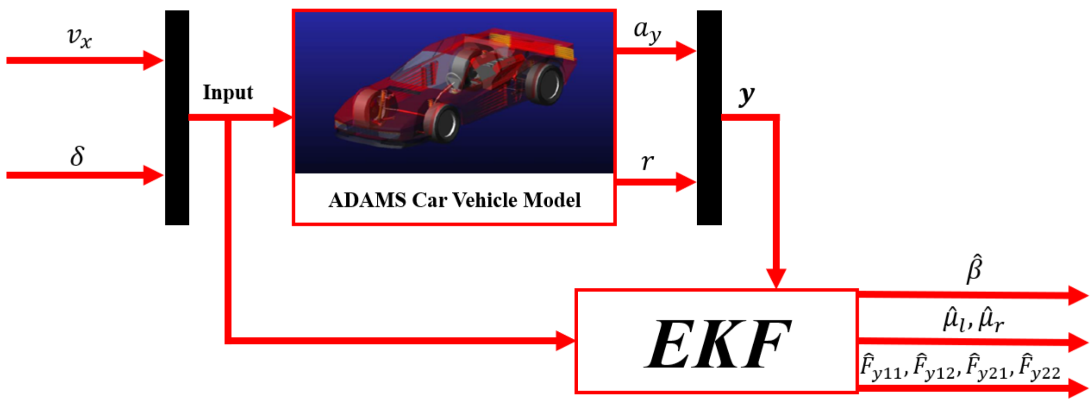

Figure 3.6. Estimation flow for monitoring tire-road interaction conditions and vehicle performances by estimating the sideslip angle through EKF.

3.2.2. Estimator design model for vehicle and tire-road monitoring with no interaction modelling

The estimator design model proposed in Section 3.2.1 allows the Extended Kalman Filter, chosen as a model-based estimator for monitoring purposes, to estimate the sideslip angle, fundamental for monitoring vehicle performances and for providing feedback signals to control units and lateral tire-road friction coefficients of both the sides of the vehicle for tire-road interaction monitoring.

Unfortunately, the calibration of tire models, such as the chosen Pacejka one with four parameters [57], requires expensive experimental tests and offline optimization procedures for identifying the parameters of the tire model.

Therefore, an estimator design model, suitable for the design of an Extended Kalman Filter (EKF), is presented for estimating the sideslip angle and the lateral tire-road forces without specific modelling of tires for overcoming the previously described issue related to the calibration of tire models.

Furthermore, the lateral tire-road friction coefficient is included in the estimation procedure for tire-road condition monitoring purposes.

The developed estimator design model is based on a single-track vehicle model to capture the lateral and yaw dynamics.

The single-track model is represented in Figure 3.7. The reference frames Oxy and Gxy are the inertial and fixed ones, respectively. The velocity **v** of the centre of gravity (COG) is decomposed in the lateral velocity v_y and the longitudinal one v_x.

The longitudinal dynamic is neglected, assuming a constant v_x [37].

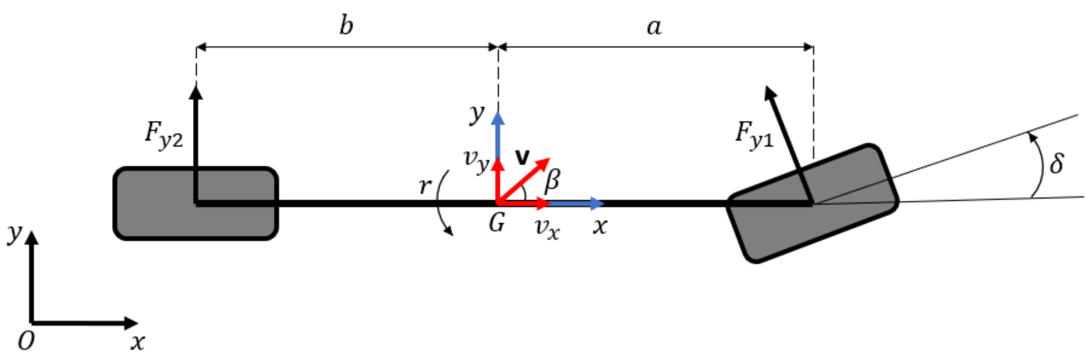

Figure 3.7. Single-track vehicle model.

The yaw rate r is computed in the reference frame Oxy.
Furthermore, δ is the steering angle while F_{y1} and F_{y2} are the lateral tire-road forces of the front and rear axle, respectively.
The parameters referred to the single-track model extracted by a complete and detailed Multibody vehicle model developed in ADAMS Car [121] are shown in Table 3.4.

Table 3.4. Parameters of the estimator design model.

Parameter name	***Value***
Vehicle mass (M)	2217 kg
Yaw moment of inertia (J)	3231 kg m^2
Distance from COG to front wheels (a)	1.397 m
Distance from COG to rear wheels (b)	1.263 m

The lateral and yaw dynamics of the single-track model are described in the continuous-time form by the following equations:

$$\begin{cases} \dot{v}_y = \dfrac{1}{M}\left(F_{y1}\cos\left(\delta\right) + F_{y2}\right) - v_x\, r \\ \dot{r} = \dfrac{1}{J}\left(a\, F_{y1}\cos(\delta) - F_{y2}\, b\right) \end{cases} \tag{3.30}$$

where $\dot{v}_y$ and $\dot{r}$ are the first-time derivatives of v_y and r, respectively.
Referring to Figure 3.7, the sideslip angle β can be determined as follows:

$$\beta = \text{atan}\left(\frac{v_y}{v_x}\right) \tag{3.31}$$

Therefore, the state vector of the single-track vehicle model is defined as follows:

$$\boldsymbol{x} = \left[v_y, r\right]^T \tag{3.32}$$

For including the lateral tire-road friction coefficient μ and two variables K_1 and K_2, functional for the estimation of lateral tire-road forces, in the state vector of the estimator design model, the augmented state technique coupled with a parametric estimation strategy has been adopted [29].

Equations representing the lateral tire-road forces, functional for their estimation, have been developed to avoid a specific tire model employment.

Based on this purpose, consider a simplified Pacejka Magic Formula [57] for the lateral tire-road forces F_y computing:

$$\begin{cases} F_y(\alpha) = D \sin\{C \ \mathrm{atan}[B\ \alpha - E(B\ \alpha - \mathrm{atan}(B\ \alpha)]\} \\ D = \mu\ F_z \end{cases} \tag{3.33}$$

where F_z is the vertical load acting on the front or rear axle, α is the drift angle referred to each wheel and with B, C and E, the typical Pacejka parameters are indicated.

The parameters B, C and E are, typically, identified through expensive experimental tests. Therefore, referring to Figure 3.7, the following expressions of the lateral forces F_{y1} and F_{y2} allow their estimation avoiding the identification of the previously mentioned Pacejka parameters and other types of tire modelling techniques:

$$\begin{gathered} F_{y1} = \mu\ F_{z1}\ K_1 \\ F_{y2} = \mu\ F_{z2}\ K_2 \end{gathered} \tag{3.34}$$

where $F_{z1} = M\ g\ b/(a+b)$ and $F_{z2} = M\ g\ a/(a+b)$ are the static vertical loads acting on the front axle and the rear one (lateral load transfers are not taken into account in the single-track vehicle model), respectively ($g = 9.806$ m/s^2 is the gravity acceleration).

The state variables μ, K_1 and K_2 are estimated through a parametric estimation approach [29] through the following formulation:

$$\begin{gathered} \dot{\mu} = 0 \\ \dot{K}_1 = 0;\ \dot{K}_2 = 0 \end{gathered} \tag{3.35}$$

Therefore, by considering the augmented state vector $\boldsymbol{x} = \left[v_y, r, \mu, K_1, K_2\right]^T$, the complete estimator design model is given by:

$$\begin{cases} \dot{v}_y = \dfrac{1}{M}\left(F_{y1}\cos(\delta) + F_{y2}\right) - v_x\, r \\ \dot{r} = \dfrac{1}{J}\left(a\, F_{y1}\cos(\delta) - F_{y2}\, b\right) \\ \dot{\mu} = 0 \\ \dot{K}_1 = 0 \\ \dot{K}_2 = 0 \end{cases} \tag{3.36}$$

The input variables for the estimator design model and, therefore, for the EKF are the steering angle δ and the longitudinal velocity v_x.

Considering the global lateral acceleration a_y and the yaw rate r as measurements collected in the measurement vector defined as follows:

$$\boldsymbol{y} = \left[a_y, r\right]^T = \begin{bmatrix} \dfrac{1}{M}\left(F_{y1}\cos(\delta) + F_{y2}\right) \\ r \end{bmatrix} \tag{3.37}$$

and taking into account Equation (3.36), the EKF is able to perform its prediction-correction algorithm for purposes of sideslip angle estimation and tire-road condition monitoring.

The estimator design model described in Equation (3.36) can be written in discrete-time form, assuming a fixed sampling time Δt, making it functional for the implementation in the EKF estimation algorithm.

The discrete-time form of the estimator design model is described by the following equations:

$$\begin{aligned} \boldsymbol{x}_{k+1} &= \boldsymbol{f}(\boldsymbol{x}_k) + \boldsymbol{w}_k \\ \boldsymbol{y}_{k+1} &= \boldsymbol{h}(\boldsymbol{x}_{k+1}) + \boldsymbol{v}_{k+1} \end{aligned} \tag{3.38}$$

where $\boldsymbol{f}$ and $\boldsymbol{h}$ are the state transition function and the measurement function, $\boldsymbol{x}$ and $\boldsymbol{y}$ are the state and measurement vectors, $\boldsymbol{w}$ and $\boldsymbol{v}$ are the Gaussian white process and measurement noises. The process and measurement Gaussian white noises $\boldsymbol{w}$ and $\boldsymbol{v}$ are characterized by a null mean with diagonal covariance matrices $\boldsymbol{Q}$ and $\boldsymbol{R}$, respectively [29].

By renaming state variables of the augmented state vector $\boldsymbol{x} = \left[v_y, r, \mu, K_1, K_2\right]^T = [x_1, x_2, x_3, x_4, x_5]^T$ the complete estimator design model in discrete form is formulated integrating Equation (3.36) from time t_k to time t_{k+1}, and can be written as follows:

$$\boldsymbol{x}_{k+1} = \begin{bmatrix} x_{1,k} + \dfrac{\Delta t}{M}\left(F_{y1,k}\cos\left(\delta_{,k}\right) + F_{y2,k}\right) - v_{x,k}\, x_{2,k}\, \Delta t \\ x_{2,k} + \dfrac{\Delta t}{J}\left(a\, F_{y1,k}\cos\left(\delta_{,k}\right) - F_{y2,k}\, b\right) \\ x_{3,k} \\ x_{4,k} \\ x_{5,k} \end{bmatrix} + \boldsymbol{w}_k \tag{3.39}$$

where a process noise $\boldsymbol{w}$ has been added.

The measurement vector $\boldsymbol{y}_{k+1}$ can be written as follows:

$$\boldsymbol{y}_{k+1} = \begin{bmatrix} \dfrac{1}{M}\left(F_{y1,k}\cos\left(\delta_{,k}\right) + F_{y2,k}\right) \\ x_{2,k+1} \end{bmatrix} + \boldsymbol{v}_{k+1} \tag{3.40}$$

where a measurement noise $\boldsymbol{v}$ has been added.

In Figure 3.8, a conceptual scheme of the estimation flow is shown, pointing out the input variables for both the EKF and vehicle model developed in ADAMS Car and the measurements obtained through the latter functional to improve the estimation provided by the EKF.

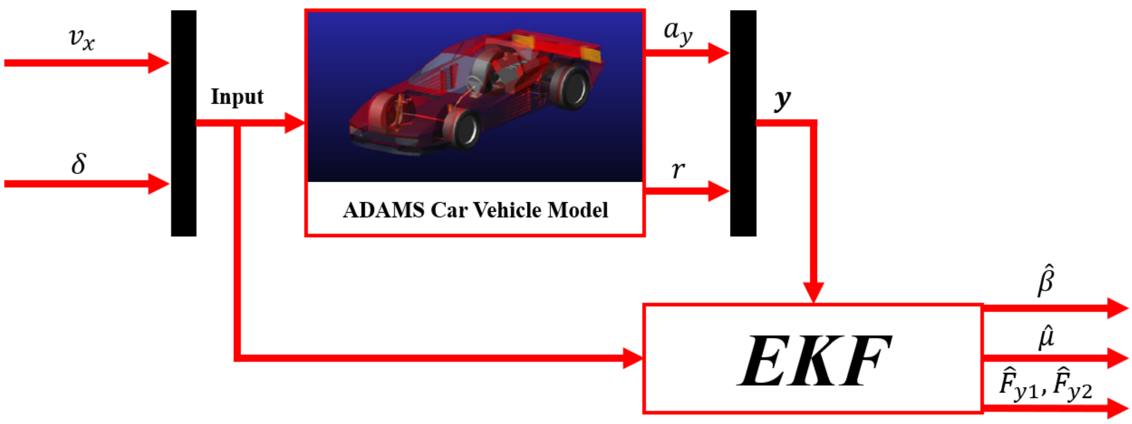

Figure 3.8. Estimation flow for monitoring tire-road interaction conditions with no interaction modelling and vehicle performances by estimating the sideslip angle through EKF.

3.3 Estimator design model for monitoring the surfaces of sliding seismic isolators

The difficulties in the characterization of frictional properties for health and wear condition monitoring of Curved Surfaces Sliding (CSS) seismic isolators led to the development of a model-based monitoring solution based on a Constrained Unscented Kalman Filter (CUKF). Some physical modelling considerations are functional for developing the estimator design model on which the CUKF is designed.

At the generic time instant t, the instantaneous values of the longitudinal (F_x) and transversal (F_y) components of the horizontal force resisted by a sliding isolator in a bi-directional motion in the x-y plane (see Figure 3.9) can be calculated as [64,122]:

$$\begin{bmatrix} F_x \\ F_y \end{bmatrix} = \frac{N}{R_{eff}} \begin{bmatrix} d_x \\ d_y \end{bmatrix} + \mu_{eff}\, N(t) \begin{bmatrix} \sin(\vartheta)\, \mathrm{sign}(\dot{d}_x) \\ \cos(\vartheta)\, \mathrm{sign}(\dot{d}_y) \end{bmatrix} \tag{3.41}$$

where:

a) N is the vertical load acting on the device;
b) $R_{eff} = R_1 + R_2 - h$, and $\mu_{eff} = (\mu_1 R_1 + \mu_2 R_2)/(R_1 + R_2)$ are the effective radius, and the effective friction coefficient, respectively;
c) d_x, and d_y are the longitudinal and transversal displacement components;
d) $\vartheta = \mathrm{atan}(|\Delta d_x / \Delta d_y|)$ is the trajectory angle (with $0 \leq \vartheta \leq \frac{\pi}{2}$); being Δd_x, and Δd_y the displacement increments from the previous time instant;
e) $\mathrm{sign}(\cdot)$ is the sign function;
f) the dot employed as accent denotes the time derivate, e.g., $\dot{d}_x$, and $\dot{d}_y$.

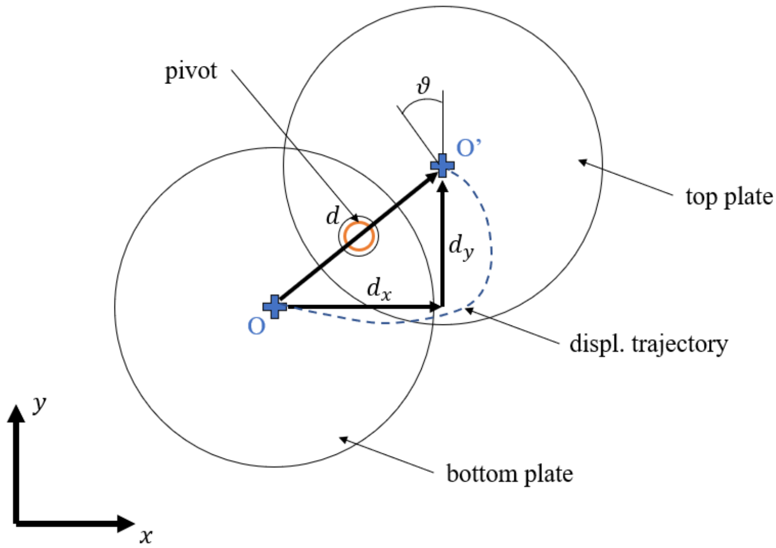

Figure 3.9. In-plane kinematic of a Curved Surfaces Sliding isolator.

Previous studies identified several sources of variability of the coefficient friction, such as the instantaneous sliding velocity, contact pressure, and temperature of the sliding surfaces [74,75], and a number of constitutive models [123,124], and numerical approaches [75] were developed to capture and reproduce this complex behaviour during the motion of sliding isolators.

Despite the suitability of the proposed formulations to simulate the lateral response of CSSs has been widely proven in the referred studies, the calibration of relevant parameters is a challenging task [123,124] since the coefficient of friction at both sliding surfaces can be expressed as:

$$\begin{cases} \mu_1(t) = \mu_1(v_1, p_1, T_1) \\ \mu_2(t) = \mu_2(v_2, p_2, T_2) \end{cases} \tag{3.42}$$

where v is the sliding velocity, p is the contact pressure, T is the temperature, and subfixes 1 and 2 refer to the primary and secondary sliding surfaces of the single CSS, or to the upper and the lower sliding surfaces of the DCSS, as relevant.

Since quantitative information about these dependencies strongly depend on the particular employed sliding material (e.g. PTFE, UHMWPE, in dry or lubricated condition), the tricky dependence of the coefficient of friction on these factors is “only” qualitatively represented in Figure 3.10.

However, as confirmed also by very recent experimental studies [125,126], an increase in sliding velocity causes the coefficient of friction to rapidly decrease from its breakaway value,

μ_B, to a minimum low-velocity value μ_{LV} (typically for sliding velocities $v < 1$ mm/s), and then to gradually increase until it reaches the (asymptotic) high-velocity value μ_{HV} (typically for sliding velocities $v > 100$ mm/s).

An increase in temperature, caused either from the heat generated during the sliding or from a change in environmental temperature, results in a decrease of the coefficient of friction (Figure 3.10-left).

An increase in contact pressure causes friction to decrease (Figure 3.10-right). As a result, during an experimental test the coefficient of friction shows a continuous variation over time from its initial value at the beginning of the sliding motion.

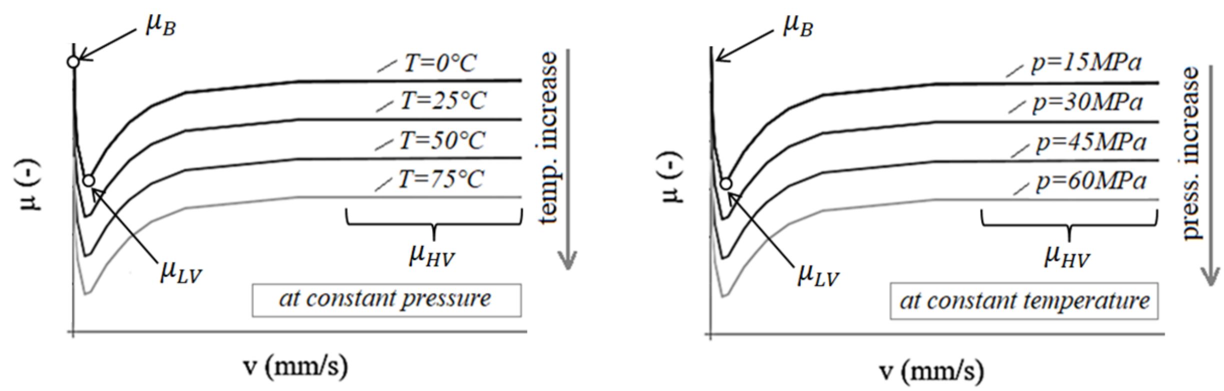

Figure 3.10. Qualitative representation of the dependence of the friction coefficient on the sliding velocity and its typical decrease for increasing temperatures (left), and contact pressures (right), adapted from [127].

Based on the previously described issues in the identification of frictional behaviour of CSS isolators, an estimator design model suitable for the CUKF design has been developed to identify the coefficient of friction and its time-dependent variation at the individual sliding surfaces of CCS and DCSS isolators.

This tool is applicable to data collected from the displacement-controlled tests performed during the prototype testing of the isolators as recommended by the codes and avoids to account for explicit formulations of the friction modeling of Equation (3.42) to extrapolate the frictional properties from the experimental data.

The in-plane displacement components d_x and d_y, the velocity components v_x and v_y, and the trajectory angle ϑ imposed during testing are collected in the input vector $\boldsymbol{u} = \left[d_x, d_y, v_x, v_y, \vartheta\right]^T$ and used as input for the CUKF estimator.

The avoidance of needing an *a priori* friction model is guaranteed by the employment of the random walk model (RWM) estimation technique [1,24,26,77] coupled with a parametric estimation approach [29].

The friction coefficients at the two sliding surfaces are time-variant during the isolator motion. The friction coefficients variation is due to different effects as the sliding velocity, the temperature variation and the vertical loads acting on the isolator.
Furthermore, on the two sliding surfaces, the friction coefficient can change in a different way, in particular, on the basis of the material and geometrical properties of the isolator.

For this reason, in the developed model, the time-variant friction coefficient at the i-th sliding surface (for $i = 1{,}2$) is formulated as: $\mu_i = \mu_{i,0}\, f_i$, where $\mu_{i,0}$ is the initial friction coefficient relatives to the isolator in static conditions at room temperature and f_i is the time-dependent variation function of the respective friction coefficient, bounded in [0,1]. Furthermore, the initial friction coefficients $\mu_{1,0}$ and $\mu_{2,0}$ are considered at room temperature. This approach allows capturing with a priori no knowledge the overall friction coefficients and their physical characteristics in a decoupled way on both the sliding surfaces of the isolator, providing information on the friction coefficients in both the static and dynamic conditions.
It is worth noting that the two time-dependent friction variation functions f_1 and f_2 are able to depict simultaneously the overall variation of the instantaneous friction coefficients at the two sliding surfaces due to the three aforementioned phenomena (dependency on sliding velocity, temperature and the vertical loads acting on the isolator).
The RWM structure is based on a stochastic model that includes the friction-variation function and its first-time derivative:

$$\begin{bmatrix} \dot{f}_{d1} \\ \dot{f}_1 \\ \dot{f}_{d2} \\ \dot{f}_2 \end{bmatrix} = \begin{bmatrix} 0 & 0 & 0 & 0 \\ 1 & 0 & 0 & 0 \\ 0 & 0 & 0 & 0 \\ 0 & 0 & 1 & 0 \end{bmatrix} \begin{bmatrix} f_{d1} \\ f_1 \\ f_{d2} \\ f_2 \end{bmatrix} + \boldsymbol{w}_f \tag{3.43}$$

where f_1 and f_2 represent the friction-variation functions of the primary and secondary sliding surfaces, respectively, f_{d1} and f_{d2} are their first-time derivatives, and $\boldsymbol{w}_f$ is a random white noise. $\dot{f}_{d1}$, $\dot{f}_{d2}$, $\dot{f}_1$ and $\dot{f}_2$ are the first-time derivatives of f_{d1}, f_{d2}, f_1 and f_2, respectively.

According to this formulation, at a given time instant t the coefficients of friction at the sliding surfaces $\mu_1 = \mu_{1,0}\, f_1$ and $\mu_2 = \mu_{2,0}\, f_2$ are expressed as the product of the relevant initial values $\mu_{1,0}$ and $\mu_{2,0}$ and the time-varying functions f_1 and f_2, respectively.

It is worth noting that assuming $0 \leq f_1 \leq 1$ and $0 \leq f_2 \leq 1$, f_1 and f_2 have their physical counterparts in the time-dependent friction variation functions postulated by several friction models like e.g. [123,124].

The identification of the initial friction coefficients $\mu_{1,0}$ and $\mu_{2,0}$ at the two sliding surfaces of the isolator is made through a parametric estimation strategy [29] that includes $\mu_{1,0}$ and $\mu_{2,0}$ in the state vector as system state variables.

Therefore, the complete observer design model in the continuous-time domain takes the form:

$$\begin{cases} \dot{f}_{d1} = 0 \\ \dot{f}_1 = f_{cd1} \\ \dot{f}_{d2} = 0 \\ \dot{f}_2 = f_{cd2} \\ \dot{\mu}_{1,0} = 0 \\ \dot{\mu}_{2,0} = 0 \end{cases} \tag{3.44}$$

and the state vector is composed by:

$$\boldsymbol{x} = \left[f_{d1}, f_1, f_{d2}, f_2, \mu_{1,0}, \mu_{2,0}\right]^T = \left[x_{1,k}, x_{2,k}, x_{3,k}, x_{4,k}, x_{5,k}, x_{6,k}\right]^T \tag{3.45}$$

The state space equation in discrete-time form is formulated by integrating the system equation (3.44) from time t_k to time t_{k+1}, and can be written as:

$$\boldsymbol{x}_{k+1} = \boldsymbol{f}(\boldsymbol{x}_k) + \boldsymbol{w}_k = \begin{bmatrix} x_{1,k} \\ x_{2,k} + x_{1,k}\,\Delta t \\ x_{3,k} \\ x_{4,k} + x_{3,k}\,\Delta t \\ x_{5,k} \\ x_{6,k} \end{bmatrix} + \boldsymbol{w}_k \tag{3.46}$$

where $\boldsymbol{f}(\boldsymbol{x})$ is the state transition function, $\boldsymbol{w}$ is the additive Gaussian process noise and Δt is the sampling time.

The typical outputs of bi-directional displacement-controlled tests of CSS isolators are the reaction forces F_x and F_y along the x and y axes.

The reaction forces contain physical information on the initial value of the coefficient of friction and the relevant variation during the motion, and therefore are employed as measurements to feed the CUKF.

Following this reasoning, the measurement vector is defined as:

$$\boldsymbol{y} = \left[F_x, F_y\right]^T \tag{3.47}$$

The measurement equations in the discrete-time domain can be written as follows:

$$\boldsymbol{y}_{k+1} = \boldsymbol{h}(\boldsymbol{x}_k, \boldsymbol{u}_k) + \boldsymbol{v}_{k+1} = \begin{bmatrix} F_{rx,k} + F_{fricx,k} \\ F_{ry,k} + F_{fricy,k} \end{bmatrix} + \boldsymbol{v}_{k+1} \tag{3.48}$$

where $\boldsymbol{h}(\boldsymbol{x}, \boldsymbol{u})$ is the measurement function and $\boldsymbol{v}$ is the additive Gaussian measurement noise. The process and measurement Gaussian white noises $\boldsymbol{w}$ and $\boldsymbol{v}$ are characterized by a null mean with diagonal covariance matrices $\boldsymbol{Q}$ and $\boldsymbol{R}$, respectively [29].

The Gaussian white noise $\boldsymbol{w_f}$ referred to the Random Walk modelling of the friction-variation functions is a subset of the process noise $\boldsymbol{w}$.

Therefore, it is characterized by a null mean and its covariance matrix is constituted by the first four elements along the diagonal of the $\boldsymbol{Q}$ matrix.

The terms $F_{rx,k} = \left(\frac{N}{R_{eff}}\right) d_{x,k}$ and $F_{ry,k} = \left(\frac{N}{R_{eff}}\right) d_{y,k}$ in Equation (3.41) are the restoring components of the reaction forces, while the frictional components are expressed as:

$$F_{fricx,k} = N \ \sin(\theta_k) \ \tanh(\alpha \ v_{x,k})(x_{5,k} \ R_{n1} \ x_{2,k} + x_{6,k} \ R_{n2} \ x_{4,k}) \tag{3.49}$$
$$F_{fricy,k} = N \ \cos(\theta_k) \ \tanh(\alpha \ v_{y,k})(x_{5,k} \ R_{n1} \ x_{2,k} + x_{6,k} \ R_{n2} \ x_{4,k}) \tag{3.50}$$

where N is the vertical load acting on the isolator and α is a slope-form factor relative to the hyperbolic tangent function.

The hyperbolic tangent function is employed to avoid the intrinsic discontinuity of the sign function, usually enrolled to describe the force-displacement behaviour of frictional isolators (see Equation (3.41)).

An α factor equal to 100 was found by attempts to be large enough to guarantee a very sharp transition between -1 and +1.

The parameters R_{n1} and R_{n2} represent the normalized radii R_1 and R_2, defined as $R_{n1} = \frac{R_1}{R_1+R_2}$ and $R_{n2} = \frac{R_2}{R_1+R_2}$.

For a double CSS isolator with identical sliding surfaces, i.e., $R_1 = R_2 = R$, the normalized radii count $R_{n1} = R_{n2} = \frac{R}{2R} = 0.5$.

In Figure 3.11 the estimation procedure is summarized, pointing out the input variables for both the CUKF and numerical models or real CSS seismic isolators and the measurements obtained through the latter functional to improve the estimation provided by the CUKF.

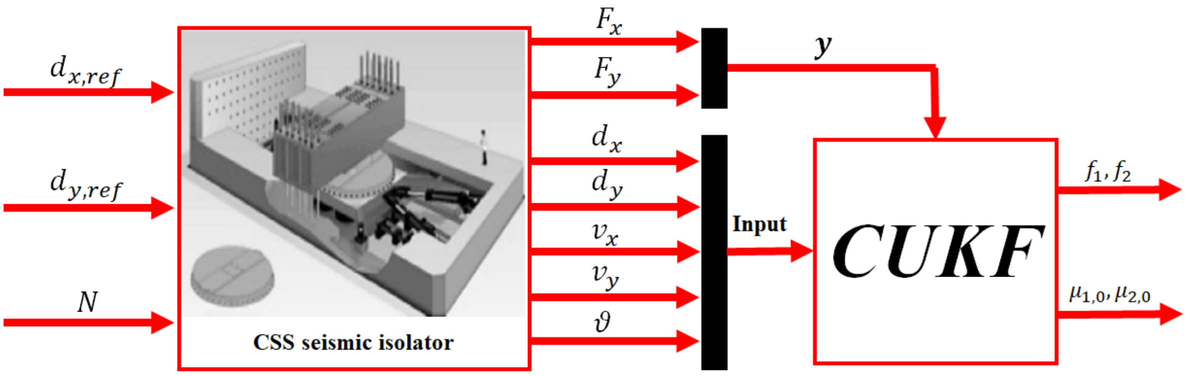

Figure 3.11. Estimation flow for monitoring CSS seismic isolators through CUKF.

4. RESULTS OF PROPOSED APPLICATIONS

In Chapter 3, estimator design models have been described for including them in model-based estimators represented by Kalman Filters (described in Chapter 2) for monitoring purposes.
The desired system state variables and parameters can be estimated through a good design of the model-based estimators. Therefore, a reliable estimator design model able to capture the fundamental dynamics of the system to be monitored is crucial for finalizing the design of a Kalman Filter.
In this Chapter, the results of estimations provided by Kalman Filters, coupled with the developed estimator design models, are presented for all the application fields mentioned in previous Chapters. In the following, estimator design models and Kalman Filters employed for each application are indicated:

- **Monitoring of railway anti-yaw suspension components** (Section 4.1) – for this application, the employed estimator design model has been described in Section 3.1. The CUKF (see Section 2.2.4) has been used as a model-based estimator;
- **Estimation of sideslip angle and left and right lateral tire-road friction coefficients** (Section 4.2.1) – for this application, the employed estimator design model has been described in Section 3.2.1. The EKF (see Section 2.2.2) has been used as a model-based estimator;
- **Estimation of sideslip angle and lateral tire-road friction coefficient with no interaction modelling** (Section 4.2.2) – for this application, the employed estimator design model has been described in Section 3.2.2. The EKF (see Section 2.2.2) has been used as a model-based estimator;
- **Estimation of the instantaneous friction coefficients of sliding isolators subjected to bi-directional orbits** (Section 4.3) – for this application, the employed estimator design model has been described in Section 3.3. The CUKF (see Section 2.2.4) has been used as a model-based estimator;

Furthermore, the Normalized Root Mean Squared Error has been employed as an indicator of the estimation quality for all the presented applications [128].

The NRMSE is defined as follows:

$$NRMSE = \frac{\sqrt{\frac{\sum_{i=1}^{N}(\hat{y}_i - y_i)^2}{N}}}{n_f}$$

where:

- N is the number of samples of the considered signal y;
- $\hat{y}$ is the estimation of the signal y;
- n_f is a normalization factor typically computed as the range of values of y or as the mean of values of y. Therefore, $n_f = \max(y) - \min(y)$ or $n_f = \frac{\sum_{i=1}^{N} y_i}{N}$.

Typically, values of the NRMSE close to zero indicate a good estimation quality, while values close to one indicate a poor estimation quality.

4.1. Monitoring of railway anti-yaw suspension components

Estimated variables obtained from the adopted model-based technique based on the CUKF for monitoring railway anti-yaw suspension components have been compared with a complete and detailed multibody railway vehicle model developed through the commercial software SIMPACK 18.4.
The SIMPACK software [119] is a well-established and widely used tool for the design of railway vehicles, as well as for research. It enables for including nonlinear wheel-rail contact models in railway vehicles ones. The employment of this validated software is nowadays encouraged by the scientific community in place of experimental tests since it allows to reduce expensive activities, that can be calendarized at the final step of the product development [16,24,130,131].

The employment of a detailed model of the entire vehicle is of crucial importance for the validation of the estimation technique.
The vehicle model describes a standard passenger coach equipped with two bogies, each one having two wheelsets. The parameters of the vehicle are taken from a report [118], issued by the European Railway Research Institute (ERRI).

They describe the passenger coach of the type Avmz, which is the German variant of the Eurofima coach. This vehicle uses Fiat 0270 bogies type, which are equipped with yaw dampers. The primary vertical springs, the bushings of the trailer arms of the axleboxes, and the secondary flexicoil suspension are described as springs having linear characteristics. Furthermore, the secondary suspension contains a lateral bumpstop with a clearance of 6 mm to each side. The dampers, i.e., the primary vertical dampers, the secondary vertical, lateral, and anti-yaw dampers, are hydraulic dampers; in the model, they are described by a damper, which has a piecewise linear characteristic defined by points, and a stiff linear spring arranged in series.

Linear springs with constant stiffness have been employed for describing the springs included in the anti-yaw suspension components.

For the analysis, the damper force of the yaw damper is multiplied by a factor f_{YD} with $0 \leq f_{YD} \leq 1$ in order to reproduce the degradation of the damper; here, $f_{YD} = 1$ describes the case of the fully intact yaw damper.

In order to take the flexibility of the track into account, each wheelset is supported by one rigid body, which is connected to the environment by linear viscoelastic elements and can perform lateral and vertical translations and a roll rotation; an illustration is given in [132].

An approximative description of the track flexibility is reasonable, since a completely rigid track model can produce unrealistically high dynamic wheel-rail forces.

The simulated railway vehicle model representing a passenger coach is running on a straight track with vertical and lateral rail irregularities at a constant running speed of 250 km/h = 69.4 m/s, typical for high-speed railway vehicles [15]. Vertical and lateral irregularities have been applied to each rail. Regarding the wheel-rail contact geometry, the wheel profile S1002 and the rail profile with a rail inclination of 1:40 and a track gauge of 1435 mm have been chosen. A high equivalent conicity characterizes the previously described contact geometry. Therefore, a stronger tendency for bogie hunting than carbody hunting is expected. A friction coefficient of $\mu = 0.4$ has been assigned to the wheel-rail contact. It leads to a high level of tangential forces with consequent strong excitation of the vehicle. The chosen scenario allows obtaining a very active attitude of anti-yaw dampers. Nonlinearities related to the wheel-rail contact constituted of the nonlinear function characterizing rolling radii versus the lateral displacement of the wheelset, and the nonlinear relation between creepages and tangential contact forces, have been taken into account.

The results illustrated below include the estimation of the anti-yaw damping, and the estimation of the measurements. Two kinds of tests have been executed:

1) estimation of the anti-yaw damping C_{axd} in no fault condition ($f_{YD} = 1$) and in a fault condition (degrade of $f_{YD} = 40\%$ from the nominal value) with a five sensors configuration;
2) estimation of the anti-yaw damping C_{axd} in no fault condition and in a fault condition (degrade of $f_{YD} = 40\%$ from the nominal value) with a three sensors configuration.

Furthermore, for both no-fault and fault conditions of anti-yaw dampers in the case of the five sensors configuration, the estimation of the stiffness for monitoring springs included in the anti-yaw suspension components has been considered.

The properties of anti-yaw dampers C_{axd} in no fault condition and in fault condition are portrayed by the arrays of force vs speed in Figure 4.1.
In Figure 3.2, anti-yaw dampers are represented to indicate their effective installation in parallel. Therefore, considering the parallel configuration of anti-yaw dampers, the anti-yaw damping coefficient C_{axd} is the resulting one, while $0.5C_{axd}$ is the damping coefficient of one anti-yaw damper.

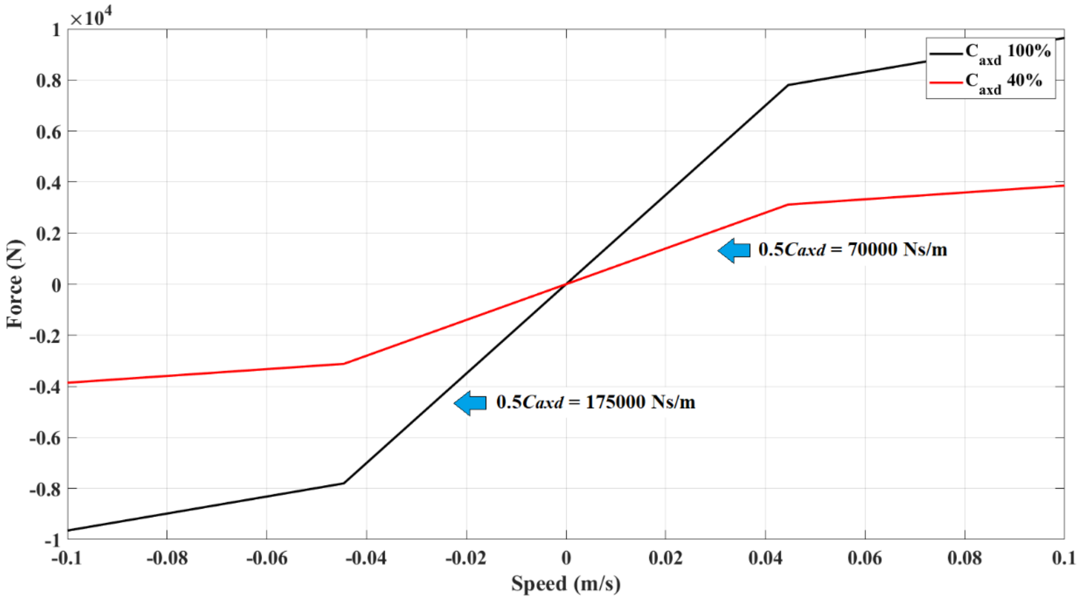

Figure 4.1. Characteristics of the anti-yaw damper (C_{axd}) in fault and in no fault condition.

4.1.1. Test with five sensors configuration

This test has been employed to verify the sensitivity of the estimator to the variation of the operating conditions of the anti-yaw dampers. The measurements vector related to the five sensors configuration is $\boldsymbol{y} = [\ddot{y}_{bd}, \ddot{y}_b, \ddot{y}_{w1}, \ddot{y}_{w2}, \dot{\psi}_b]^T$. Figure 4.2 shows the estimation of the anti-yaw damping, compared with the linearized value of the damping in no fault condition (C_{axd} = 350000 Ns/m) (Figure 4.1).

The CUKF is able to estimate the anti-yaw damping, converging rapidly to the target value in a very short time thanks to the employment of constraints on the states.

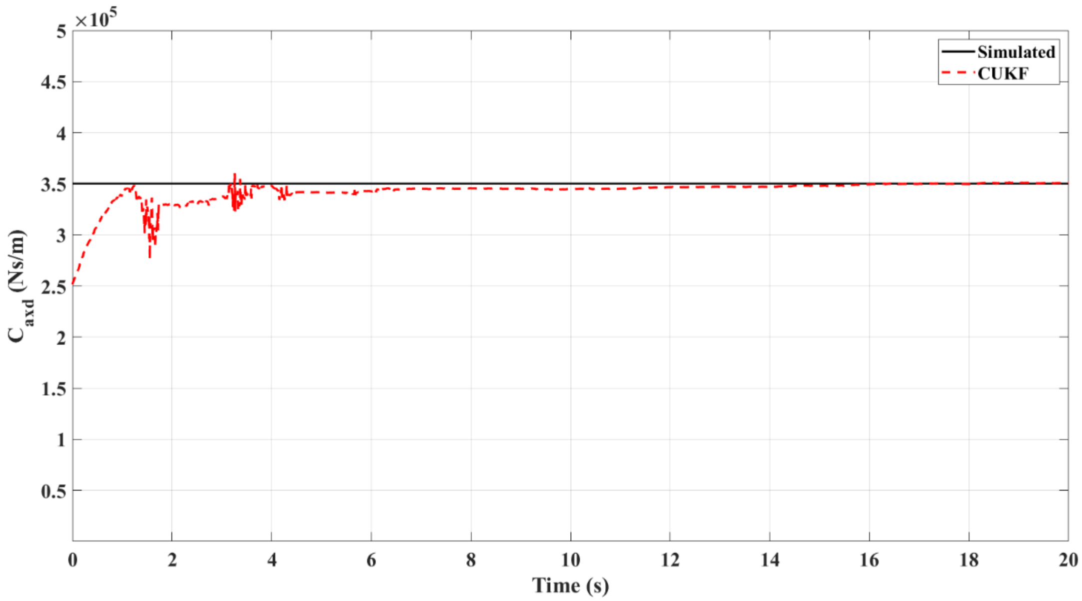

Figure 4.2. Anti-yaw damping C_{axd} (no fault condition – five sensors configuration).

In addition to the parametric estimation of anti-yaw damping, the five measurements have been estimated. The comparison between the simulated measurements and the estimated measurements is an indicator of the CUKF capability to correctly estimate the states.

The estimated measurements are strictly connected to the states of the system (see Equation (3.9)).

The estimation of carbody lateral acceleration and leading bogie frame lateral acceleration (Figures 4.3, 4.4) are practically superimposed on the simulated values and confirm the validity of the suggested technique.

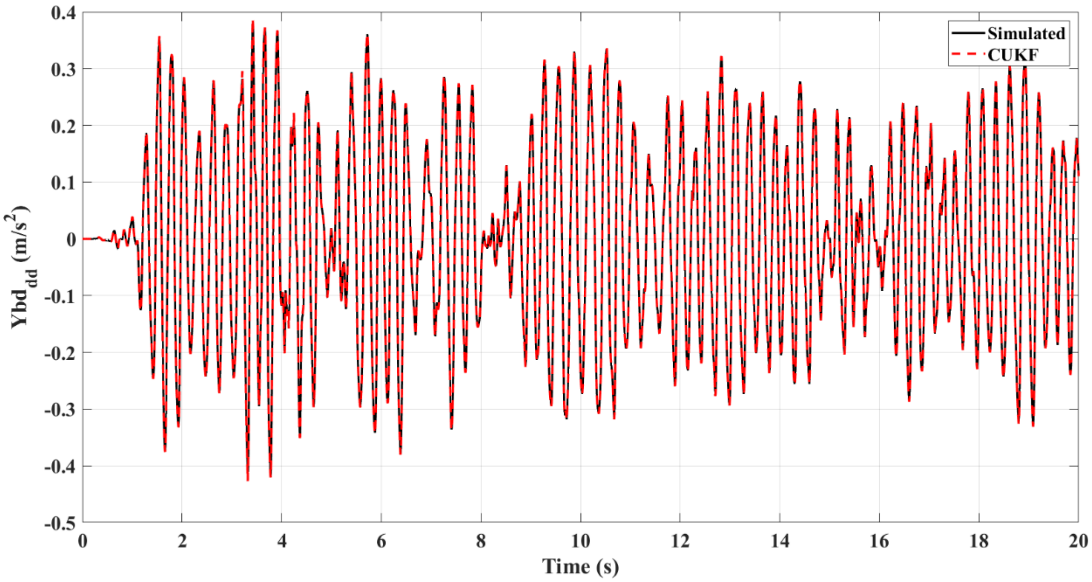

Figure 4.3. Carbody lateral acceleration $\ddot{y}_{bd}$ (no fault condition – five sensors configuration).

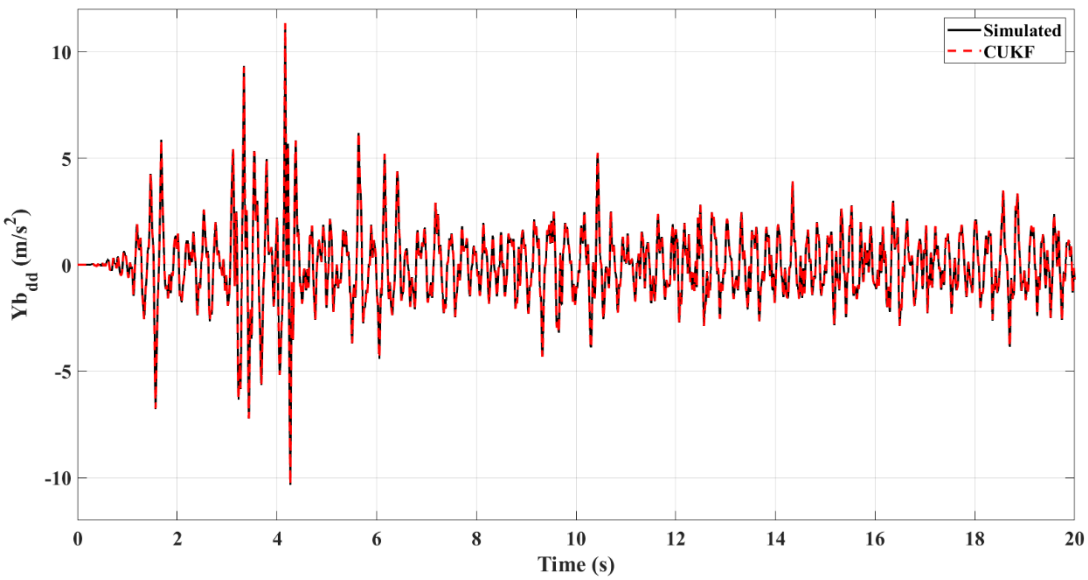

Figure 4.4. Leading Bogie frame lateral acceleration $\ddot{y}_b$ (no fault condition – five sensors configuration).

Figure 4.5 and Figure 4.6 refer to lateral acceleration of leading and trailing wheelset, respectively. The time histories confirm the quality, capability and accuracy of the employed technique. The same excellent behaviour can be observed in Figure 4.7 that represents the leading bogie frame yaw angular velocity.

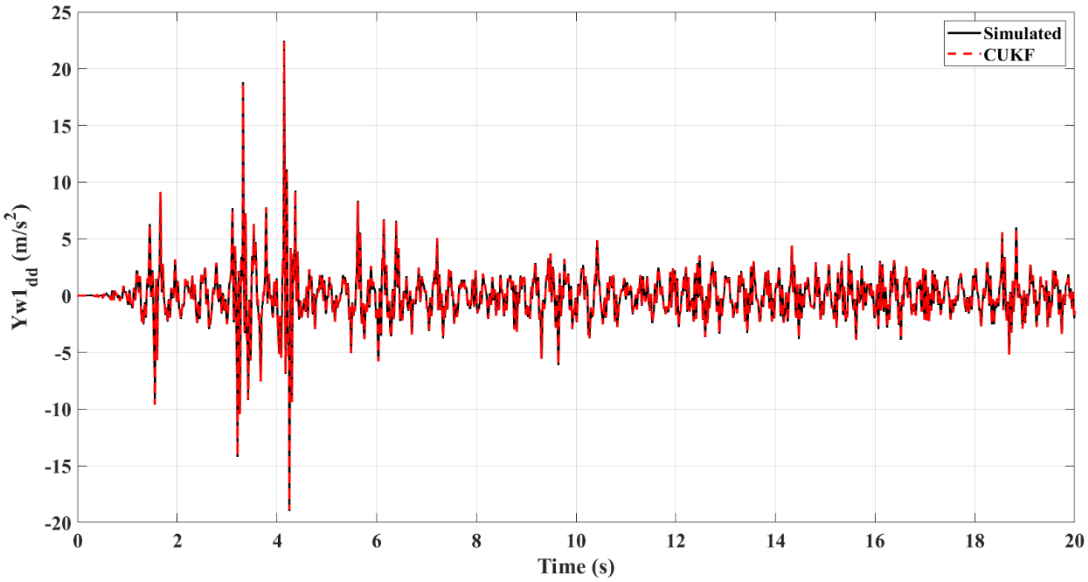

Figure 4.5. Leading Wheelset lateral acceleration $\ddot{y}_{w1}$ (no fault condition – five sensors configuration).

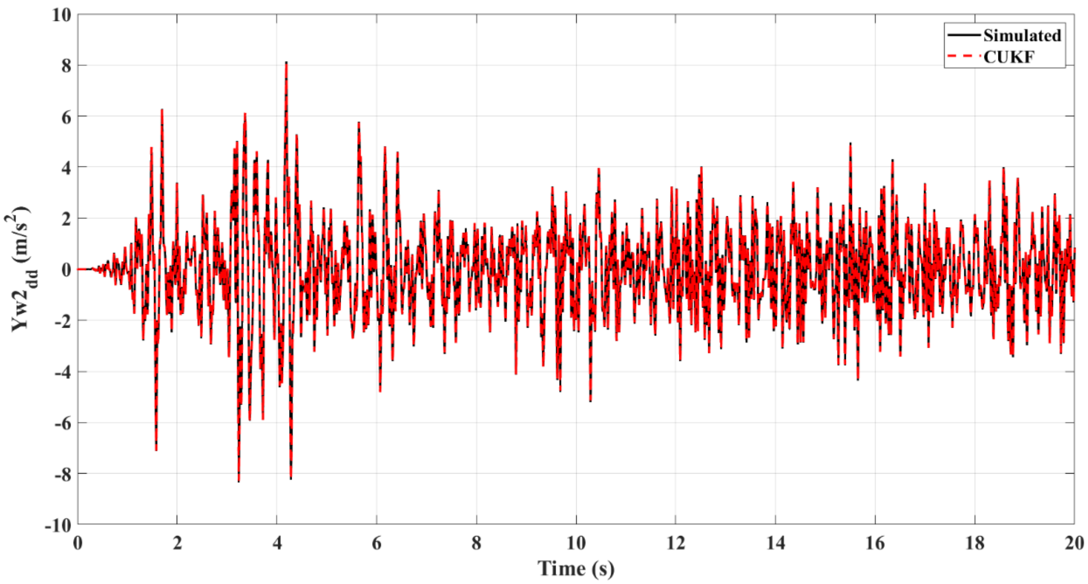

Figure 4.6. Trailing Wheelset lateral acceleration $\ddot{y}_{w2}$ (no fault condition – five sensors configuration).

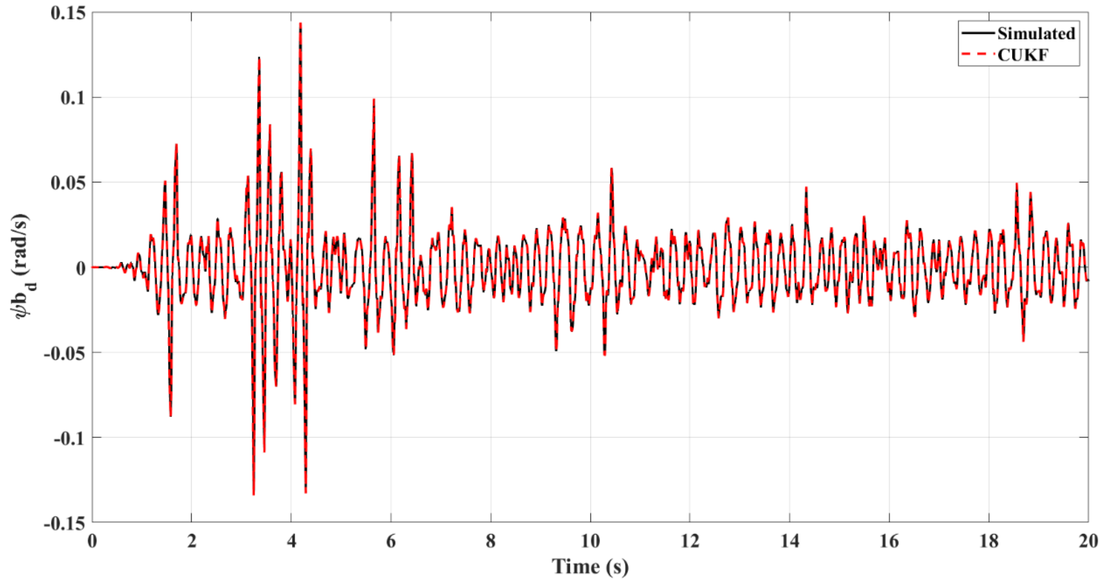

Figure 4.7. Leading Bogie frame yaw angular velocity $\dot{\psi}_b$ (no fault condition – five sensors configuration).

Even if the current focus is the anti-yaw damping monitoring, also forces and moments are illustrated. Figure 4.8 shows the time histories of the lateral contact forces and moments acting on leading and trailing wheelsets, in order to demonstrate the validity of the RWM approach, functional for the anti-yaw damping monitoring.

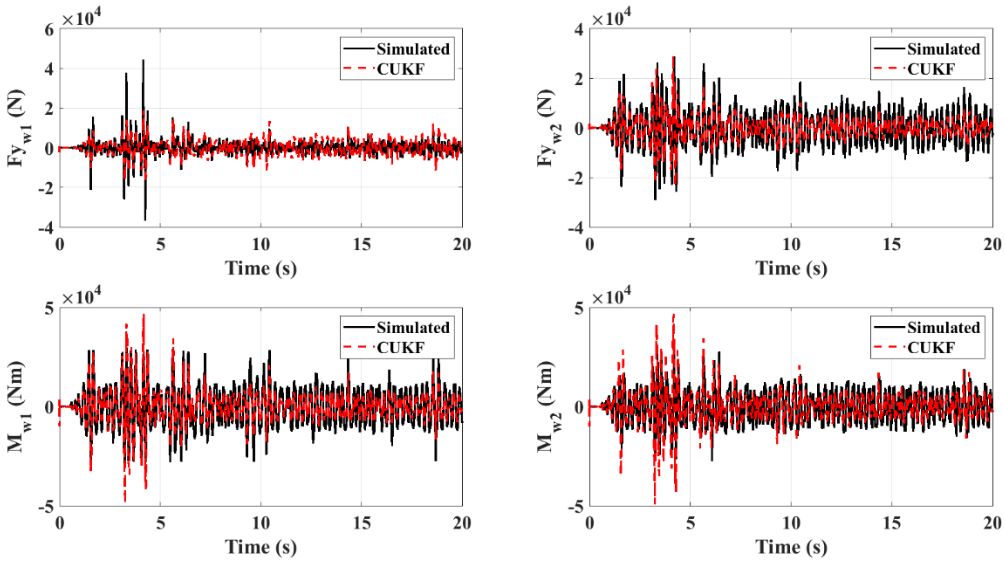

Figure 4.8. Lateral wheel-rail contact forces F_{yw1}, F_{yw2} and moments M_{w1}, M_{w2} (no fault condition – five sensors configuration).

The results highlight that the CUKF is able to estimate the actual forces trough the employment of the RWM approach, allowing a priori no knowledge of both deterministic wheel-rail contact models and track irregularities.
The time histories confirm the goodness of the Random Walk Model approach. The presence of the additional estimation of the first-time derivative works as "degree-of-freedom" of the estimator that greatly improves the estimation of the forces and moments.

The quality of the estimation has been evaluated also through the NRMSE indicator. NRMSE values are reported in Table 4.1 for measurements, wheel-rail contact forces and moments and the anti-yaw damping.
The NRMSE for all the mentioned variables is near to zero highlighting the advantages, in terms of estimation quality, that can be reached by means of the constrained approach applied to the proposed estimator design model.

Table 4.1. NRMSE values (no fault condition – five sensors configuration).

Variable name	***NRMSE***
$\ddot{y}_{bd}$	0.0017
$\ddot{y}_{b}$	7.89×10^{-4}
$\ddot{y}_{w1}$	5.15×10^{-4}
$\ddot{y}_{w2}$	0.0013
$\dot{\psi}_{b}$	2.72×10^{-4}
F_{yw1}	0.0401
F_{yw2}	0.0702
M_{w1}	0.0828
M_{w2}	0.1377
C_{axd}	0.0346

Figure 4.9 shows the estimation of the anti-yaw damping compared with the linearized value of the damping in fault condition (C_{axd} = 140000 Ns/m), obtained from the characteristic curve of the anti-yaw dampers (Figure 4.1). The estimator is able to detect the presence of a fault in the anti-yaw damper and therefore of a degradation of the damping.

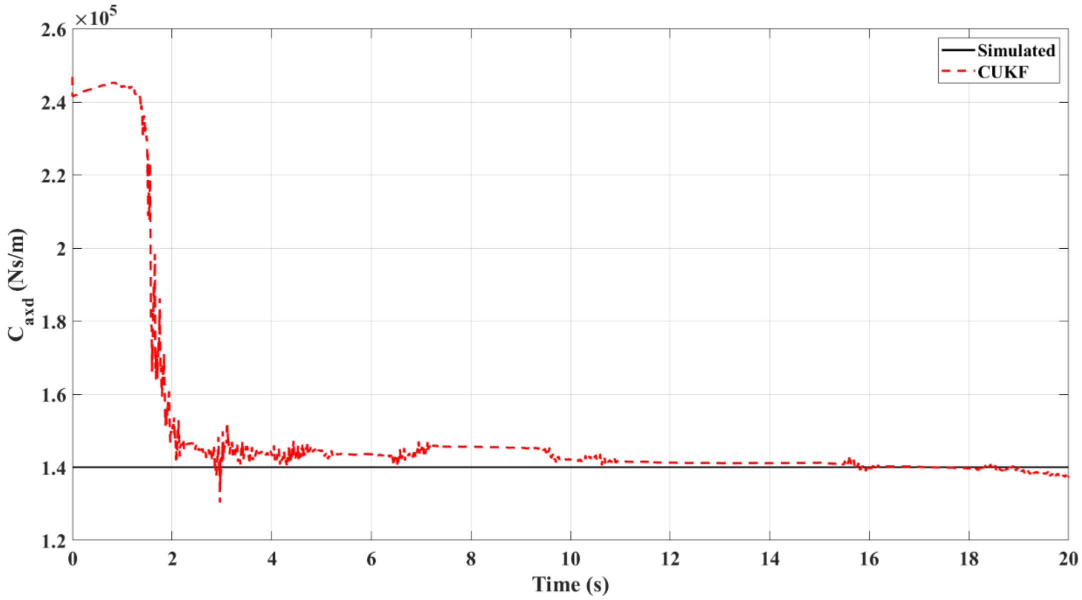

Figure 4.9. Anti-yaw damping C_{axd} (fault conditions – five sensors configuration).

The estimated measurements (Figures 4.10, 4.11, 4.12, 4.13, 4.14) fully agree with the simulated values. This is very important since even if the anti-yaw damper is damaged, the CUKF continues to perfectly estimate the measurements and therefore the states that compose them.

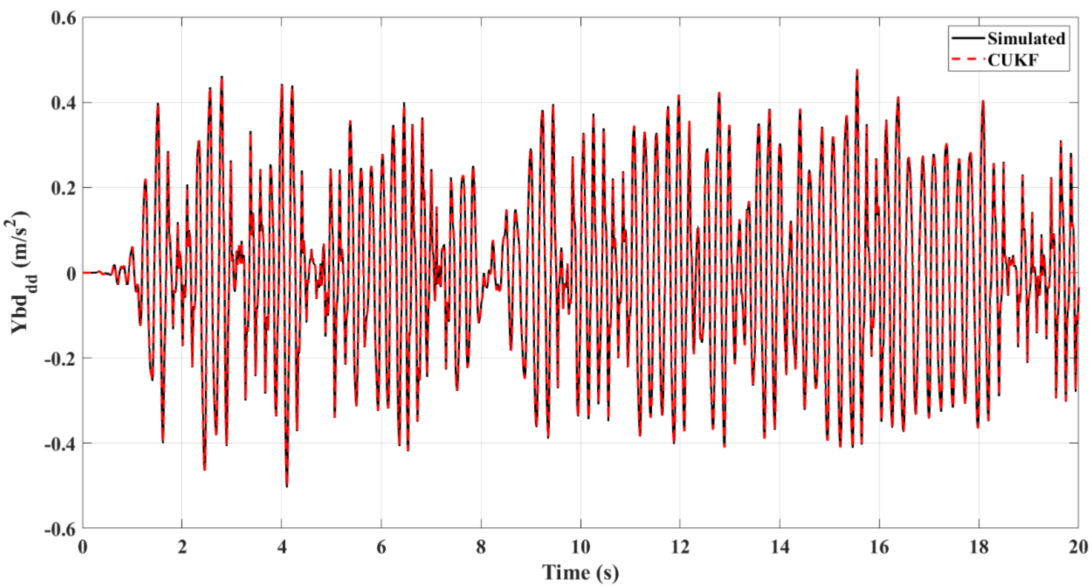

Figure 4.10. Carbody lateral acceleration $\ddot{y}_{bd}$ (fault condition – five sensors configuration).

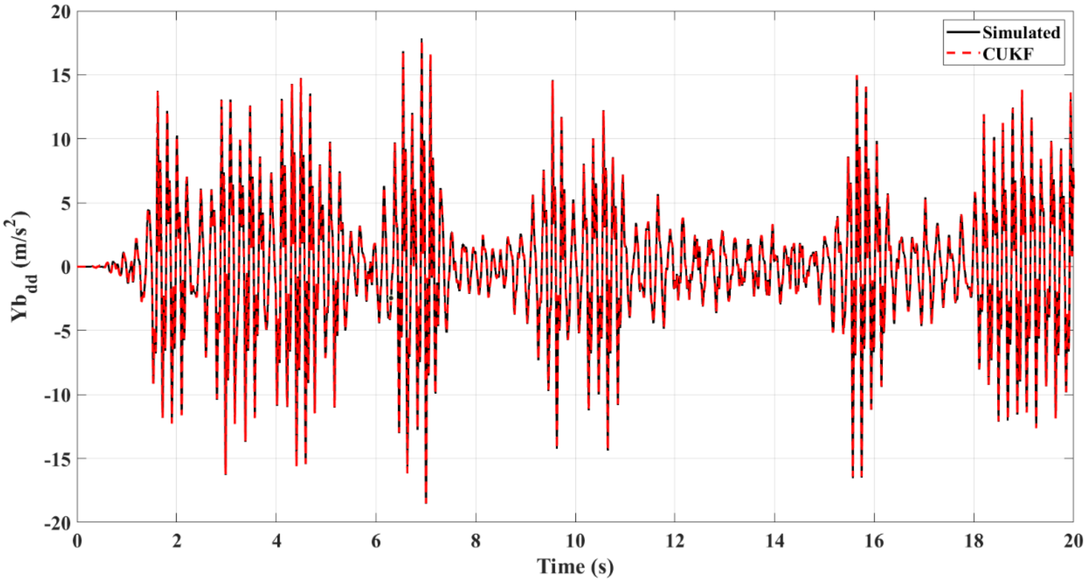

Figure 4.11. Leading Bogie frame lateral acceleration $\ddot{y}_b$ (fault condition – five sensors configuration).

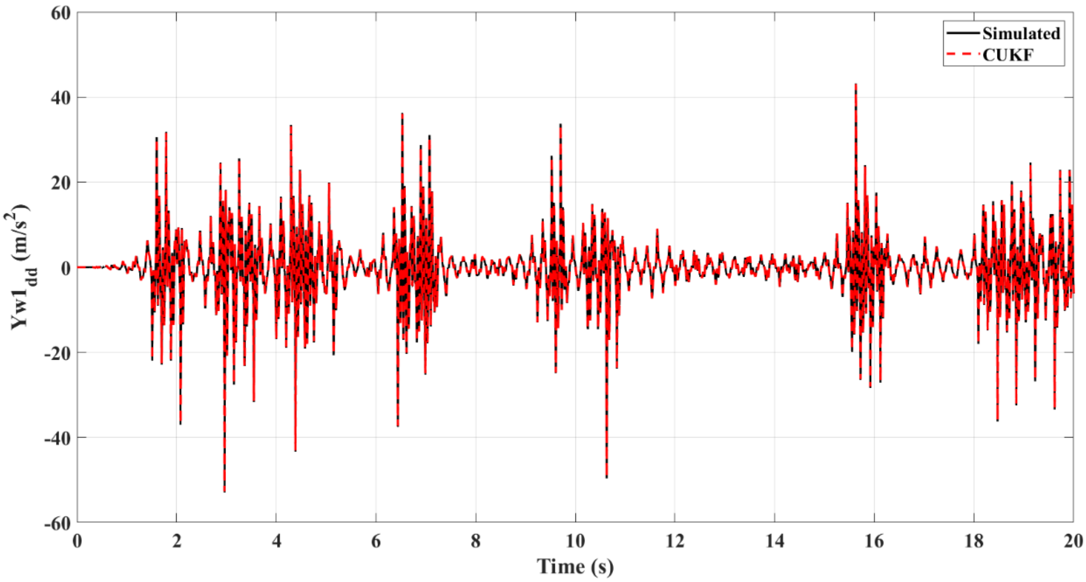

Figure 4.12. Leading Wheelset lateral acceleration $\ddot{y}_{w1}$ (fault condition – five sensors configuration).

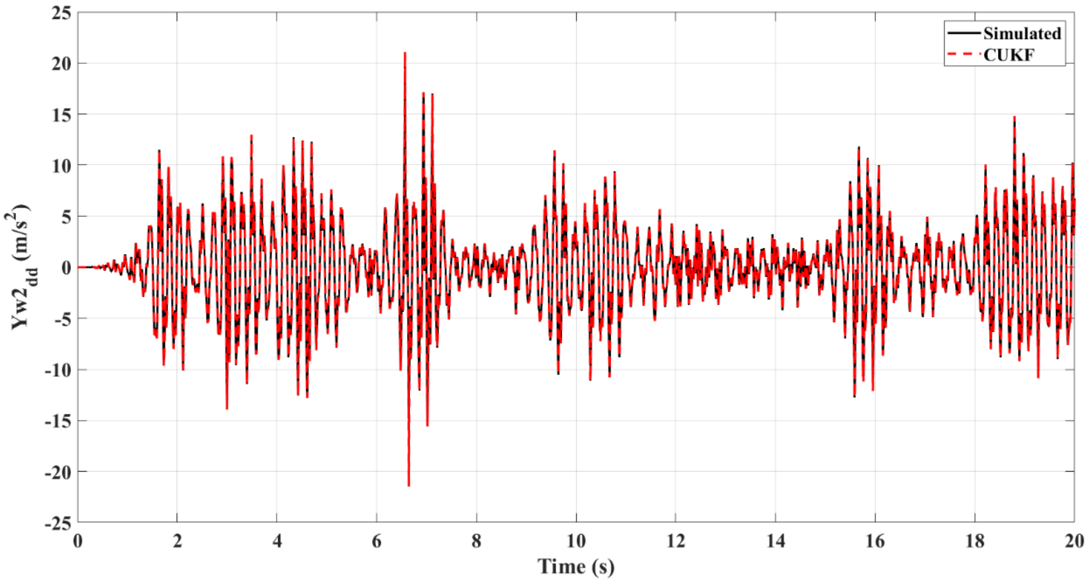

Figure 4.13. Trailing Wheelset lateral acceleration $\ddot{y}_{w2}$ (fault condition – five sensors configuration).

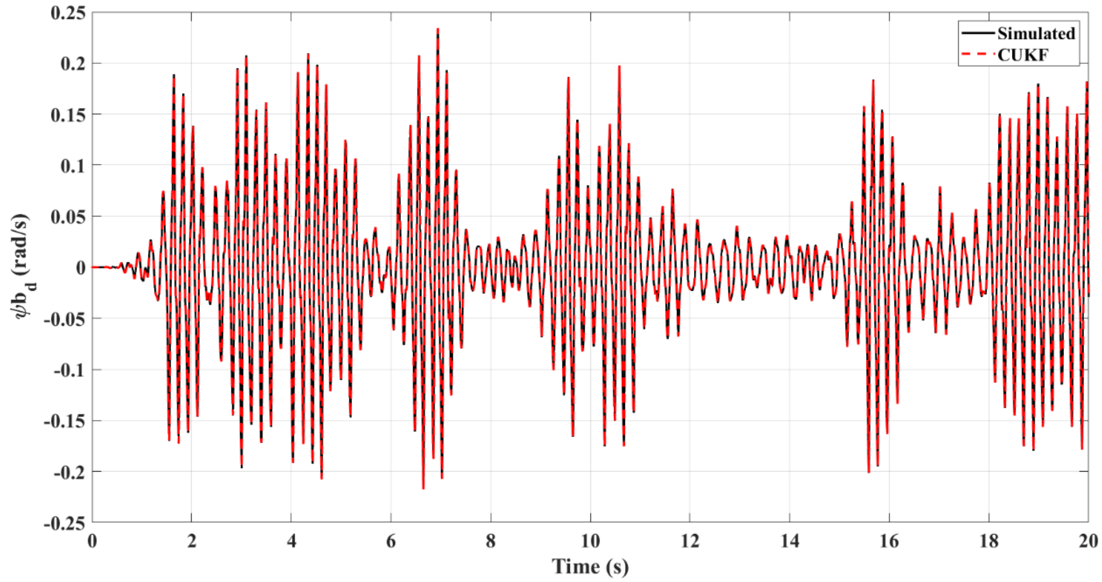

Figure 4.14. Leading Bogie frame yaw angular velocity $\dot{\psi}_b$ (fault condition – five sensors configuration).

The presence of a fault in the anti-yaw dampers changes the dynamic response of the railway vehicle as shown by the previous Figures.

The CUKF is able to estimate correctly the measurements in this new condition and is sensitive to changes in the railway vehicle dynamics.

The estimated wheel rail contact forces and moments are compared with simulated ones in Figure 4.15. The CUKF is able to manage the behaviour of the wheel-rail contact interactions by avoiding a priori knowledge of their modelling, despite overestimates and underestimates.

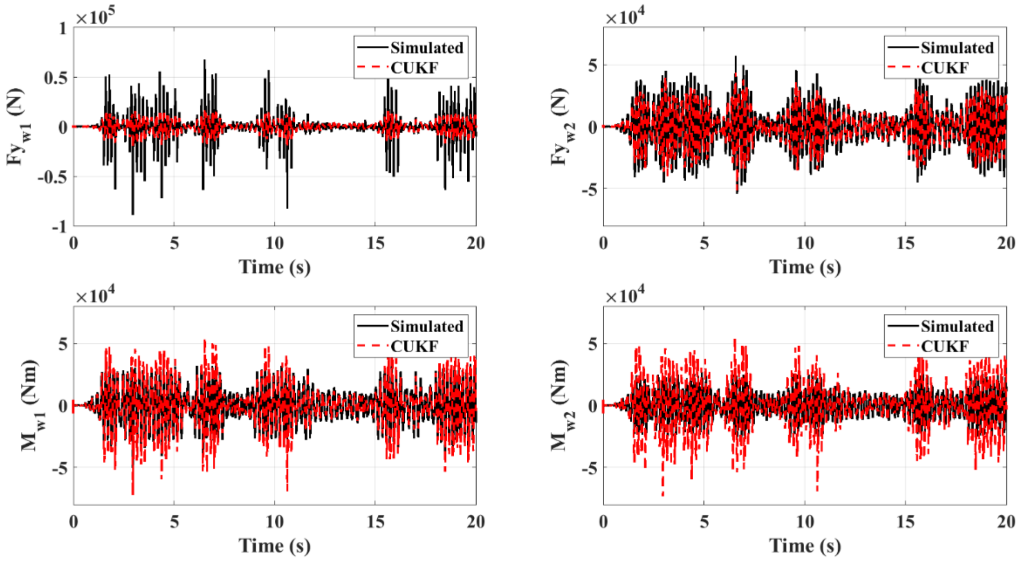

Figure 4.15. Lateral wheel-rail contact forces F_{yw1}, F_{yw2} and moments M_{w1}, M_{w2} (fault condition – five sensors configuration).

The NRMSE values reported in Table 4.2 are near zero confirming the good estimation quality of the proposed estimation technique.

Table 4.2. NRMSE values (fault condition – five sensors configuration).

Variable name	***NRMSE***
$\ddot{y}_{bd}$	0.0011
$\ddot{y}_{b}$	0.0022
$\ddot{y}_{w1}$	0.001
$\ddot{y}_{w2}$	0.0023
$\dot{\psi}_{b}$	6.39×10^{-4}
F_{yw1}	0.0425
F_{yw2}	0.0829
M_{w1}	0.0838
M_{w2}	0.325
C_{axd}	0.175

4.1.2. Test with three sensors configuration

Accelerometers are often undesired on the wheelsets due to the severe vibration environment. So, this test refers to a three sensors configuration constituted by one gyroscope and two accelerometers, to obtain the same measurements of the previous test, except the lateral acceleration of the two wheelsets. The measurements vector related to the three sensors configuration is $\boldsymbol{y} = \left[\ddot{y}_{bd}, \ddot{y}_b, \dot{\psi}_b\right]^T$.

The CUKF is able to estimate the anti-yaw damping with a good estimation quality as shown in Figure 4.16 in the new measurement configuration.

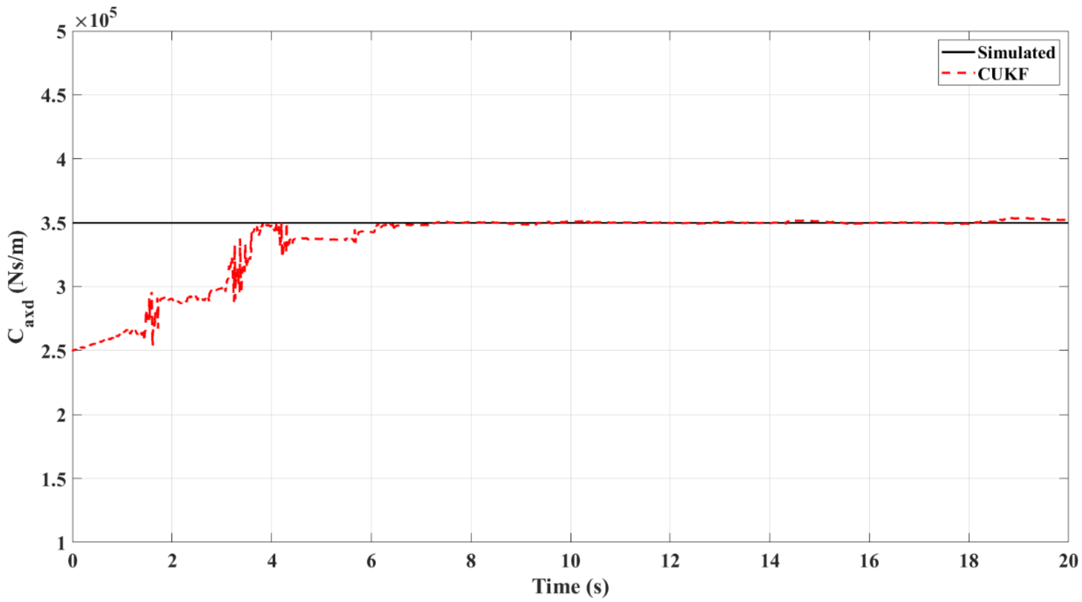

Figure 4.16. Anti-yaw damping C_{axd} (no fault condition – three sensors configuration).

Estimations of carbody lateral acceleration and leading bogie frame lateral acceleration (Figures 4.17, 4.18) are practically superimposed on simulated values.

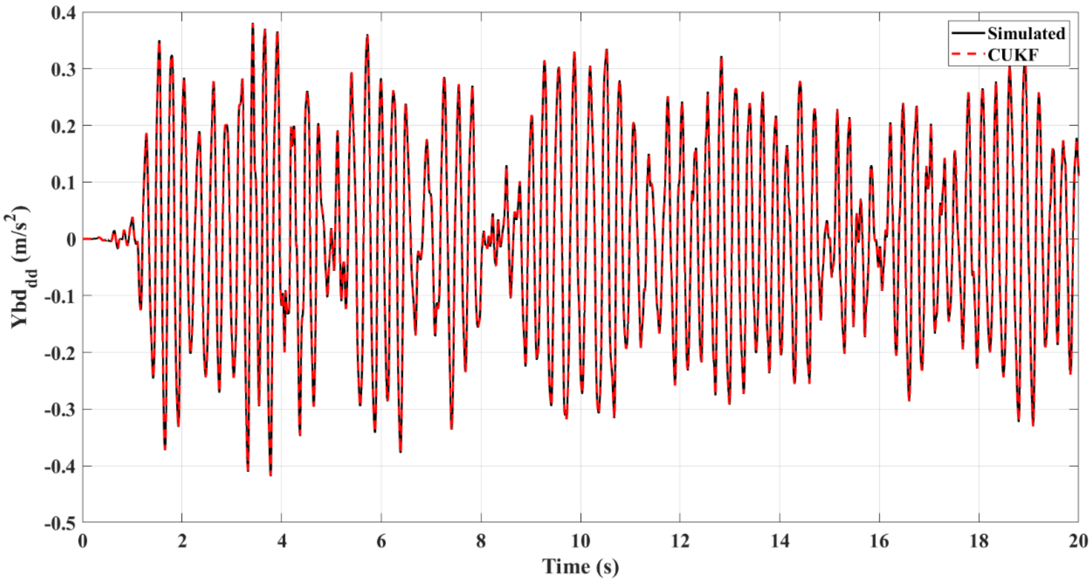

Figure 4.17. Carbody lateral acceleration $\ddot{y}_{bd}$ (no fault condition – three sensors configuration).

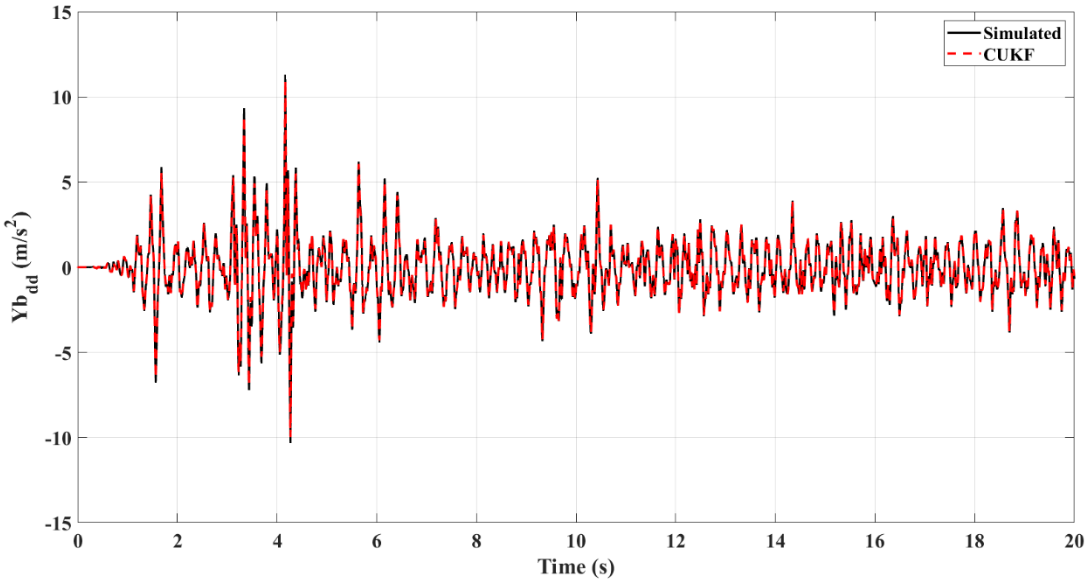

Figure 4.18. Leading Bogie frame lateral acceleration $\ddot{y}_b$ (no fault condition – three sensors configuration).

The time history of the leading bogie frame yaw angular velocity is illustrated in Figure 4.19 confirming an excellent quality of the estimation.

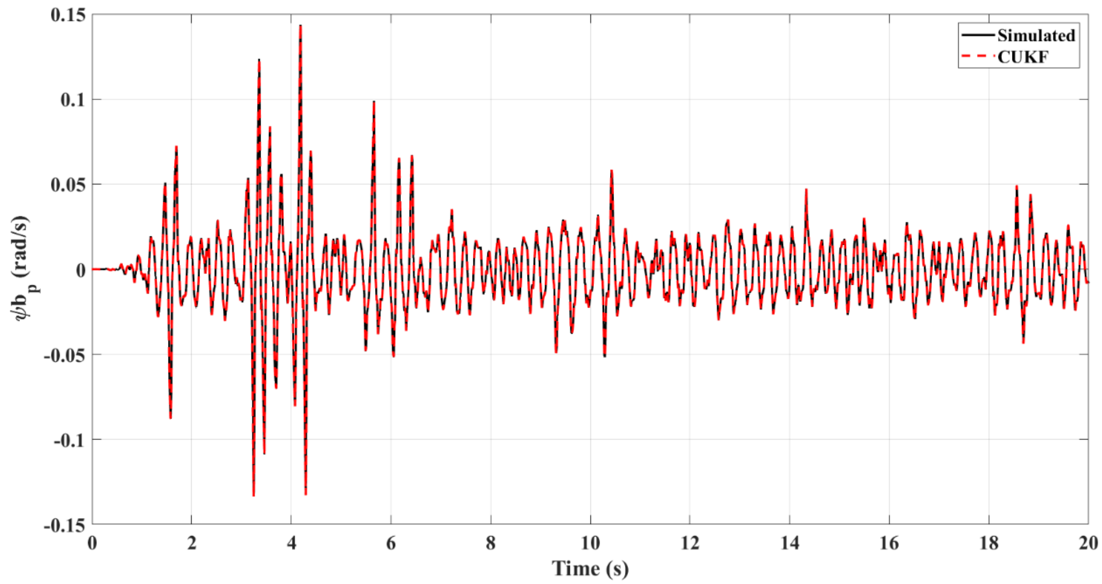

Figure 4.19. Leading Bogie frame yaw angular velocity $\dot{\psi}_b$ (no fault condition – three sensors configuration).

Pointing out that the goal of the proposed model-based estimation technique is the monitoring of anti-yaw suspension components, the estimated wheel-rail contact forces and moments are compared with simulated ones in Figure 4.20. The CUKF can manage the behaviour of the wheel-rail contact interactions by avoiding a priori knowledge of their modelling, despite overestimates and underestimates.

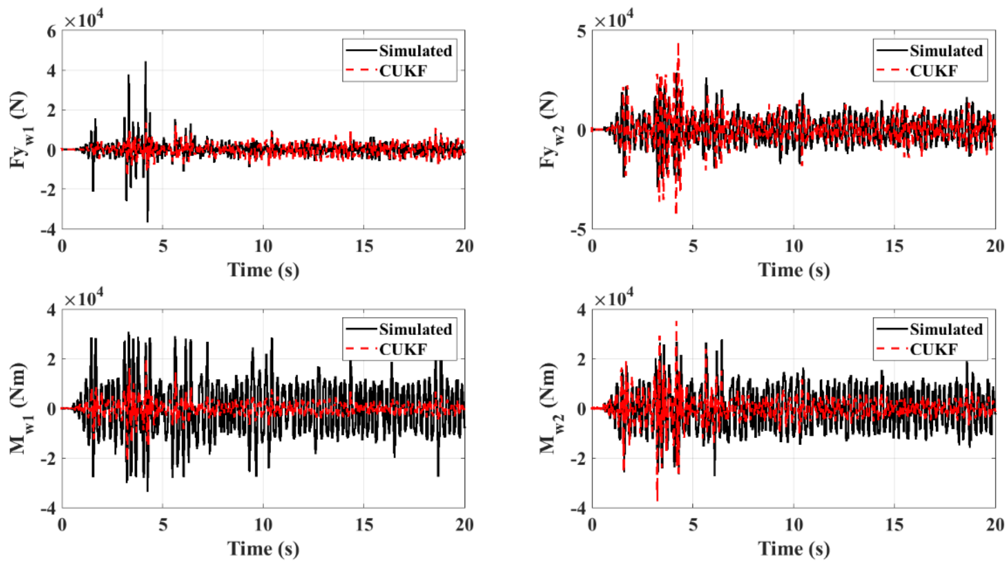

Figure 4.20. Lateral wheel-rail contact forces F_{yw1}, F_{yw2} and moments M_{w1}, M_{w2} (no fault condition – three sensors configuration).

The NRMSE values reported in Table 4.3 are near zero confirming the good estimation quality of the proposed estimation technique.

Table 4.3. NRMSE values (no fault condition – three sensors configuration).

Variable name	***NRMSE***
$\ddot{y}_{bd}$	3.45×10^{-4}
$\ddot{y}_b$	0.0043
$\dot{\psi}_b$	2.49×10^{-5}
F_{yw1}	0.0443
F_{yw2}	0.184
M_{w1}	0.132
M_{w2}	0.129
C_{axd}	0.075

With reference to the fault condition, Figure 4.21 highlights the capability of the proposed estimator to feel the degrade in anti-yaw dampers.

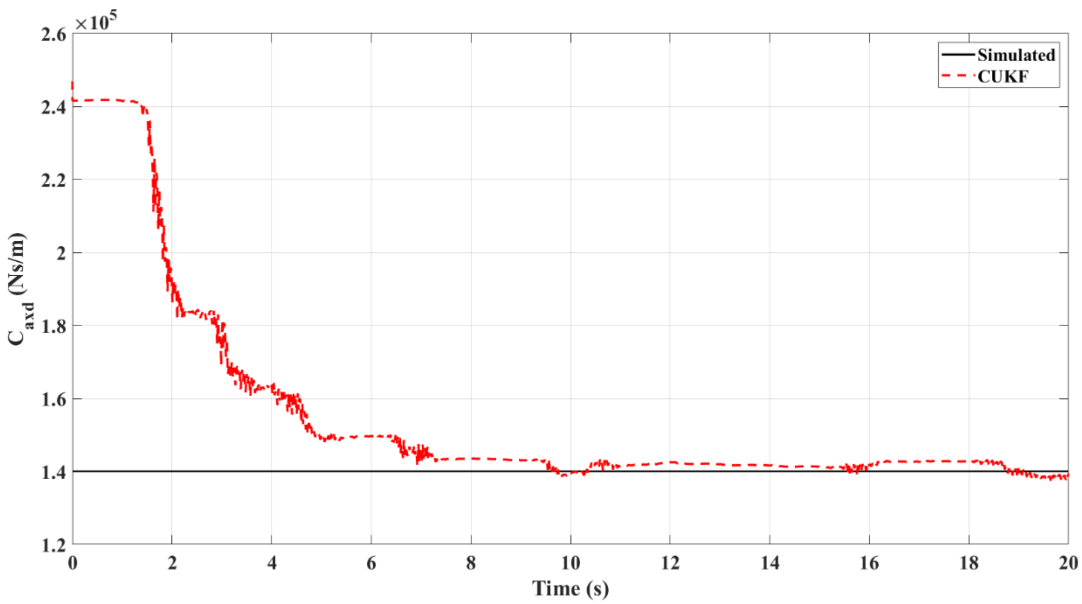

Figure 4.21. Anti-yaw damping C_{axd} (fault condition – three sensors configuration).

The estimated measurements (Figures 4.22, 4.23, 4.24) confirm the goodness of the proposed model-based technique. This is very important since even if the anti-yaw damper suffers a fault, the CUKF continues to perfectly estimate the measurements and therefore the states that compose them.

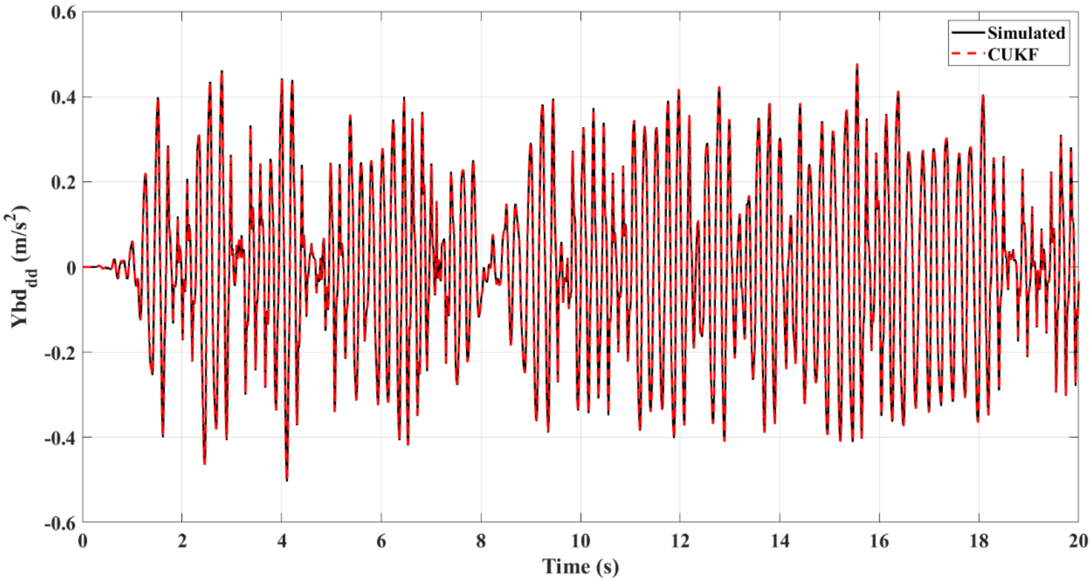

Figure 4.22. Carbody lateral acceleration $\ddot{y}_{bd}$ (fault conditions – three sensors configuration).

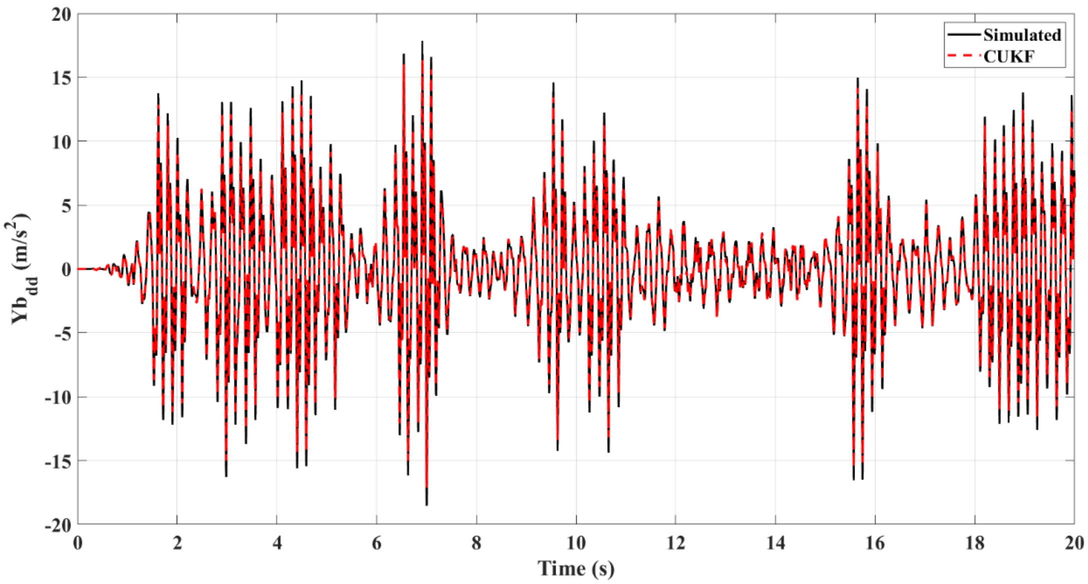

Figure 4.23. Leading Bogie frame lateral acceleration $\ddot{y}_b$ (fault conditions – three sensors configuration).

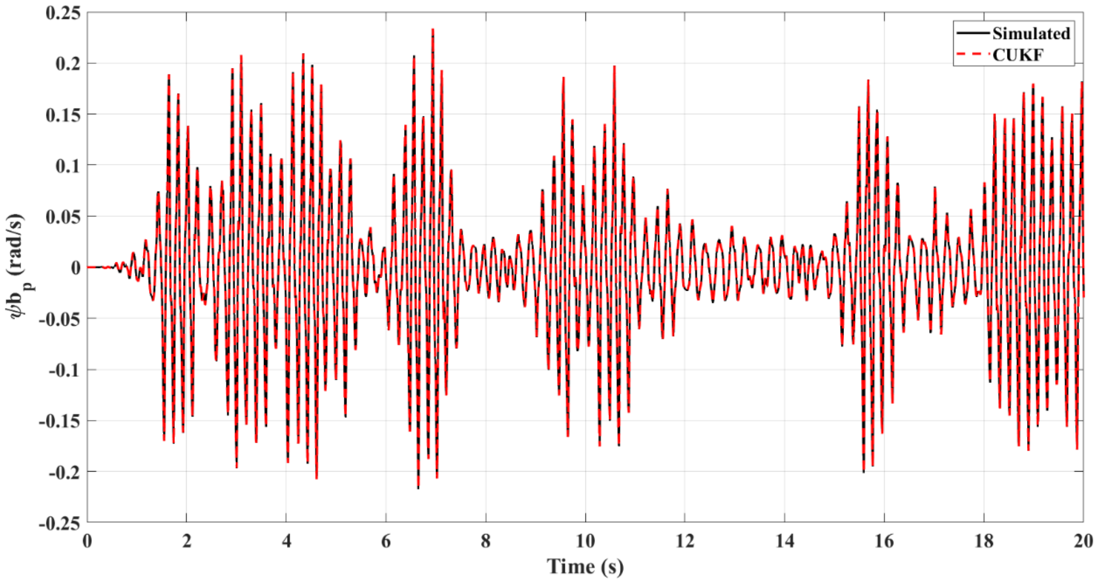

Figure 4.24. Leading Bogie frame yaw angular velocity $\dot{\psi}_b$ (fault conditions – three sensors configuration).

The estimated wheel-rail contact forces and moments are compared with simulated ones in Figure 4.25. The CUKF can manage the behaviour of the wheel-rail contact interactions by avoiding a priori knowledge of their modelling, despite overestimates and underestimates.

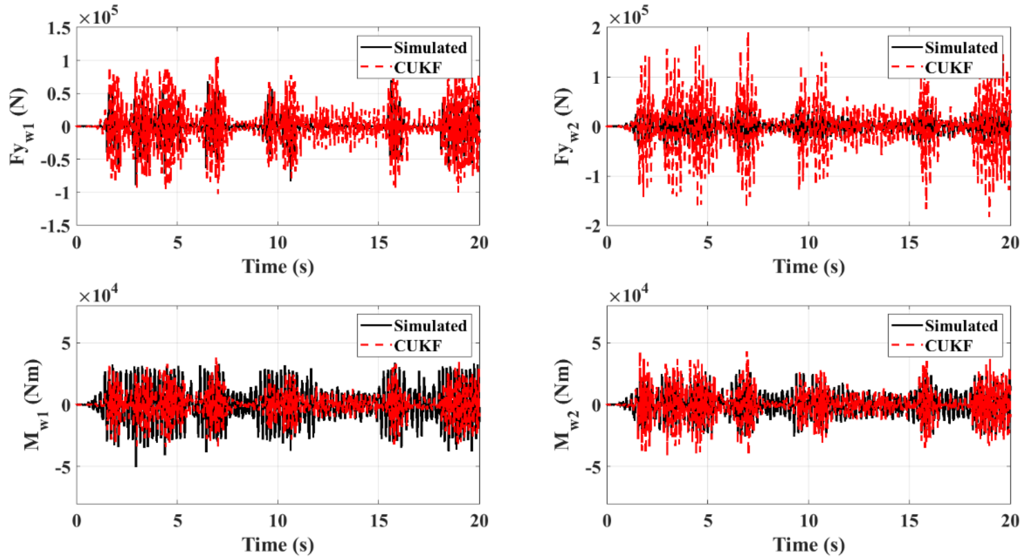

Figure 4.25. Lateral wheel-rail contact forces F_{yw1}, F_{yw2} and moments M_{w1}, M_{w2} (fault condition – three sensors configuration).

The NRMSE values reported in Table 4.4 are near zero confirming the good estimation quality of the proposed estimation technique.

Table 4.4. NRMSE values (fault condition – three sensors configuration).

Variable name	***NRMSE***
$\ddot{y}_{bd}$	0.0011
$\ddot{y}_{b}$	0.0099
$\dot{\psi}_{b}$	4.43×10^{-5}
F_{yw1}	0.192
F_{yw2}	0.381
M_{w1}	0.201
M_{w2}	0.189
C_{axd}	0.197

Plots confirm that the CUKF allows for estimating the anti-yaw damping and identifying the presence of a fault in anti-yaw dampers for railway vehicle condition monitoring.

4.1.3. Estimation of damping and stiffness related to anti-yaw suspension components: five sensors configurations

In addition to results previously shown, the coupled estimation of the anti-yaw damping C_{axd} and stiffness K_{axd} is presented taking into account the five sensors configuration. Figure 4.26 shows the comparison between the estimated anti-yaw damping and the linearized damping value related to the anti-yaw dampers in no-fault condition (C_{axd} = 350000 Ns/m).

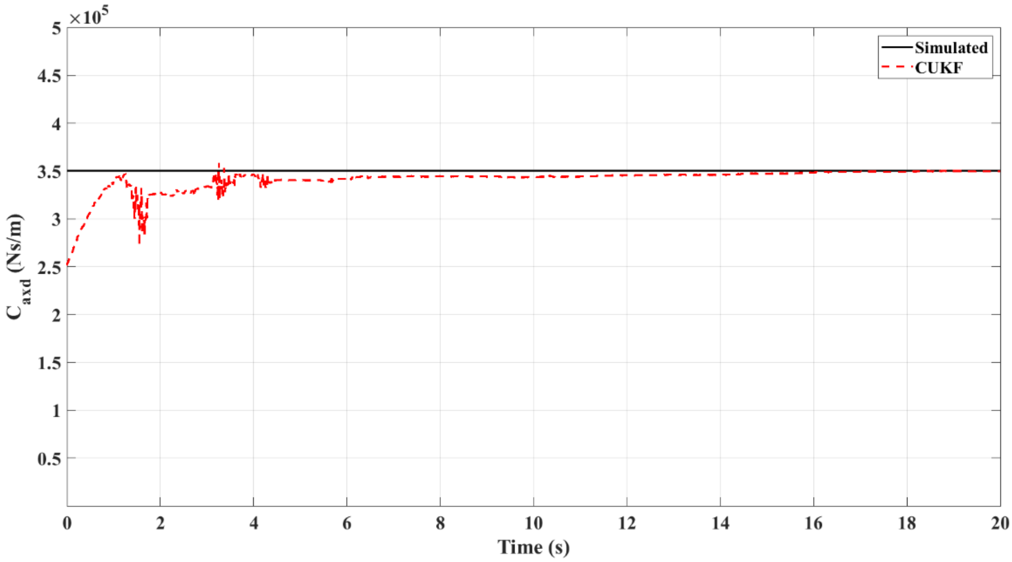

Figure 4.26. Anti-yaw damping C_{axd} (no fault condition – five sensors configuration with anti-yaw stiffness estimation).

This result demonstrates the suitability of the CUKF to estimate the anti-yaw damping converging to the desired value thanks to the application of state constraints, which allow taking into account the physical operative limits of the anti-yaw suspension components.

The estimated anti-yaw stiffness is compared with the simulated one (K_{axd} = 323400 N/m). The CUKF is able to estimate the anti-yaw stiffness with excellent estimation quality, as shown in Figure 4.27. The employed constrained estimator is able to improve the estimation convergence.

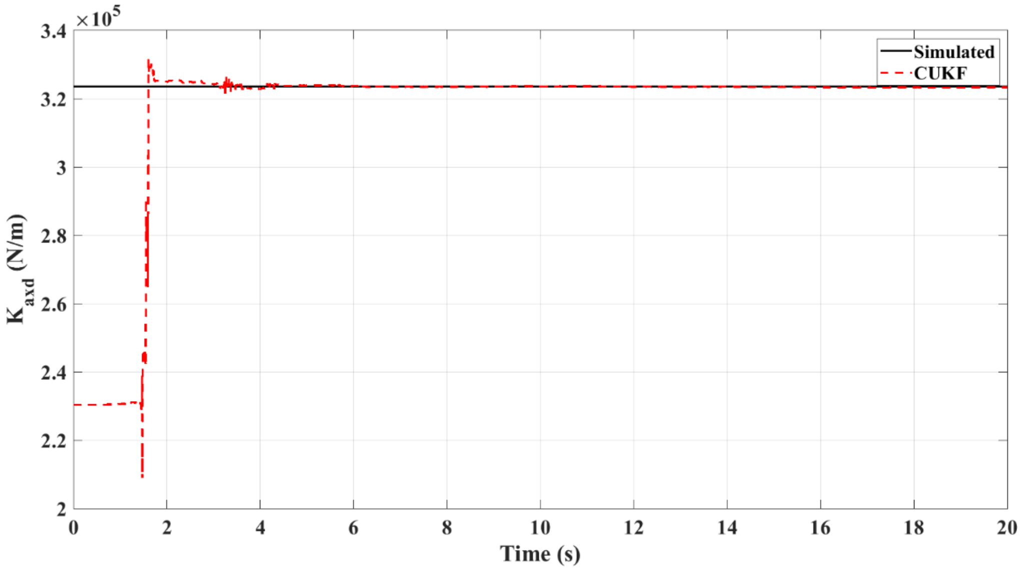

Figure 4.27. Anti-yaw stiffness K_{axd} (no fault condition – five sensors configuration with anti-yaw stiffness estimation).

Estimated measurements are similar to those shown in Figure 4.3, 4.4, 4.5, 4.6 and 4.7 of Section 4.1.1, confirming the capability of the CUKF to estimate measurements provided by sensors. A reliable estimation of the measurements, strongly related to the system state variables, indicates the capability of the CUKF to estimate the states correctly.

Estimated wheel-rail contact interactions are similar to those shown in Figure 4.8 of Section 4.1.1, demonstrating the validity of the RWM technique.
The CUKF estimates the lateral wheel-rail contact interactions, avoiding a priori knowledge of the track conditions and a specific wheel-rail contact model by applying the RWM, which is functional for monitoring anti-yaw suspension components.

The NRMSE values reported in Table 4.5 are near zero confirming the good estimation quality of the proposed estimation technique.

Table 4.5. NRMSE values (no fault condition – five sensors configuration with estimation of K_{axd}).

Variable name	***NRMSE***
$\ddot{y}_{bd}$	0.0017
$\ddot{y}_{b}$	7.89×10^{-4}
$\ddot{y}_{w1}$	5.15×10^{-4}
$\ddot{y}_{w2}$	0.0013
$\dot{\psi}_{b}$	2.72×10^{-4}
F_{yw1}	0.0401
F_{yw2}	0.0702
M_{w1}	0.0828
M_{w2}	0.1377
C_{axd}	0.0371
K_{axd}	0.0675

Figure 4.28 shows the comparison between the estimated anti-yaw damping and the linearized damping value related to the anti-yaw dampers in fault condition (C_{axd} = 140000 Ns/m).
In this test, the capability of the CUKF to perceive a change in the operative conditions of anti-yaw suspension components, especially of the anti-yaw dampers, is verified.

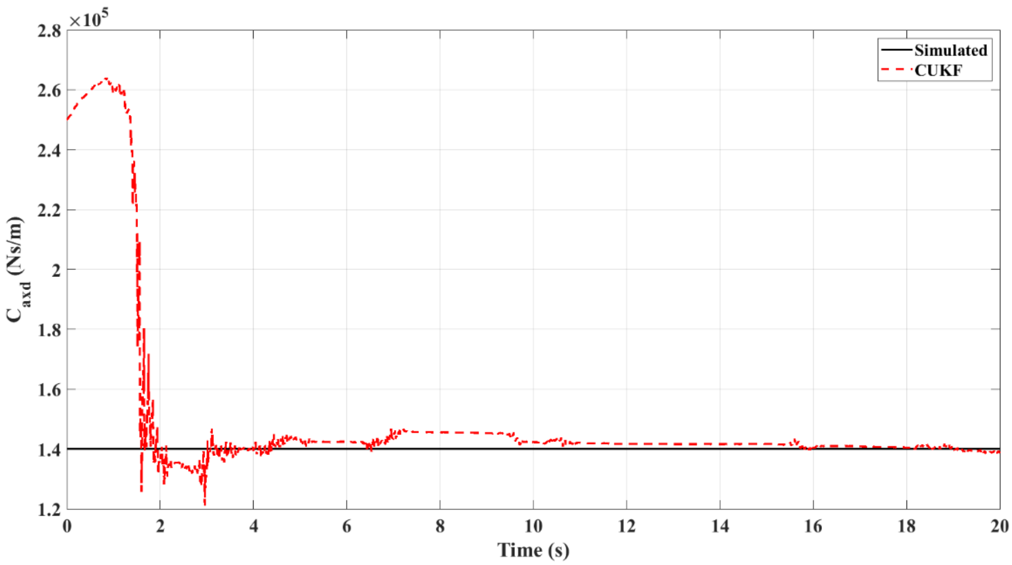

Figure 4.28. Anti-yaw damping C_{axd} (fault condition – five sensors configuration with anti-yaw stiffness estimation).

The CUKF is able to identify a fault affecting the anti-yaw dampers demonstrating its suitability to monitor the degradation of anti-yaw suspension components.

Simultaneously, the estimation of the anti-yaw stiffness (K_{axd} = 323400 N/m) is made by the CUKF, as shown in Figure 4.29.

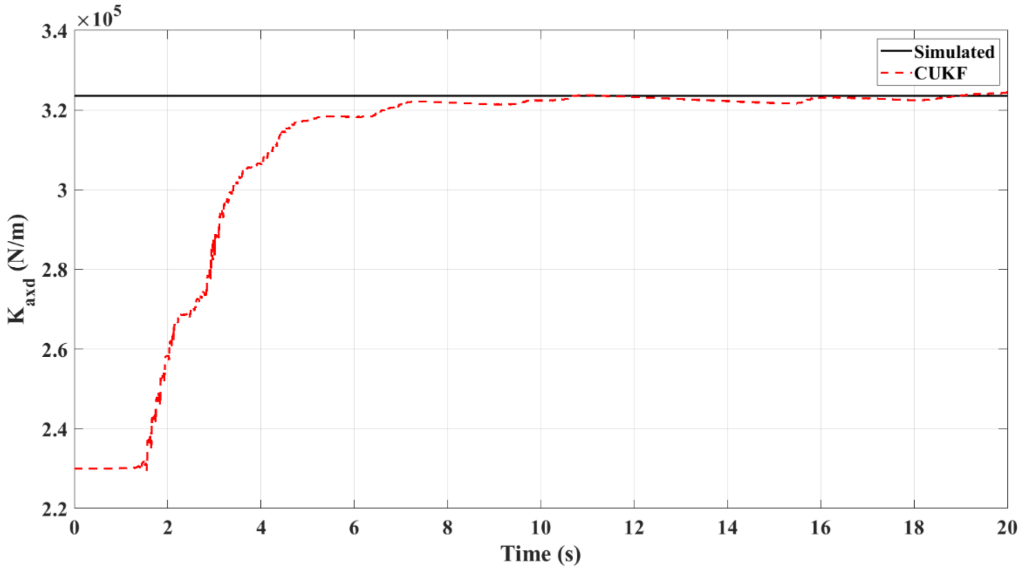

Figure 4.29. Anti-yaw stiffness K_{axd} (fault condition – five sensors configuration with anti-yaw stiffness estimation).

Estimated measurements are similar to those shown in Figures 4.10, 4.11, 4.12, 4.13, and 4.14 of Section 4.1.1, confirming the capability of the CUKF to distinguish the operative conditions of the anti-yaw dampers and springs. The degradation of anti-yaw dampers causes a change in the dynamical behaviour of the railway vehicle detected by the CUKF through the correct estimation of the measurements.

Estimated wheel-rail contact interactions are similar to those shown in Figure 4.15 of Section 4.1.1, demonstrating the validity of the RWM technique. The CUKF estimates the lateral wheel-rail contact interactions, avoiding a priori knowledge of the track conditions and a specific wheel-rail contact model by applying the RWM, which is functional for monitoring anti-yaw suspension components.

The NRMSE values reported in Table 4.6 are near zero confirming the good estimation quality of the proposed estimation technique.

Table 4.6. NRMSE values (fault condition – five sensors configuration with estimation of K_{axd}).

Variable name	***NRMSE***
$\ddot{y}_{bd}$	0.0011
$\ddot{y}_{b}$	0.0022
$\ddot{y}_{w1}$	0.001
$\ddot{y}_{w2}$	0.0023
$\dot{\psi}_{b}$	6.37×10^{-4}
F_{yw1}	0.0528
F_{yw2}	0.1067
M_{w1}	0.0925
M_{w2}	0.3674
C_{axd}	0.1945
K_{axd}	0.0822

Overall, the obtained results confirm the suitability of the CUKF as a tool to estimate the parameters of anti-yaw suspension components by aiming at the condition monitoring of railway vehicles.

4.2. Vehicle and tire-road condition monitoring

4.2.1. Estimation of sideslip angle and left and right lateral tire-road friction coefficients

Estimations provided by the proposed model-based monitoring technique based on the EKF have been compared with simulated data obtained through a multibody vehicle developed in the ADAMS Car environment [121].

The sideslip angle with left and right lateral tire-road friction coefficients and measurements estimated by the EKF are compared with the ADAMS Car vehicle model.
Realistic measurements have been obtained by adding Gaussian white noise to the simulated measurements.

Three manoeuvres, described in Table 4.7, have been selected for assessing the proposed model-based estimator.

Table 4.7. Details and investigative purposes of each simulated manoeuvres.

Simulated manoeuvres	Test surface	Purpose
Step steer – case 1	Constant dry roadbed	Investigate the friction-sensing ability of the estimator. During the manoeuvre, lateral forces increase gradually, eventually reaching saturation.
Step steer – case 2	Each wheel is subjected to the same values of lateral tire-road friction coefficients. These latter change values every 10 seconds.	Determinate the estimator response to a quick change in the road surface. Friction coefficients are varied on three different levels.
Step steer – case 3	Each wheel is subjected to different values of lateral tire-road friction coefficients. These latter change values every 10 seconds.	Validate the tire-road condition monitoring under little friction variations. Each wheel is exposed to a different surface (distinct values of latera tire-road friction coefficients for the left and right tires).

Figure 4.30 provides the indicative physical representation of each proposed scenario.

The first simulation (Figure 4.30a) has been performed by imposing a constant profile of both lateral tire-road friction coefficients, without variations over time. The road conditions do not change during the manoeuvre.

The second simulation (Figure 4.30b) has been performed by imposing a descending friction profile equal to each wheel.

The third simulation (Figure 4.30b) has been performed by imposing a differentiated descending friction profile on the two sides of the car.

Therefore, through scenarios represented in Figures 4.30b and 4.30c, it is possible to observe changes in lateral tire-road friction coefficients depending on the time and occurring at successive time intervals.

In Figure 4.30, each colour represents a value of the lateral tire-road friction coefficient. The black colour corresponds to a high friction value; the green colour corresponds to a medium friction value; the violet colour corresponds to a low friction value.

During simulations, the vehicle has been set on an equilibrium point with constant longitudinal velocity.

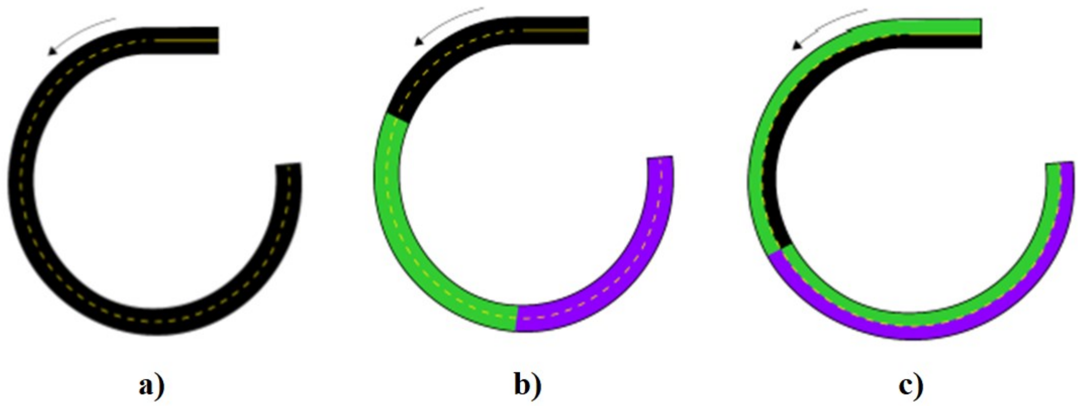

Figure 4.30. Schematic road layout coupled with the representation of time-dependent changes of lateral tire-road friction coefficients.

4.2.1.1. Step Steer Manoeuvre: case 1

The chosen manoeuvre for the first simulation is a step steer manoeuvre. At t=1 s, a variation in the steering angle of 100 degrees, in 0.1 s, has been imposed. The manoeuvre (Figure 4.30a) has been carried out on a dry road, and road conditions do not vary over time. The longitudinal speed has been set constant at 50 km/h.

Estimations of the sideslip angle and measurements constituted of the lateral acceleration and the yaw rate obtained by the EKF are shown in Figure 4.31. The EKF is able to estimate the sideslip angle correctly in the first proposed scenario.

The correct estimation of measurements reflects the capability of the proposed model-based approach of managing state variables which compose measurements.

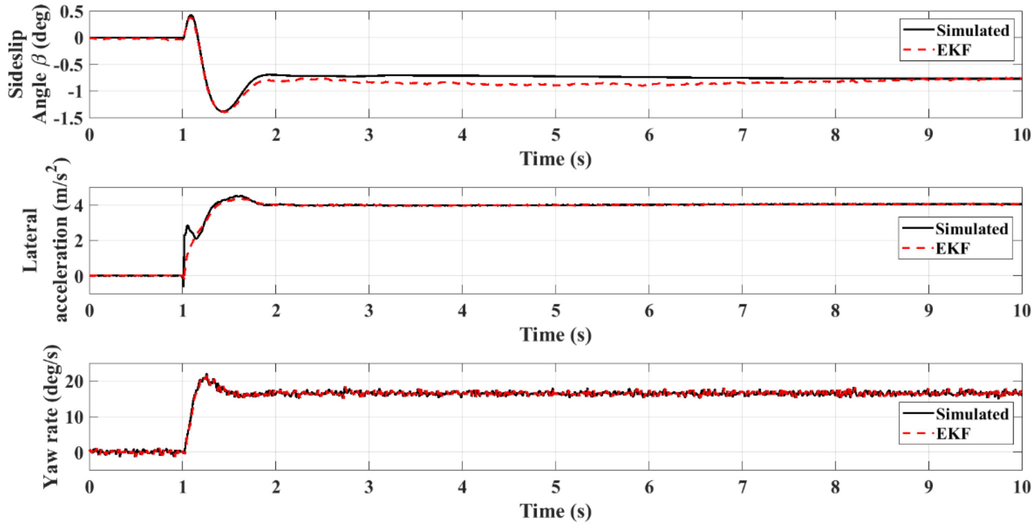

Figure 4.31. Sideslip angle β and measurements a_y, r (step steer manoeuvre: case 1).

Figure 4.32 shows the estimation of left and right lateral tire-road friction coefficients. The steady-state behaviour of both friction coefficients reveals the suitability of the EKF for estimating constant and equal values of previously mentioned friction coefficients as expected for the first scenario.

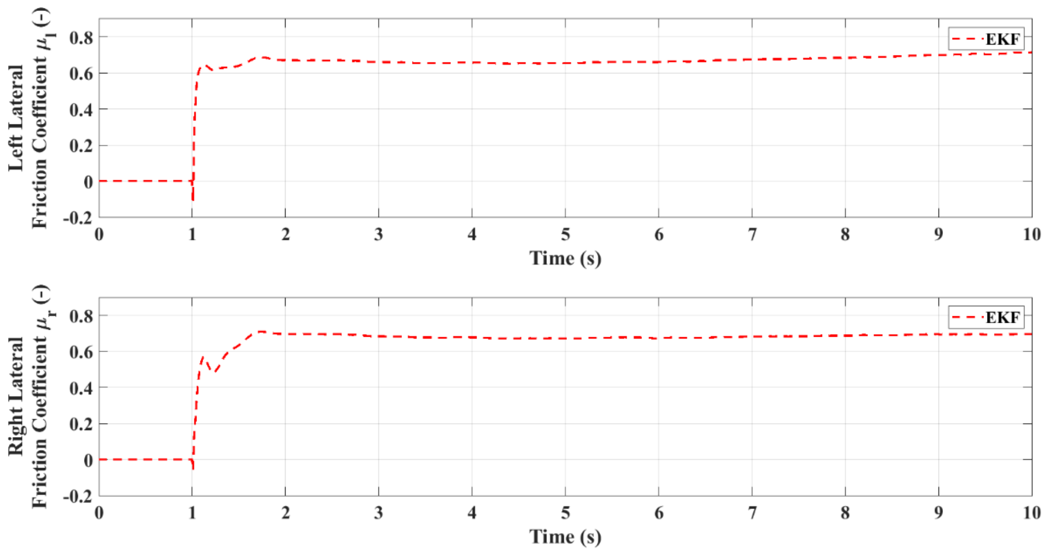

Figure 4.32. Left and right lateral tire-road friction coefficients μ_l, μ_r (step steer manoeuvre: case 1).

The estimated lateral tire-road friction coefficients allow for estimating lateral tire-road forces through the EKF, by adapting the adopted four parameters Pacejka Magic Formula included in the estimator design model.

The EKF provides reliable estimations of lateral tire-road forces, as represented in Figure 4.33, confirming its suitability for monitoring tire-road conditions.

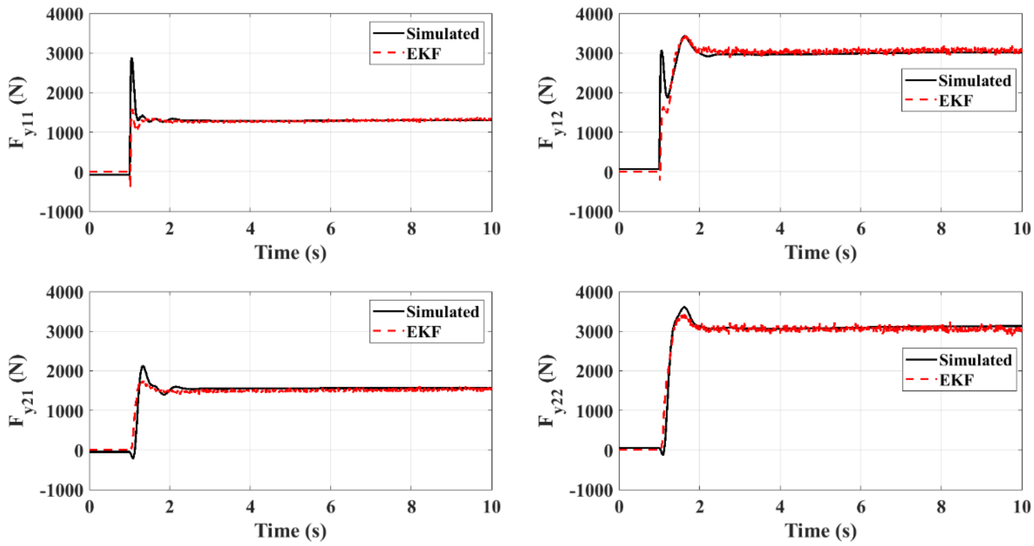

Figure 4.33. Lateral tire-road forces F_{y11}, F_{y12}, F_{y21}, F_{y22} (step steer manoeuvre: case 1).

NRMSE values are reported in Table 4.8 for evaluating the estimation quality.

Table 4.8. NRMSE values (step steer manoeuvre: case 1).

Variable name	***NRMSE***
β	0.0555
a_y	0.0300
r	0.0366
F_{y11}	0.0502
F_{y12}	0.0591
F_{y21}	0.0509
F_{y22}	0.0353

NRMSE values are close to zero, confirming a good estimation quality provided by the proposed EKF.

4.2.1.2. Step Steer Manoeuvre: case 2

The chosen manoeuvre for the second simulation is a step steer manoeuvre. At t=1 s, a variation in the steering angle of 100 degrees, in 0.5 s, has been imposed. The manoeuvre (Figure 4.30b) has been carried out by simulating different road conditions (dry asphalt, wet asphalt, off-road, etc.) through a descent variation of lateral tire-road friction coefficients over time. Transitions of friction coefficients occur during successive equal time intervals of 10 s. The longitudinal speed has been set constant at 60 km/h.

Estimations of the sideslip angle and measurements obtained by the EKF are shown in Figure 4.34. The EKF is able to capture the sideslip angle correctly in the second proposed scenario, in which the frictional behaviour of the road changes globally in three different periods. Variations in the sideslip angle trend can be observed at the same time instants in which the lateral tire-road friction coefficient changes.

The correct estimation of measurements reflects the capability of the proposed model-based approach of managing state variables which compose measurements.

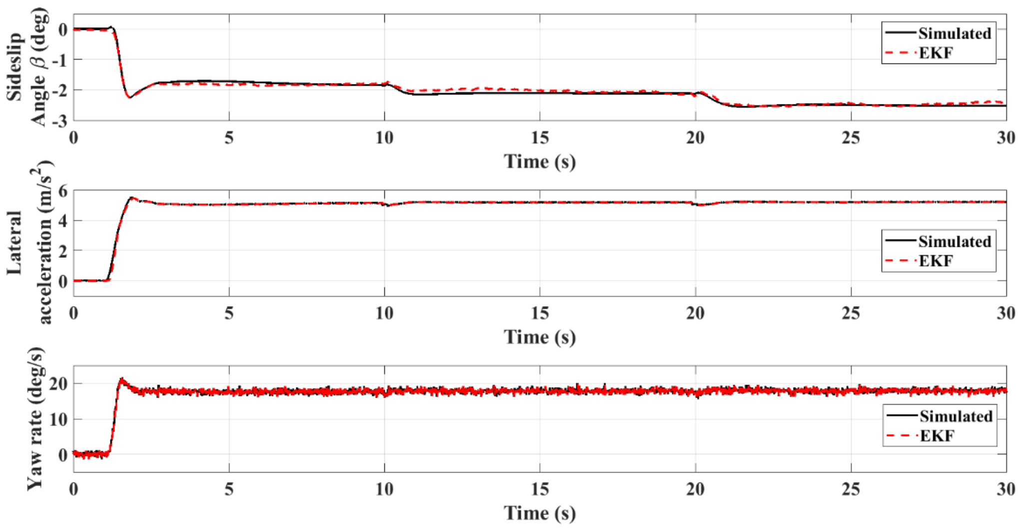

Figure 4.34. Sideslip angle β and measurements a_y, r (step steer manoeuvre: case 2).

Figure 4.35 shows the estimation of left and right lateral tire-road friction coefficients.

Globally, the estimated values of both friction coefficients are similar, as expected for the second scenario. Furthermore, the EKF demonstrates its capability to detect friction variations every 10 s.

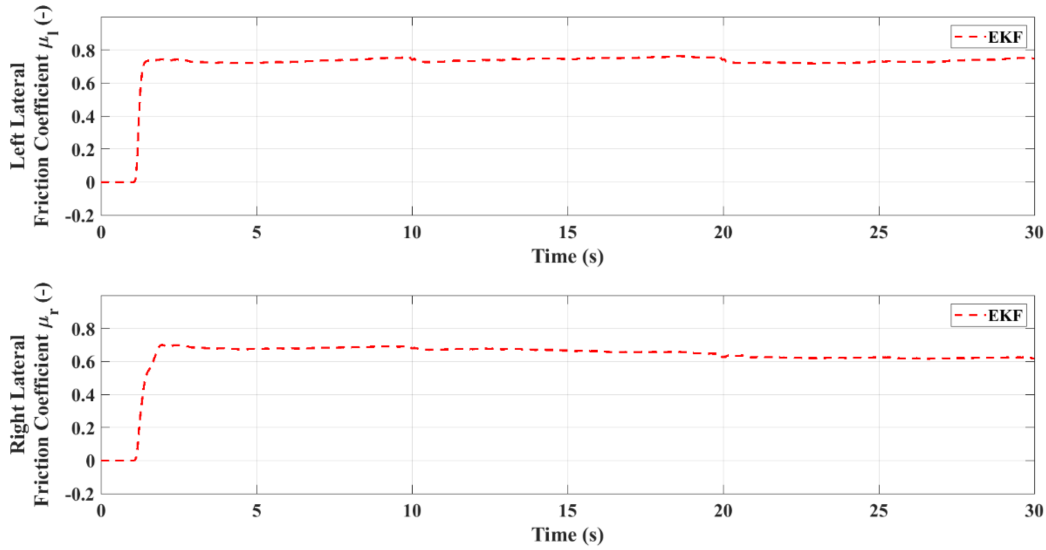

Figure 4.35. Left and right lateral tire-road friction coefficients μ_l, μ_r (step steer manoeuvre: case 2).

Trends of lateral tire-road forces are correctly estimated through the EKF, as shown in Figure 10, despite a slight underestimation in F_{y21}. The good perceiving of lateral tire-road friction coefficients is fundamental for the EKF to obtain a reliable estimation of lateral tire-road forces based on the adopted Pacejka Magic Formula.

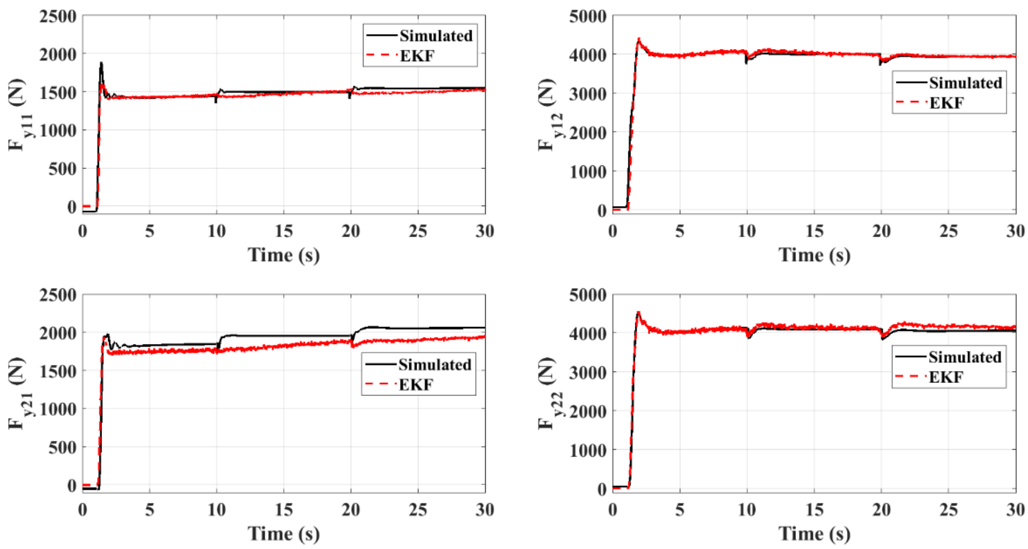

Figure 4.36. Lateral tire-road forces F_{y11}, F_{y12}, F_{y21}, F_{y22} (step steer manoeuvre: case 2).

NRMSE values are reported in Table 4.9 for evaluating the estimation quality.

Table 4.9. NRMSE values (step steer manoeuvre: case 2).

Variable name	***NRMSE***
β	0.0285
a_y	0.0095
r	0.0362
F_{y11}	0.0286
F_{y12}	0.0235
F_{y21}	0.0624
F_{y22}	0.0198

NRMSE values are close to zero, confirming a good estimation quality provided by the proposed EKF.

4.2.1.3. Step Steer Manoeuvre: case 3

The chosen manoeuvre for the third simulation is a step steer manoeuvre. At t=1 s, a variation in the steering angle of 100 degrees, in 0.5 s, has been imposed. The manoeuvre (Figure 4.30c) has been carried out by simulating different road conditions through a descent variation of lateral tire-road friction coefficients over time. Differently, from the second simulation, in the third one, left and right lateral tire-road friction coefficients vary at both sides of the vehicle by differentiating left and right frictional behaviour. Transitions of friction coefficients occur during successive equal time intervals of 10 s. The longitudinal speed has been set constant at 60 km/h.

Estimations of the sideslip angle and measurements obtained by the EKF are shown in Figure 4.37. The EKF is able to capture the sideslip angle correctly in the third proposed scenario, in which the frictional behaviour of the road changes in two different periods. Variations in the sideslip angle trend can be observed at the same time instants in which the lateral tire-road friction coefficient changes.

The correct estimation of measurements reflects the capability of the proposed model-based approach of managing state variables which compose measurements.

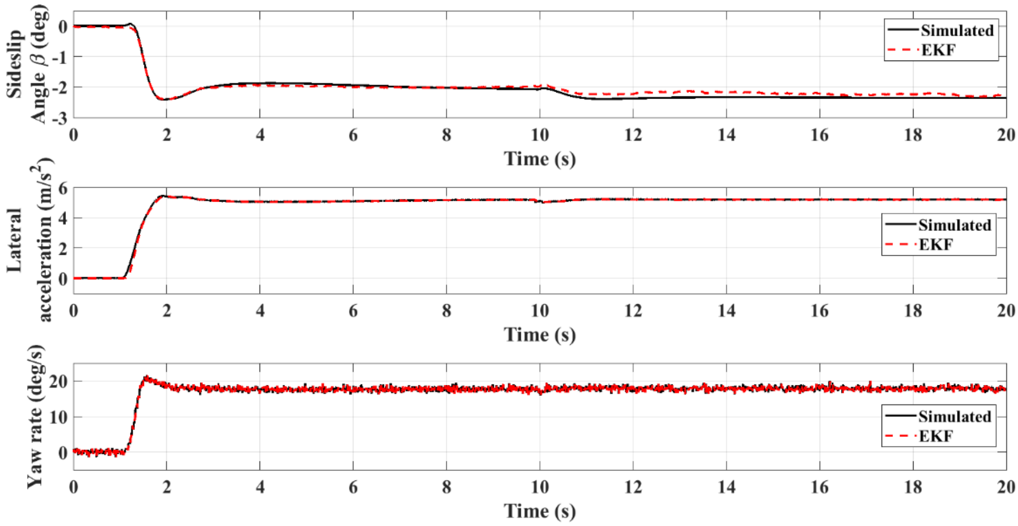

Figure 4.37. Sideslip angle β and measurements a_y, r (step steer manoeuvre: case 3).

Figure 4.38 shows the estimation of left and right lateral tire-road friction coefficients.
The estimated values of left and right lateral tire-road friction coefficients are different, as expected for the second scenario, confirming the capability of the EKF to identify nonidentical frictional behaviours at both sides of the vehicle. Furthermore, the EKF demonstrates its potential for detecting friction variations every 10 s.

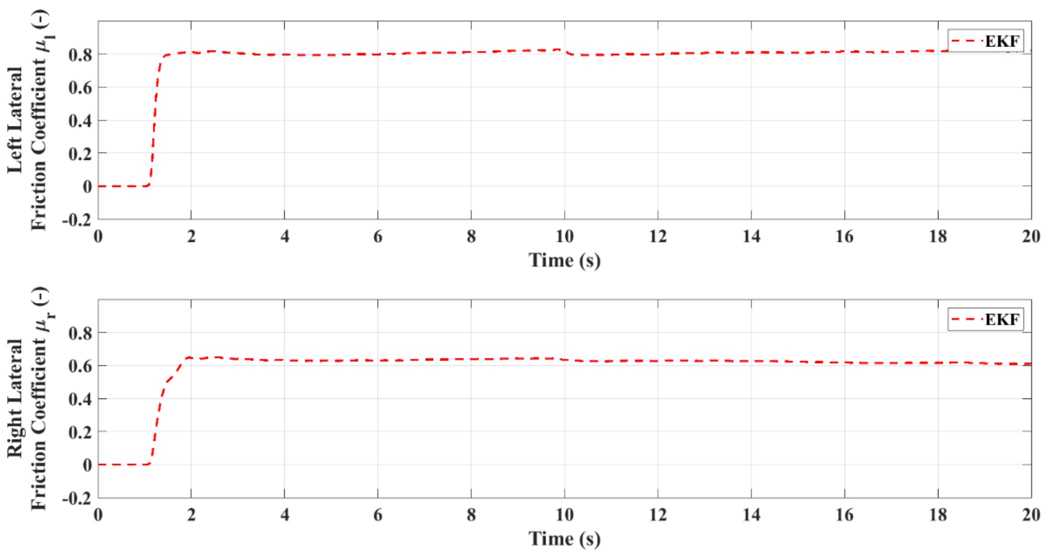

Figure 4.38. Left and right lateral tire-road friction coefficients μ_l, μ_r (step steer manoeuvre: case 3).

Trends of lateral tire-road forces are correctly estimated through the EKF, as shown in Figure 4.39, despite a slight underestimation in F_{y21}. The good perceiving of lateral tire-road friction coefficients is fundamental for the EKF to obtain a reliable estimation of lateral tire-road forces based on the adopted Pacejka Magic Formula.

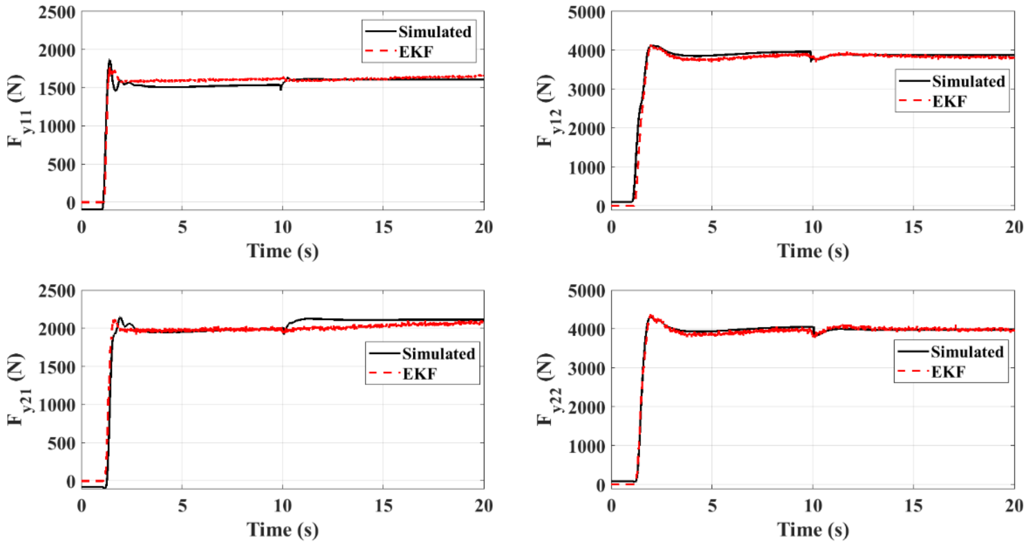

Figure 4.39. Lateral tire-road forces F_{y11}, F_{y12}, F_{y21}, F_{y22} (step steer manoeuvre: case 3).

NRMSE values are reported in Table 4.10 for evaluating the estimation quality.

Table 4.10. NRMSE values (step steer manoeuvre: case 3).

Variable name	***NRMSE***
β	0.0422
a_y	0.0107
r	0.0362
F_{y11}	0.0361
F_{y12}	0.0339
F_{y21}	0.0405
F_{y22}	0.0159

NRMSE values are close to zero, confirming a good estimation quality provided by the proposed EKF. The presented results demonstrate the suitability of the proposed technique for monitoring tire-road conditions with the possibility of perceiving the possible different frictional behaviour at both sides of the vehicle and estimating the sideslip angle correctly for managing vehicle performances.

4.2.2. Estimation of sideslip angle and lateral tire-road friction coefficient with no interaction modelling

The capability of the EKF to estimate the sideslip angle and the lateral tire-road friction coefficient for vehicle condition monitoring has been assessed by comparing estimated results with ones obtained from the dynamical response of a detailed and complete Multibody vehicle model developed in ADAMS Car [121], acknowledged as a benchmark software for the simulation of vehicle dynamics from the scientific community. The EKF has been developed in Matlab/Simulink environment [133].

The chosen manoeuvre is step steering. The vehicle runs with a constant longitudinal velocity of 50 Km/h on a straight road for 1 s. After 1 s, an instant left turn, consisting of a variation of the steering angle δ from 0 to 100°, is made.

The steering angle δ is transferred to the wheels of the front axle, assuming a steering ratio of 1/27.6.

The lateral tire-road friction coefficient has been set at 0.7 in the ADAMS environment.

The performances of the EKF have been tested with neat and noisy measurements.

Figure 4.40 shows the estimation of the sideslip angle and measurements constituted by lateral acceleration and yaw rate in a not noisy condition.

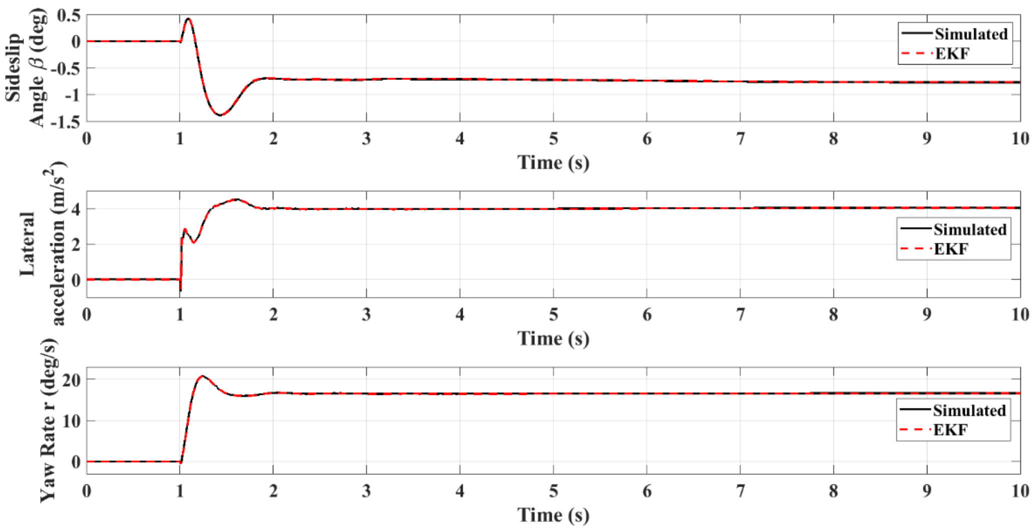

Figure 4.40. Sideslip angle β and measurements a_y, r – neat measurements.

The EKF is able to correctly estimate the sideslip angle, making it functional for the employment in control systems as a feedback variable.

Furthermore, the estimated measurements are according perfectly with the simulated ones. Estimated measurements are connected strictly with state variables of the estimator design model. Therefore, the excellent estimation quality previously displayed is reflected in state variables.

The comparison between estimated lateral friction coefficient and forces with the simulated ones is shown in Figure 4.41.
A good matching can be observed demonstrating the suitability of the employed EKF for tire-road condition monitoring with a priori no knowledge on a specific tire modelling technique. Furthermore, observing the lateral tire-road forces, it is possible to appreciate the capability of variables K_1 and K_2 to correctly capture the vehicle dynamical behavior dependent on the drift angles of wheels.

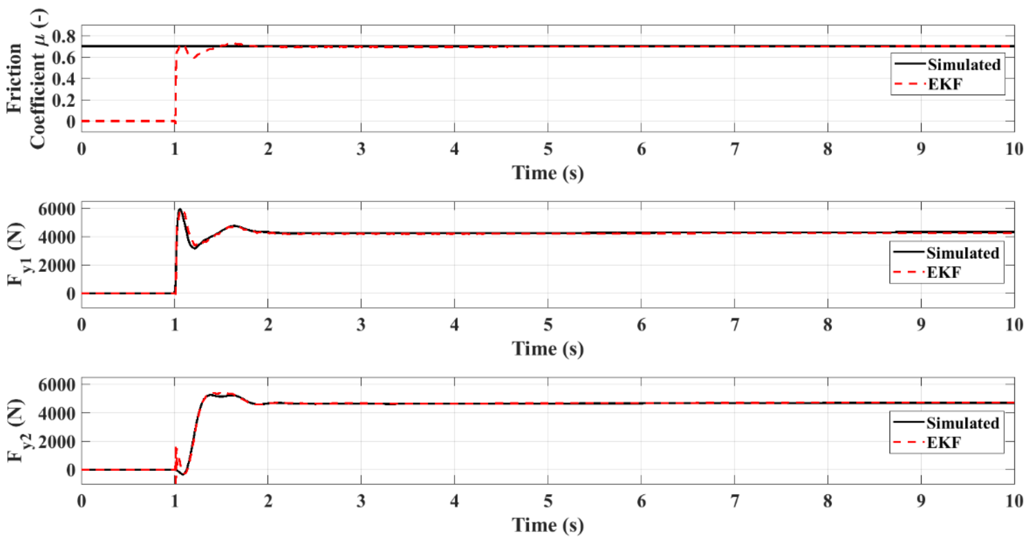

Figure 4.41. Lateral tire-road friction coefficient μ and lateral forces F_{y1}, F_{y2} – neat measurements.

NRMSE values are reported in Table 4.11 for evaluating the estimation quality.

Table 4.11. NRMSE values (neat measurements).

Variable name	*NRMSE*
β	0.0022
a_y	0.0046
r	3.634×10^{-4}
μ	0.3185
F_{y1}	0.0151
F_{y2}	0.0130

NRMSE values are close to zero, confirming a good estimation quality provided by the proposed EKF. If the NRMSE value of μ is evaluated, avoiding the time window from 0 s to 1 s, where the transient is observable, NRMSE is lower by one order of magnitude.

In Figure 4.42, the results concerning the comparison between the estimated sideslip angle and measurements affected by a noisy source are shown.

These results demonstrate the reliability of the EKF to identify with a good estimation quality the desired variables in noisy measurements presence.

Furthermore, a filtering action can be observed in the yaw rate estimation.

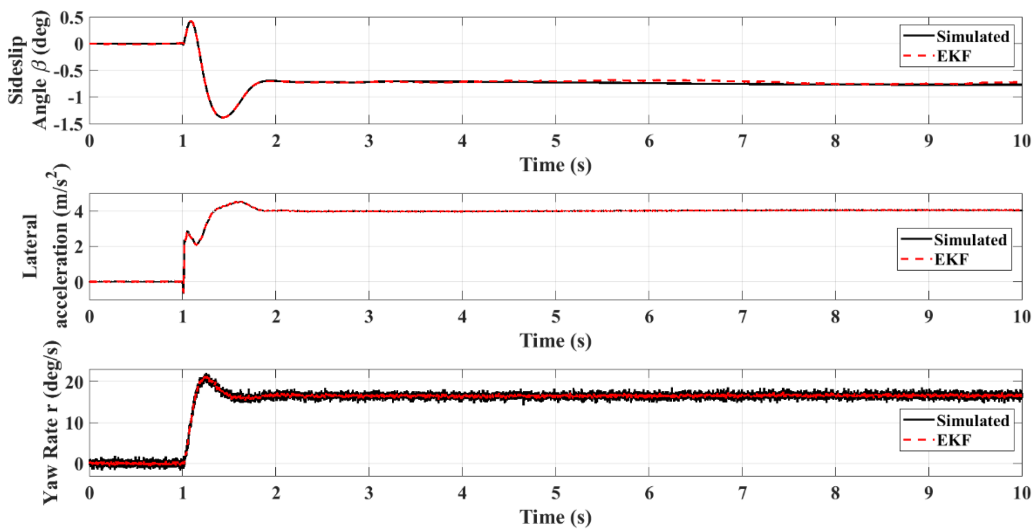

Figure 4.42. Sideslip angle β and measurements a_y, r – noisy measurements.

Finally, Figure 4.43 confirms the suitability of the proposed approach for tire-road condition monitoring through a good matching between the estimated lateral friction and forces with the simulated ones even in a noisy environment.

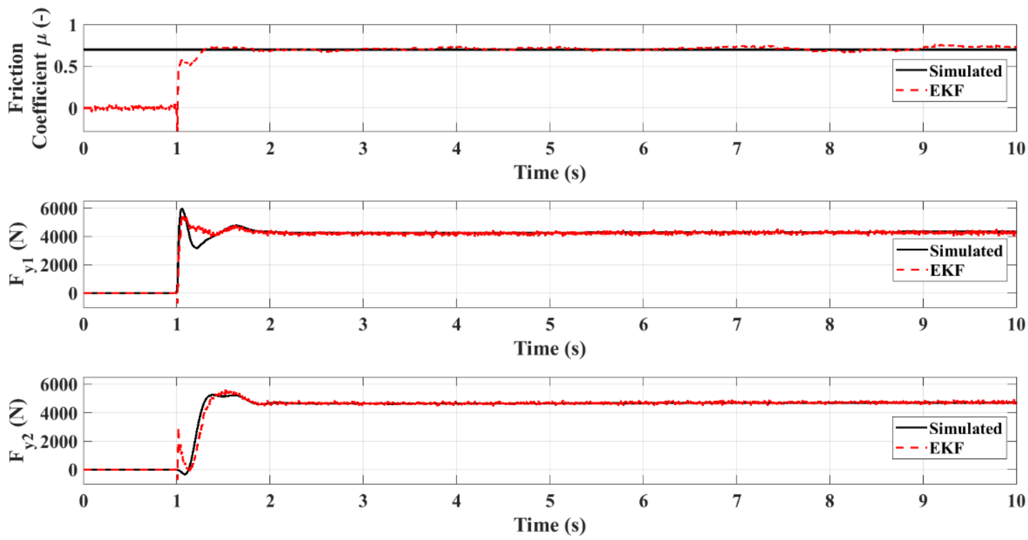

Figure 4.43. Lateral tire-road friction coefficient μ and lateral forces F_{y1}, F_{y2} – noisy measurements.

NRMSE values are reported in Table 4.12 for evaluating the estimation quality.

Table 4.12. NRMSE values (noisy measurements).

Variable name	***NRMSE***
β	0.0149
a_y	0.0033
r	0.0263
μ	0.3225
F_{y1}	0.0341
F_{y2}	0.0371

NRMSE values are close to zero, confirming a good estimation quality provided by the proposed EKF. If the NRMSE value of μ is evaluated, avoiding the time window from 0 s to 1 s, where the transient is observable, NRMSE is lower by one order of magnitude.

The presented results demonstrate the suitability of the proposed technique for monitoring tire-road conditions without specific modelling of tires and for estimating the sideslip angle correctly for managing vehicle performances.

4.3. Estimation of the instantaneous friction coefficients of sliding isolators subjected to bi-directional orbits

4.3.1. Method validation through numerical simulations

The effectiveness of the CUKF to estimate the friction coefficient at either sliding surface of CSS isolators is validated through force-displacement data obtained from bi-directional thermo-mechanical FE analyses.

In particular, it is demonstrated hereafter that the CUKF can estimate the instantaneous values of the friction coefficients $\mu_1 = \mu_1(t)$ and $\mu_2 = \mu_2(t)$ processing the following time-histories input data:

- the displacement histories imposed to the CSS in the longitudinal, d_x, and transversal, d_y, directions;
- the applied axial load N;
- the longitudinal and transversal components of the reaction force of the isolator, F_x and F_y.

Additional input data are the geometric parameters of the CSS: the radii of curvature R_1 and R_2 of the sliding surfaces, and the thickness h of the pivot element (Figure 1.3).

Three different isolator layouts, namely CSS-1, CSS-2, and CSS-3, have been defined by varying radii of curvature and frictional properties of the two sliding surfaces as in Table 4.13 to cover different possible real scenarios.

Table 4.13. Characteristic parameters of the CSSs considered in FEM analyses.

	R_1 [mm]	R_2 [mm]	h [mm]	N [kN]	$p_{1,avg}$ [MPa]	$p_{2,avg}$ [MPa]	$\mu_{1,Tamb}$ [-]	$\mu_{2,Tamb}$ [-]	β_1 [-]	β_2 [-]
CSS-1	1650	530	186	4500	18.3	27.6	0.110	0.005	0.0027	0.0000
CSS-2	770	770	55	100	35.4	35.4	0.110	0.110	0.0027	0.0027
CSS-3	770	770	55	100	35.4	35.4	0.070	0.085	0.0050	0.0050

R_1, R_2 = radius of curvature ; h = height of the pivot element; N = design axial load; $p_{1,avg}$, $p_{2,avg}$ = average contact pressure on the sliding pad; $\mu_{1,Tamb}$, $\mu_{2,Tamb}$ = coefficient of friction at ambient temperature; β_1, β_2 = temperature parameter of the friction coefficient, Eq. (4.3)

The CSS-1 layout, represented in Figure 1.3a and characterized by $R_1 > R_2$, and $\mu_1 > \mu_2$, provides a primary dissipative sliding surface to accommodate the lateral displacement, and a secondary sliding surface operating as a rotational hinge.

The CSS-2 layout represents a DCSS with two identical primary sliding surfaces, i.e., $R_1 = R_2$, and $\mu_1 = \mu_2$, as shown in Figure 1.3b.

Eventually, the CSS-3 layout, featuring $R_1 = R_2$, and $\mu_1 = 0.8 \cdot \mu_2$, represents a DCSS device with different (20%) friction coefficients at the sliding surfaces as it may result from standard production variability of the sliding material [73].

In particular, CSS-2, and CSS-3 correspond to two real small-scale prototypes that were investigated in shaking-table tests [68].

Three-dimensional models of the isolators have been created in the FE software program ABAQUS v. 2019 [118], by using both coupled thermal-mechanical hexaedrical and wedge 3D linear elements, type C3D8T and C3D6T respectively, with four degrees of freedom at each node (the displacement components in three directions and temperature).

Further details about this modelling approach, developed by the authors in a previous study, can be found in [134]. All movements have been constrained at the lower surface of the bottom plate while an “8-shaped” horizontal displacement orbit has been imposed to the top plate according to the two sinusoidal components:

$$\begin{cases} d_x(t) = A_x \sin(n_x \, \omega \, t) \\ d_y(t) = A_y \sin(n_y \, \omega \, t) \end{cases} \tag{4.1}$$

where d_x and d_y denote the displacement of the bearing in x and y direction at time t, $A_x = 170$ mm and $A_y = 170$ mm are the displacement amplitudes in the two directions, $n_x = 1$ and

$n_y = 2$ are two parameters used to adjust the circular frequency of the motion, $\omega = \sqrt{g/(R_1 + R_2 - h)}$ is the vibration frequency of the isolator, and g is the acceleration of gravity.

It is worth noting that, among possible bi-directional orbits, the "8-shaped" has been selected since it was proven to maximize the degradation of the effective damping of the CSS due to the frictional heating [135].

A main characteristic of sliding isolators, such as CSSs and DCSSs, is that the seismic energy dissipated through friction mechanisms is converted into heat, thereby producing an increase in temperature at the sliding surfaces, which in turns affects the coefficient in friction.

Such variation of the coefficient of friction due to the heat-generated temperature rise is accounted for in the simulation. Typical mechanical and thermal properties have been assigned to the materials as per Table 4.14 [134].

Table 4.14. Material properties.

Component	Material	*E* [MPa]	ν [-]	*k* [W/(m K)]	*c* [J/(kg K)]
top/bottom plate	carbon steel	2.09×10^5	0.30	53.7	4.9×10^5
top/bottom mating surf.	stainless steel	1.96×10^5	0.30	16.0	5.0×10^5
pivot	stainless steel	1.96×10^5	0.30	16.0	5.0×10^5
top/bottom sliding pad	friction polymer	8.00×10^2	0.45	0.65	1.1×10^6

E = elastic modulus; ν = Poisson ratio; *k* = thermal conductivity; *c* = specific heat

The heat generated at each sliding surface has been introduced into the model through a heat source spread over the contact area of the sliding pad, supplying a heat flux with local intensity q_1 and q_2 at the top and bottom sliding surfaces, respectively:

$$\begin{cases} q_1 = \mu_1 \, p_1 \, v_1 \\ q_2 = \mu_2 \, p_2 \, v_2 \end{cases} \tag{4.2}$$

where $v_1 = \sqrt{v_{1,x}^2 + v_{1,y}^2}$ and $v_2 = \sqrt{v_{2,x}^2 + v_{2,y}^2}$ are the moduli of the relative sliding velocities at the two surfaces. Equation (4.2) assumes that the whole mechanical work performed by the external forces to maintain the motion of the slider is converted into heat.

It is further assumed that almost the whole totality (99%) of the heat flux is directed inwards the steel plate and only 1% inwards the sliding pad; this assumption is justified by the different thermal conductivity of the relevant materials and its validity was confirmed by a detailed thermal analysis [134].

To reduce the calculation burden, the dependence of the coefficient of friction on the local contact pressure and the sliding velocity has been disregarded, and a simple temperature-dependent formulation has been assumed [134]:

$$\begin{cases} \mu_1(T) = \mu_{1,Tamb}\exp\left[-\beta_1\,(T_1 - T_{1,amb})\right] \\ \mu_2(T) = \mu_{2,Tamb}\exp\left[-\beta_2\,(T_2 - T_{2,amb})\right] \end{cases} \tag{4.3}$$

where $\mu_{1,Tamb}$ and $\mu_{2,Tamb}$ are the initial values of the coefficients of friction at the ambient temperature $T_{1,amb} = T_{2,amb} = 25$ °C; T_1 and T_2 are the temperatures of the sliding surfaces; and β_1 and β_2 are two coefficients that regulate the rate of decay of friction with the increase of temperature. All parameters have been assigned according to Table 4.13.

The boundary conditions for the thermal analysis are: (a) nodal temperatures of the flat surfaces of upper and lower plates kept at a constant temperature $T_{amb} = 25$ °C; (b) other lateral surfaces of the bearing assumed to be adiabatic; (c) local frictional heat fluxes generated at the contact areas between the pads and the concave surfaces.

At each time step, current nodal temperatures are used by the software to update the local values of the coefficients of friction μ_1 and μ_2, and relevant heat fluxes q_1 and q_2 through Equation (4.3), and Equation (4.2), respectively.

The heat balance equation is numerically integrated providing the temperature distribution within the bearing. Two time-histories have been extracted from the analysis: (1) the average nodal temperature histories at thw two sliding surfaces, $T_{1,avg}$ and $T_{2,avg}$, and (2) the reaction force histories in the two horizontal directions, F_x and F_y.

The first history is used to calculate, through Equation (13), the average instantaneous values of the coefficients of friction μ_1 and μ_2, and the effective coefficient of friction μ_{eff} of the CSS isolator [136]:

$$\begin{cases} \mu_1 = \mu_1(T_{1,avg}) \\ \mu_2 = \mu_2(T_{2,avg}) \\ \mu_{eff} = \dfrac{\mu_1(T_{1,avg})\,R_1 + \mu_2(T_{2,avg})\,R_2}{R_1 + R_2} \end{cases} \tag{4.4}$$

where $T_{1,avg} = T_{1,avg}(t)$, and $T_{2,avg} = T_{2,avg}(t)$.

It is worth noting that, since temperature time-histories at the two sliding pads are usually unknown, only the effective friction coefficient (μ_{eff}) can be usually estimated from basic force-displacement data recorded during isolators' testing:

$$\begin{cases} \mu_{eff} = \left(\sqrt{{F_{\mu_x}}^2 + {F_{\mu_y}}^2}\right)/N \\ F_{\mu_x} = F - (N\,d_x)/R_{eff} \\ F_{\mu_y} = F - (N\,d_y)/R_{eff} \end{cases} \tag{4.5}$$

being F_{μ_x}, and F_{μ_y} the components of the friction force in the two horizontal directions, and R_{eff} the effective radius of curvature of the bearing as already defined.

The CUKF has been developed in the Matlab/Simulink environment [133].
For all of the tests, the initial state vector is set as $x = [f_{d1}, f_1, f_{d2}, f_2, \mu_{1,0}, \mu_{2,0}]^T = [x_{1,0}, x_{2,0}, x_{3,0}, x_{4,0}, x_{5,0}, x_{6,0}]^T = [0,1,0,1,0,0]^T$ with lower and upper state constraints set as $x_L = [-\infty, 0, -\infty, 0, -\infty, -\infty]^T$ and $x_U = [\infty, 1, \infty, 1, \infty, \infty]^T$, respectively.

The initial friction variation functions (f_1, f_2) state values are initialized to 1, in agreement with the assumption that at the initial time instant, when the isolator is in static conditions, its sliding surfaces are not yet subjected to any variation phenomena ($\mu = \mu(v, N, T)$).
To improve the CUKF estimation quality, the first-time derivatives of the friction variation functions (f_{d1}, f_{d2}) are introduced as additional "degrees of freedom" of the observer design model, basing on the Random Walk model approach [24], and are initialized to 0.

Moreover, the friction coefficients $\mu_{1,0}$ and $\mu_{2,0}$ are initialized to 0, assuming the "a-priori no knowledge" of their initial values (friction coefficients at motion breakaway) in order to demonstrate the CUKF convergence capabilities.

The boundaries [0,1] on the friction variation functions f_1 and f_2 are introduced to avoid a non-physical increase of the friction property during the estimation made through the CUKF, ensuring in this way, the convergence of the estimated data. The three analyses reported hereinafter, named as CSS-1 TEST, CSS-2 TEST, and CSS-3 TEST, are referred to datasets obtained from the described FE analyses.

4.3.1.1. CSS-1 TEST

In this test, a single CSS isolator is analyzed. The anticipated design with $\mu_1 > \mu_2$ is indeed very common in practice when it is necessary to limit the seismic displacement of the isolation system during strong earhtquakes.

In Figure 4.44, the FE time-histories of the average nodal temperatures of the sliding pads of the primary and secondary sliding surface are shown. In agreement with the assigned friction coefficient, the primary sliding surface experiences a substantial temperature rise (up to 165°C) due to frictional heating. The secondary sliding surface is only marginally affected from temperature rise, and its temperature remains nearly constant at about 25 °C. These results are reflected by the different variations of the coefficient of friction at the two sliding surfaces.

Figure 4.45 compares the estimated (CUKF) and the calculated (FEM) time histories of the instantaneous friction coefficients μ_1 and μ_2, and the relevant effective coefficient of friction μ_{eff}. At the primary surface, μ_1 decreases from the initial value of $\mu_{1,Tamb}$ = 0.11 to a minimum value of 0.075 (i.e., -32%) while, at the secondary surface μ_2 remains practically constant at the ambient temprature value of 0.005.

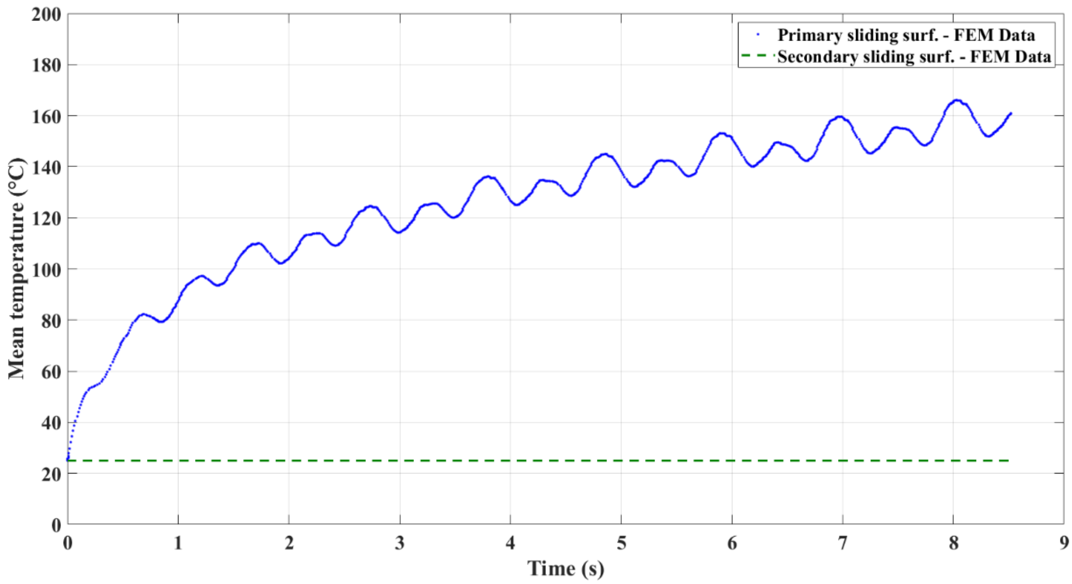

Figure 4.44. Calculated (FEM) mean temperature at the primary and secondary sliding surfaces (CSS-1 TEST).

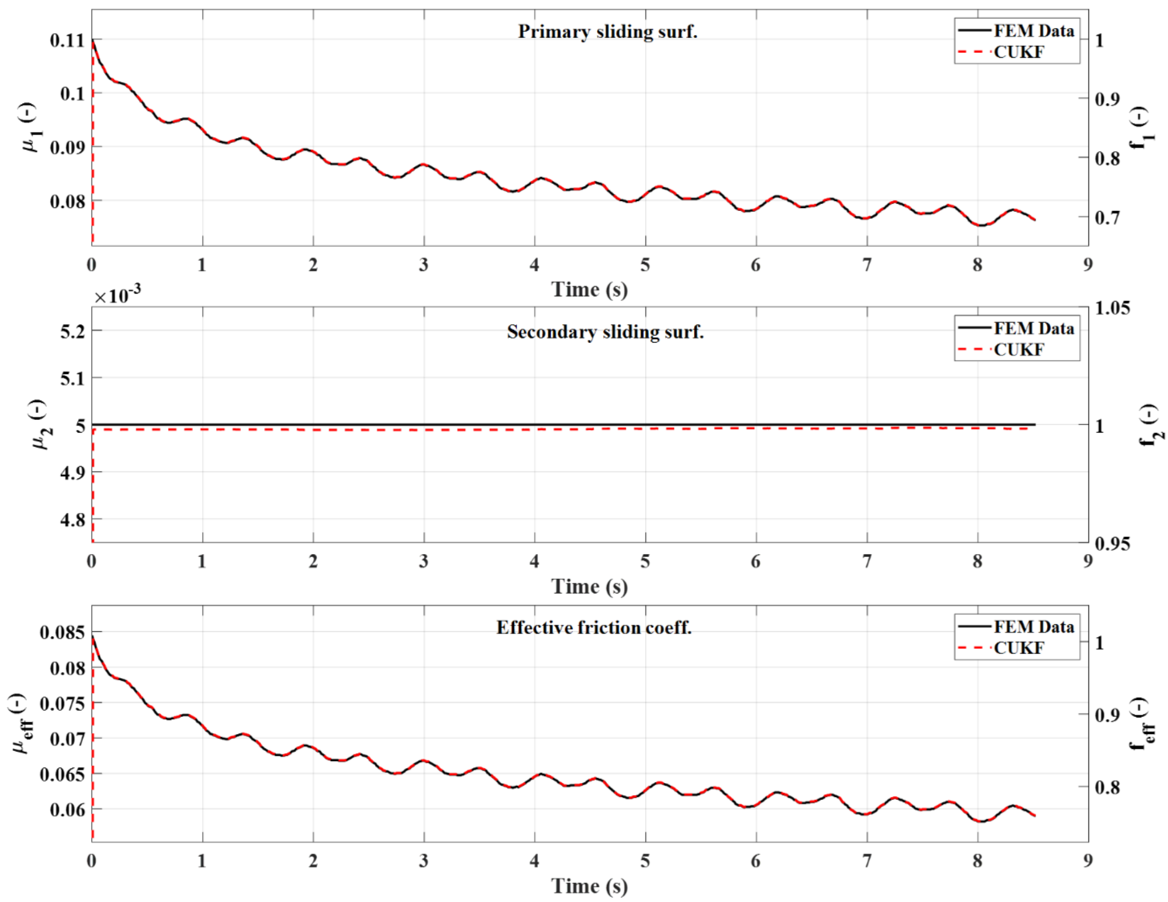

Figure 4.45. Calculated (FEM) and estimated (CUKF) instantaneous coefficients of friction at the primary (μ_1), and secondary sliding surfaces (μ_2), and effective coefficient of friction (μ_{eff}) (CSS-1 TEST).

According to the formulation introduced in Section 3.3, the instantaneous values of the estimated friction coefficient μ_1 and μ_2 are obtained as the product of the initial value of the friction coefficients $\mu_{1,0}$ and $\mu_{2,0}$ at ambient temperature times the time-varying degradation functions f_1 and f_2, i.e. $\mu_1 = \mu_{1,0}\, f_1$ and $\mu_1 = \mu_{2,0}\, f_2$.

At the beginning of the analysis, both $\mu_{1,0}$ and $\mu_{2,0}$ are initialized at 0, assuming total lack of a-priori knowledge. In spite of this, the CUKF instantaneously converges to the “true” values providing an accurate estimate of the initial friction coefficients $\mu_{1,0}$ and $\mu_{2,0}$ ($\mu_{1\_FEM} = 0.11$, $\mu_{1,0} = 0.1094$; $\mu_{2\_FEM} = 0.005$, $\mu_{2,0} = 0.00498$).

Similarly, the RWM method proves to be able to identify the instantaneoys values of the variation functions f_1 and f_2 throughout the considered time window. The constant estimate of μ_2 confirms the capability of the CUKF to identify a steady friction variation function $f_2 \cong 1$ on the secondary surface. The estimate of μ_1 agrees with the time variation on the primary surface during the isolator motion. In conclusion, the RWM method, coupled with the

application of state constraints, provides very fair estimate, avoiding the need of an *a priori* specific analytical model of the friction variation function.
NRMSE values of μ_1, μ_2 and μ_{eff} are reported in Table 4.15 for evaluating the estimation quality.

Table 4.15. NRMSE values for CSS-1 TEST.

Variable name	***NRMSE***
μ_1	0.1087
μ_2	0.0343
μ_{eff}	0.1103

NRMSE values are close to zero, confirming a good estimation quality provided by the proposed CUKF. If NRMSE values are evaluated, avoiding the time window from 0 s to 0.1 s, where the transient is observable, NRMSE is lower by two orders of magnitude.

The comparison between the calculated and the estimated reaction forces in x and y directions is shown in Figure 4.46.

The excellent matching proves the suitability of the CUKF to capture also the hysteretic force-displacement behavior of CSS isolation units.
Moreover, it is worth noting that the obtained force-displacement plots are in agreement with those calculated in a previous study for a CSS isolator under “8-shaped” displacement orbits [135].

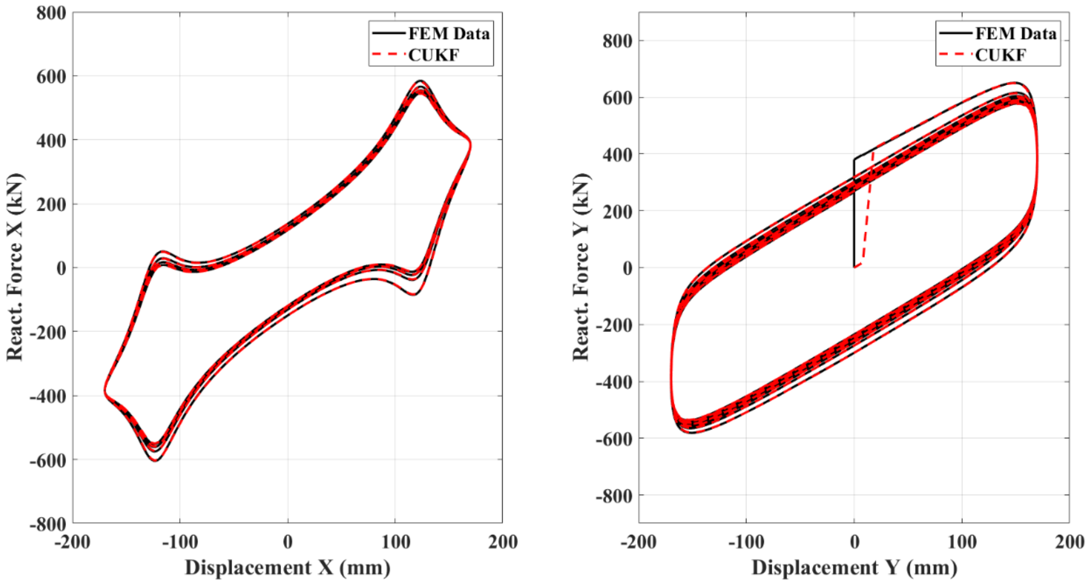

Figure 4.46. Calculated (FEM) and estimated (CUKF) isolator reaction force (F_x, F_y) vs displacement curves (d_x, d_y) (CSS-1 TEST).

4.3.1.2. CSS-2 TEST

In this test, a double CSS is analyzed, with same friction coefficients μ_1 and μ_2 at both sliding surfaces.

FEM-calculated temperature histories are shown in Figure 4.47, while a comparison between estimated (CUKF) and calculated (FEM) friction coefficients μ_1, μ_2, and μ_{eff} are presented in Figure 4.48.

At both surfaces, the average temperature raises from 25 °C to 80 °C leading to the same reduction of the friction coefficient from the initial value of 0.11 at ambient temperature to the minimum one of 0.095 (i.e., -14%).

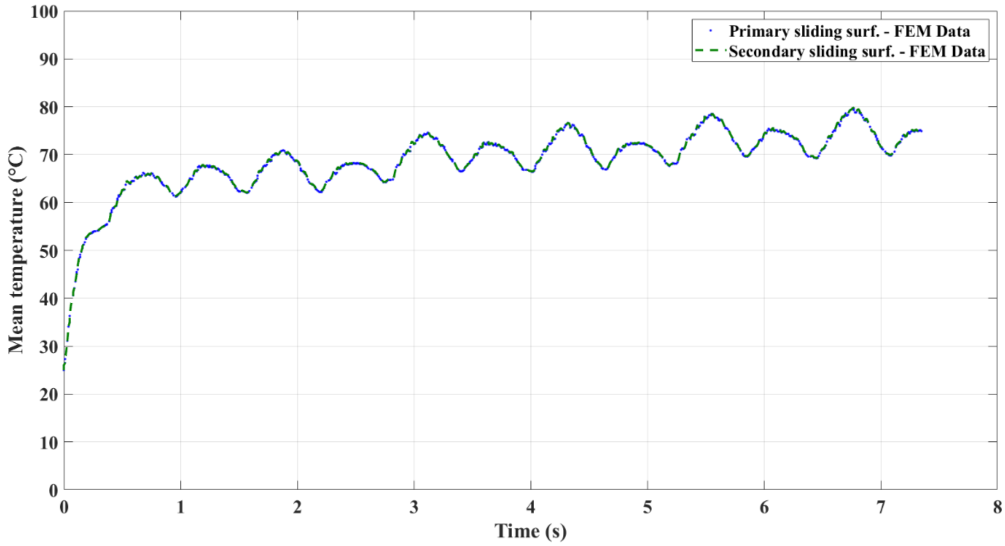

Figure 4.47. Calculated (FEM) mean temperature at the top and bottom sliding surfaces (CSS-2 TEST).

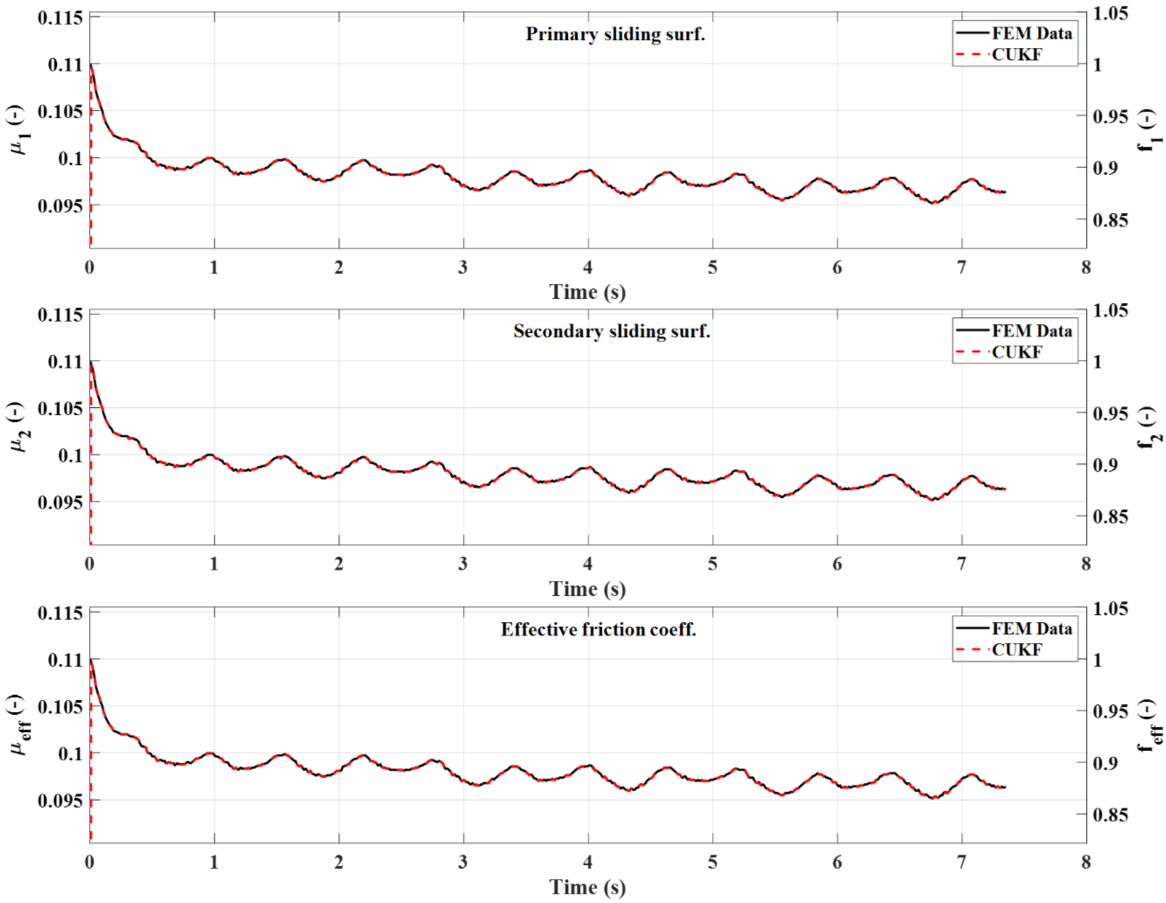

Figure 4.48. Calculated (FEM) and estimated (CUKF) instantaneous coefficients of friction at the top (μ_1), and bottom sliding surfaces (μ_2), and effective coefficient of friction (μ_{eff}) (CSS-2 TEST).

The CUKF correctly estimates the initial friction coefficients $\mu_{1,0}$ and $\mu_{2,0}$ ($\mu_{1\_FEM} = 0.11$, $\mu_{1,0} = 0.1096$; $\mu_{2\_FEM} = 0.11$, $\mu_{2,0} = 0.1096$). The similar histories of the estimated friction coefficients μ_1 and μ_2 confirm the capability of the CUKF to identify the friction variation functions $f_1 = f_2$ from the data collected in tests with imposed lateral displacement. NRMSE values of μ_1, μ_2 and μ_{eff} are reported in Table 4.16 for evaluating the estimation quality.

Table 4.16. NRMSE values for CSS-2 TEST.

Variable name	***NRMSE***
μ_1	0.2727
μ_2	0.2727
μ_{eff}	0.2727

NRMSE values are close to zero, confirming a good estimation quality provided by the proposed CUKF. If NRMSE values are evaluated, avoiding the time window from 0 s to 0.1 s, where the transient is observable, NRMSE is lower by two orders of magnitude.

The estimated (CUKF) reaction forces of the CSS are in good agreement with the FE calculated values in both horizontal directions, as shown in Figure 4.49.

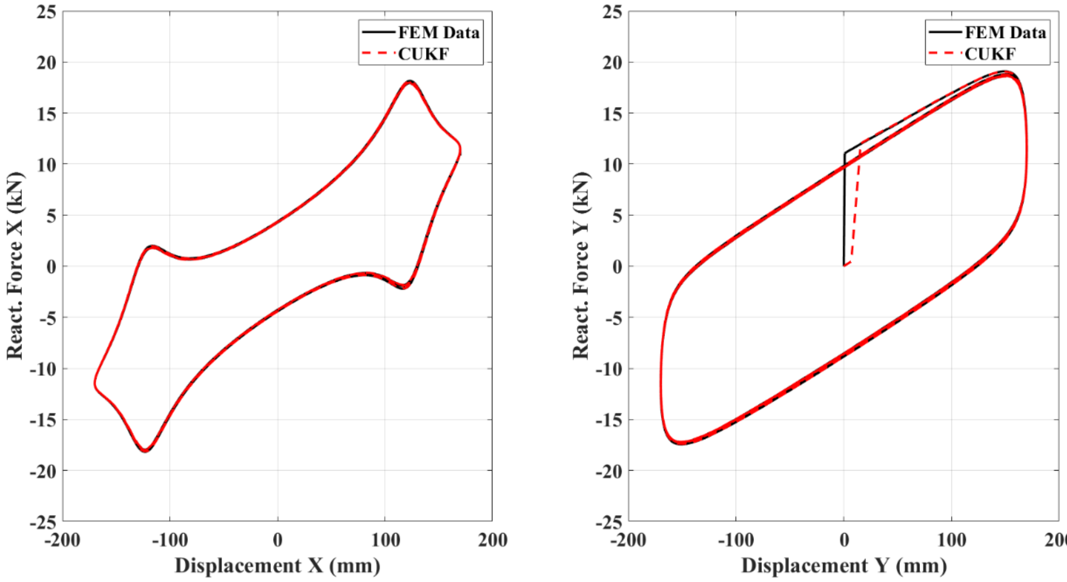

Figure 4.49. Calculated (FEM) and estimated (CUKF) isolator reaction forces (F_x, F_y) VS displacements (d_x, d_y) (CSS-2 TEST).

4.3.1.3. CSS-3 TEST

In this test, a double CSS is analyzed, with the coefficient of friction of the upper sliding surface 20% lower than the coefficient of friction the lower sliding surface. The case study therefore aims at replicating the situation in which the coefficient of friction of a sliding surface is affected from the maximum variation from its design value provided by the European standard [73]. As shown in Figure 4.50, the mean nodal temperature of the lower surface is slightly higher than the mean temperature observed at the upper surface, with maximum values of 63 °C and 58 °C, respectively.

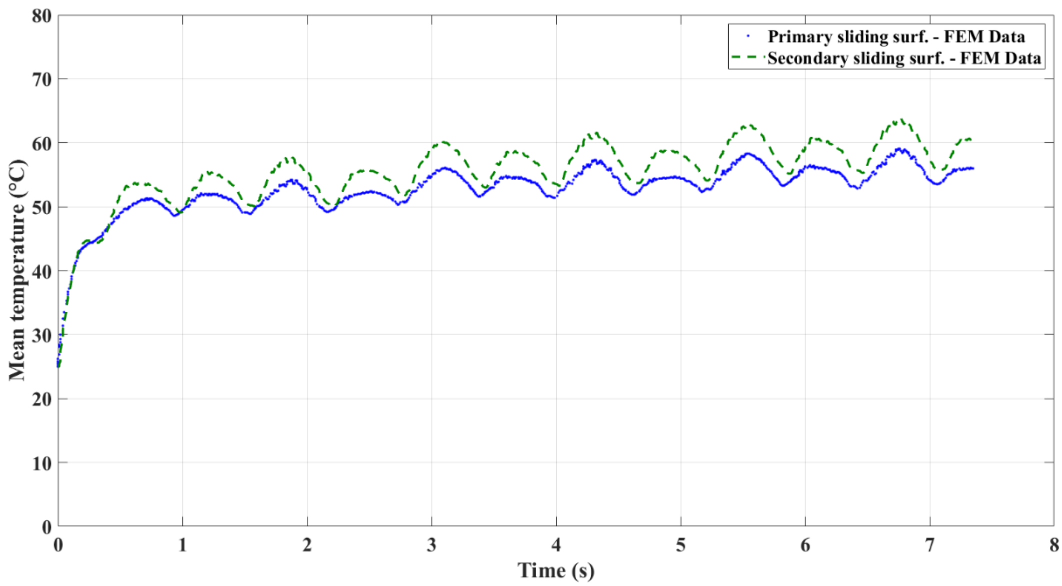

Figure 4.50. Calculated (FEM) mean temperature at the top and bottom sliding surfaces (CSS-3 TEST).

This result is reflected in the variations of the friction coefficients shown in Figure 4.51, where the estimated (CUKF) and numerical (FEM) instantaneous values of the friction coefficients μ_1, μ_2 and μ_{eff} are compared. μ_1 decreases from the initial value of 0.070, at ambient temperature to 0.058 (-17%), while μ_2 decreases from 0.085 to 0.070 (-18%) over the considered observation time window.

Similarly to the previously analysed cases, the CUKF provides accurate and fast estimates of the initial friction coefficients $\mu_{1,0}$ and $\mu_{2,0}$ ($\mu_{1\_FEM} = 0.07$, $\mu_{1s} = 0.0695$; $\mu_{2\_FEM} = 0.085$, $\mu_{2s} = 0.0845$) , converging rapidly from the initialized null values. The different histories of the RWM friction variation functions f_1 and f_2 are consistent with the relevant mean temperature history.

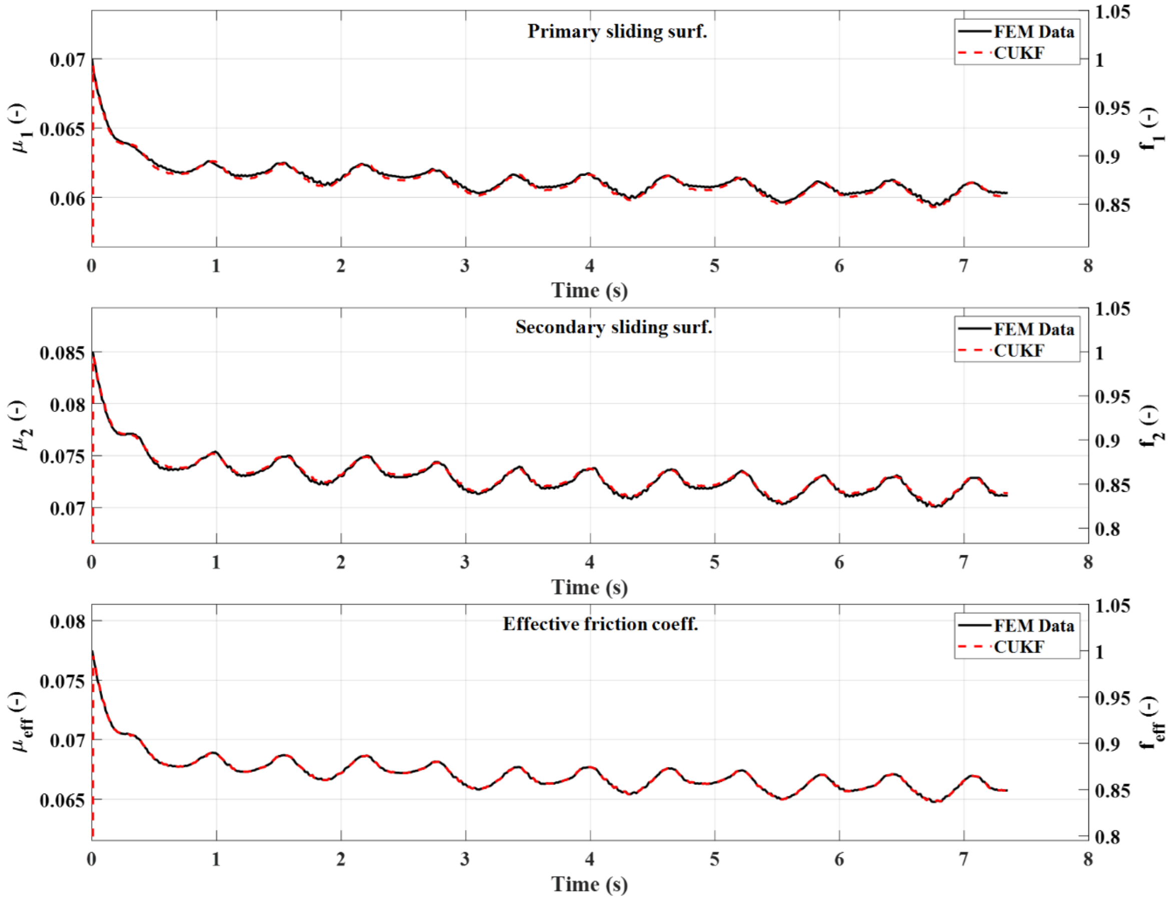

Figure 4.51. Calculated (FEM) and estimated (CUKF) instantaneous coefficients of friction at the top (μ_1), and bottom sliding surfaces (μ_2), and effective coefficient of friction (μ_{eff}) (CSS-3 TEST).

NRMSE values of μ_1, μ_2 and μ_{eff} are reported in Table 4.17 for evaluating the estimation quality.

Table 4.17. NRMSE values for CSS-3 TEST.

Variable name	***NRMSE***
μ_1	0.2440
μ_2	0.2097
μ_{eff}	0.2243

NRMSE values are close to zero, confirming a good estimation quality provided by the proposed CUKF. If NRMSE values are evaluated, avoiding the time window from 0 s to 0.1 s, where the transient is observable, NRMSE is lower by two orders of magnitude, highlighting the ability of the proposed method to identify, with no *a priori* knowledge, a deviation of the friction coefficient of a sliding surface from its design value.

Eventually, the estimated bi-directional resisting forces are practically superimposed to the relevant FE data, as shown in Figure 4.52.

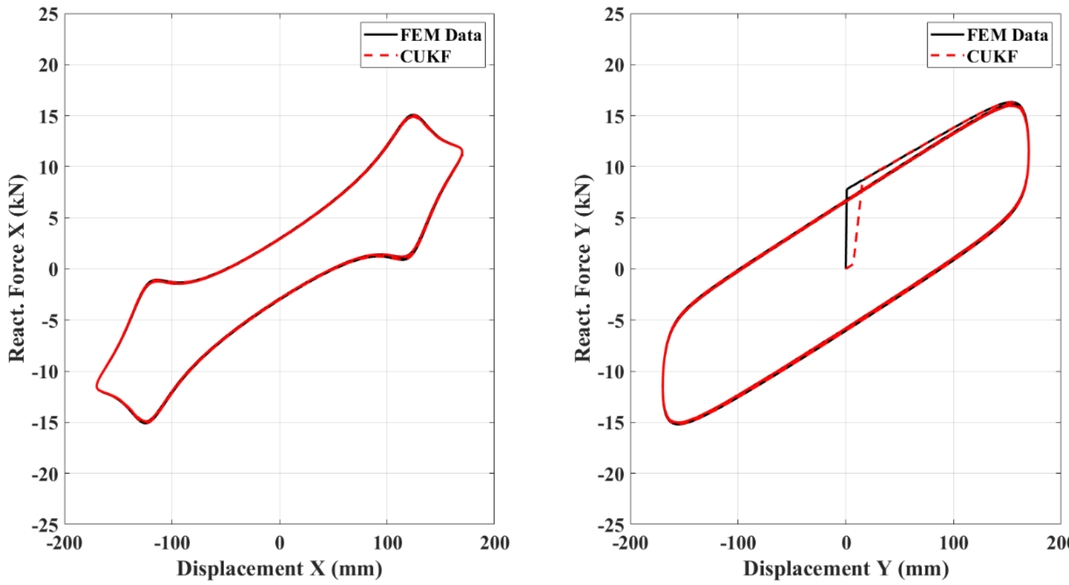

Figure 4.52. Calculated (FEM) and estimated (CUKF) isolator reaction forces (F_x, F_y) VS displacements (d_x, d_y) (CSS-3 TEST).

4.3.2. Experimental validation

The numerically tested CUKF method has been applied to two sets of experimental data.
A full-scale DCSS isolator like the one shown in Figure 1.3b was tested at the Caltrans Seismic Response Modification Device (SRMD) Laboratory at the University of California San Diego (Figure 4.53-left), on a shake-table specifically designed for seismic device testing [137].
The testing machine specifications are (a) longitudinal displacement stroke up to 1.22 m; (b) maximum horizontal and vertical load capacities equal to 9000 kN, and 53400 kN, respectively; (c) peak longitudinal velocity of 1.8 m/s.
The features of the tested CSS isolator are $R_1 = R_2 = 2275$ mm, $h = 250$ mm, $R_{eff} = 4300$ mm, and the sliding pads are made of the same polymeric material.

The bottom concave plate was fixed to the moving table of the testing machine and the top plate to a steel reaction beam. The table was first raised to apply a compression load $N = 6200$ kN, producing a contact pressure $p_{avg} = 38.8$ MPa on the sliding pads.

The shake table was then moved horizontally to reproduce two bi-directional orbits (Figure 4.53-right), namely: (a) a circular (CIRC) orbit, and (b) a cloverleaf (CLOV) orbit. The main test parameters are listed in Table 4.18.

Sufficient time was allowed between the two tests to permit the sliding surfaces of the isolator to cool down to ambient temperature. The friction coefficients μ_1 and μ_2 of the sliding surfacesare expected to vary according to the instantaneous values of the average surface temperature, similarly to the FEM simulations, but also due to the sliding velocity.

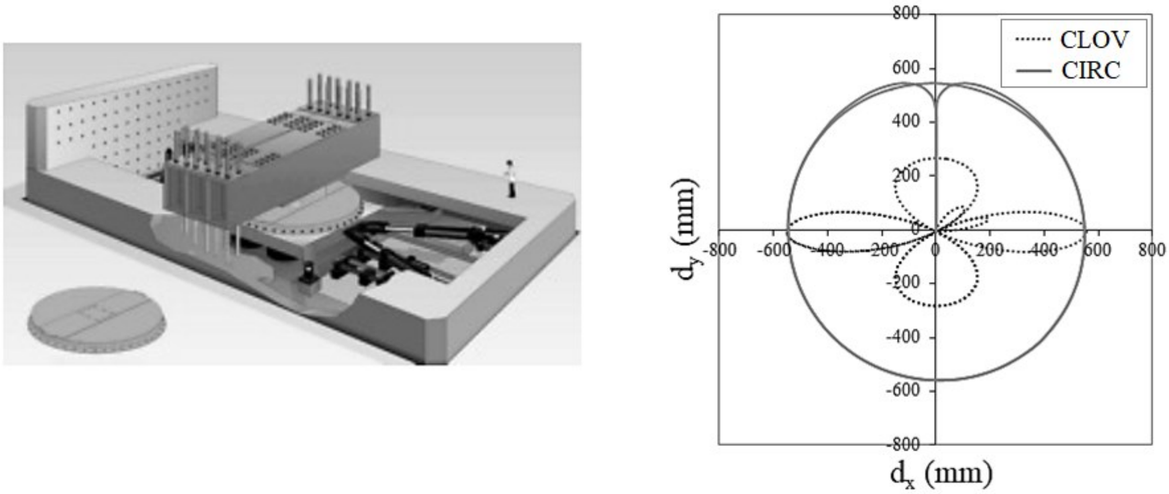

Figure 4.53. Experimental tests on the CSS isolator: schematic representation (adapted from [138]) of the testing machine (left); bi-directional displacement orbits (right).

Table 4.18. Main testing parameters.

Test	Orbit	N [kN]	A_x [mm]	A_y [mm]	$v_{TOT,max}$ [mm/s]
CIRC	circular	6200	550	550	700
CLOV	cloverleaf	6200	550	275	700

N = design axial load; A_x, = displacement amplitude in x direction; A_y = displacement amplitude in y direction; $v_{TOT,max}$ = maximum velocity

4.3.2.1. CIRC TEST

The ability of the CUKF to estimate the coefficient of friction of the individual sliding surfaces of CSS isolators is first assessed by processing the experimental forces F_x and F_y and the displacement histories d_x, and d_y from the CIRC test.

Figure 4.54-a compares the experimental and the estimated (CUKF) values of the effective coefficient of friction μ_{eff}, while Figure 4.54-b provides the estimated friction coefficients μ_1 and μ_2 of the two sliding surfaces. The practical overlapping of the plots demonstrates a similar frictional behavior of the two surfaces, as expected given their nominally identical geometrical and material features, with $\mu_1 \cong \mu_2 \cong \mu_{eff}$. Besides the degradation effect due to frictional heating, captured from the estimator as already illustrated in Section 4.3.1.3, the CUKF also identifies the variation of the friction coefficient induced from changes in the instantaneous sliding velocity.

In agreement with available literature friction models [122], the maximum value $\mu_B = 0.24$ of the coefficient of friction is estimated at the motion breakaway when the velocity is null ($v = 0$ mm/s), while local maxima are observed at $t = 1.7$ s, and $t = 12.0$ s when the sliding velocity has local minima (Figure 4.54-c).

The NRMSE value of μ_{eff} is reported in Table 4.19 for evaluating the estimation quality.

Table 4.19. NRMSE values for CIRC TEST.

Variable name	***NRMSE***
μ_{eff}	0.0435

The NRMSE value is close to zero, confirming a good estimation quality provided by the proposed CUKF. If the NRMSE value is evaluated, avoiding the time window from 0 s to 0.1 s, where the transient is observable, NRMSE is lower by one order of magnitude.

The comparison between the experimental and the estimated bi-directional reaction forces of the CSS is shown in Figure 4.55.

A fair prediction of the frictional forces can be appreciated when the isolators approaches the positions $d_x = 0$, and $d_y = 0$ corresponding to points of maximum sliding velocity (i.e., lowest accelerations and inertia forces) while a certain discrepancy can be noted when the isolator reaches the maximum displacement amplitues where, most likely, very high parasite inertia forces of the testing machine affect the recorded force values.

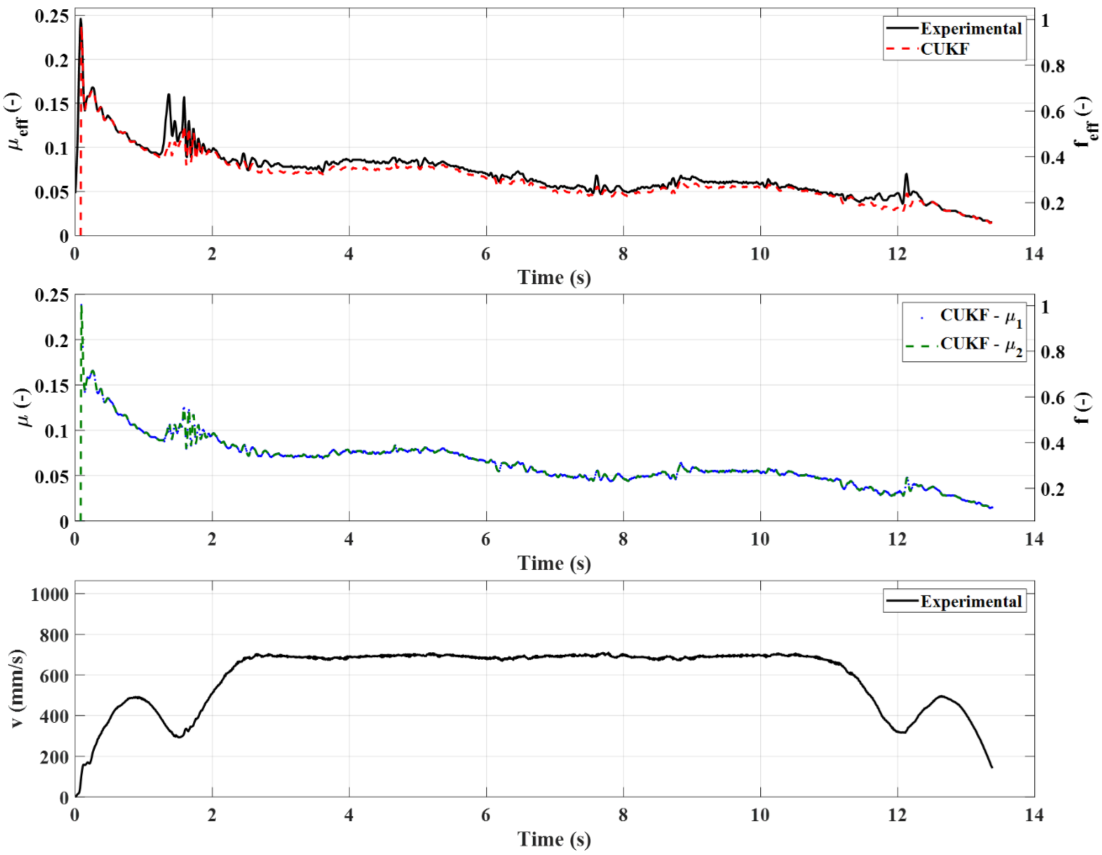

Figure 4.54. Results of CIRC test: (a) comparison between the experimental (assessed through Equation (4.5)) and the estimated (CUKF) values of the effective coefficient of friction (μ_{eff}); (b) friction coefficients predicted by the CUKF at the two sliding surfaces (μ_1, μ_2); (c) recorded instantaneous sliding velocity (v).

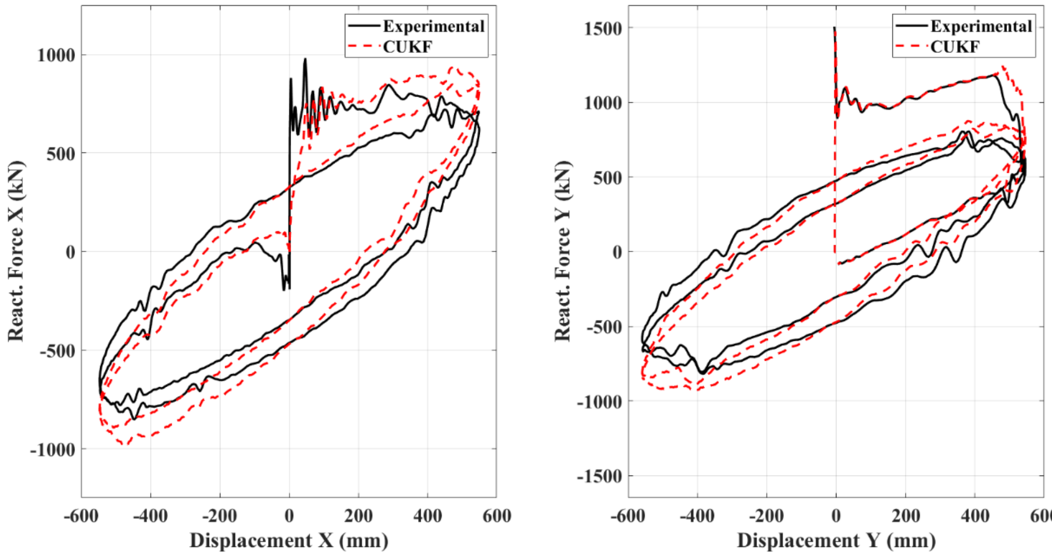

Figure 4.55. Results of CIRC test: experimental and estimated (CUKF) values of CSS reaction forces (F_x, F_y) VS displacements (d_x, d_y).

4.3.2.2. CLOV TEST

The application of the CUKF method to the CLOV test also shows good agreement between experimental and estimated values (Figure 4.56-a) in terms of effective friction coefficient μ_{eff}. Figure 4.56-b shows the friction coefficients estimated at the upper, μ_1, and lower, μ_2, sliding surfaces.

Similarly to the results relevant to the CIRC tests, the experimental and estimated time histories of the effective friction coefficient are again overlapped over the entire time window,. Besides the breakaway maximum value of the friction coefficient ($\mu_B = 0.24$ at $t = 0\ s$, and $v = 0$ mm/s), the CUKF provides accurate estimates of minor peaks of friction coefficients in correspondence of local minima of the recorded sliding velocity (Figure 4.56-c).

The NRMSE value of μ_{eff} is reported in Table 4.20 for evaluating the estimation quality.

Table 4.20. NRMSE values for CLOV TEST.

Variable name	*NRMSE*
μ_{eff}	0.0536

The NRMSE value is close to zero, confirming a good estimation quality provided by the proposed CUKF. If the NRMSE value is evaluated, avoiding the time window from 0 s to 0.1 s, where the transient is observable, NRMSE is lower by one order of magnitude.

The comparison between the experimental and the estimated bi-directional reaction forces of the CSS is shown in Figure 4.57. In the *x* direction a fair prediction of the frictional force can be appreciated throughout the test.

On the contray, a less accurate, altough acceptable, estimate is provided in the *y* direction. The different performance of the CUKF model in predicting the reaction forces in either direction is ascribed to some inaccuracies occurring at high testing velocities in the estimation of the trajectory angle ϑ based on acquired displacement time-histories; as the angle ϑ contributes in different ways to F_x and F_y as per Equation (3.41), larger errors affect on average the force component along the direction of smaller amplitude of the orbit.

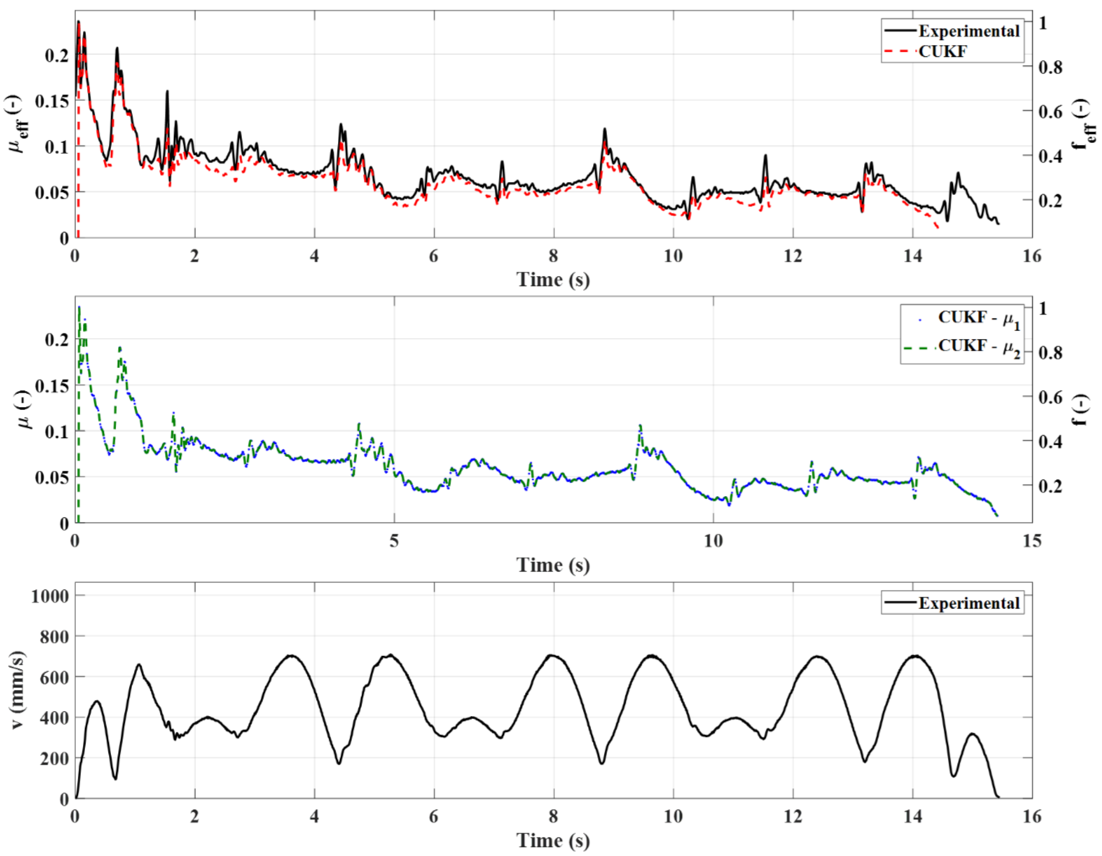

Figure 4.56. (a) Results of CLOV test: comparison between the experimental (assessed through Equation (4.5)) and the estimated (CUKF) values of the effective coefficient of friction (μ_{eff}); (b) friction coefficients predicted by the CUKF at the two sliding surfaces (μ_1, μ_2); (c) recorded instantaneous sliding velocity (v).

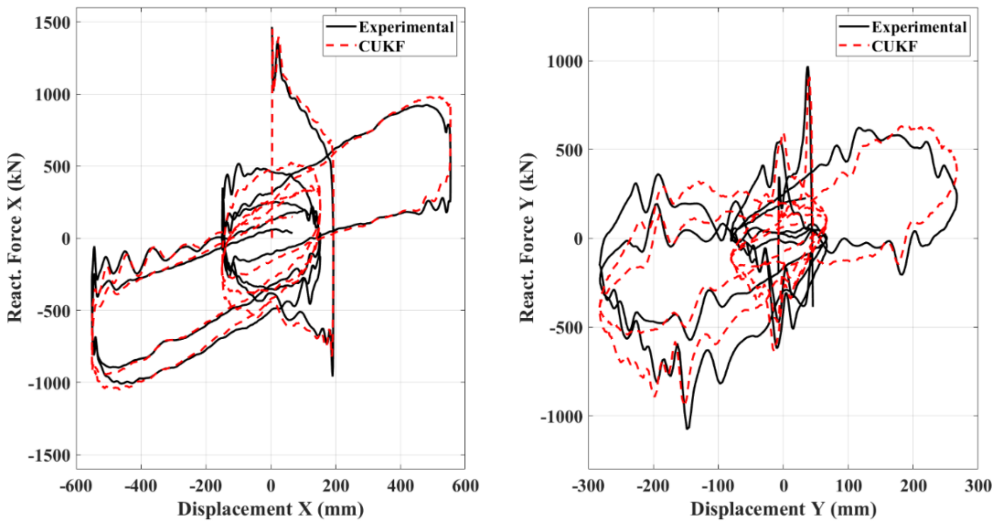

Figure 4.57. Results of CLOV test: experimental and estimated (CUKF) values of CSS reaction forces (F_x, F_y) VS displacements (d_x, d_y).

The proposed approach based on the CUKF coupled with an estimator design model able to identify the frictional behaviour of both surfaces of Curved Surfaces Sliding Isolators is suitable for the characterization of frictional properties related to previously mentioned surfaces and for monitoring their health conditions for avoiding excessive wear and, therefore, failures during work conditions of isolators.

5. CONCLUSIONS AND FUTURE DEVELOPMENTS

In the present Ph.D. thesis, the possibility of applying the model-based approach for monitoring different mechanical systems has been investigated. In particular, nonlinear Kalman Filters have been employed to make condition monitoring of three types of mechanical systems: the railway vehicle, the road vehicle, and Curved Surfaces Sliding Isolators. Estimator design models, functional for obtaining reliable estimation thorough Kalman Filters, have been developed, specifically, for each previously mentioned system to be monitored. Overall, the investigated methodology for monitoring purposes revealed its suitability to be applied in condition-based maintenance operations thanks to the possibility of estimating system state variables and parameters for identifying faults and malfunctioning.

Regarding each of investigated application field, the following final considerations can be deducted:

- **railway field:** a model-based estimation technique based on a Constrained Unscented Kalman Filter (CUKF) for the condition monitoring of anti-yaw suspension components has been proposed. The proposed monitoring technique has been designed by adopting a half-body vehicle model. The estimation of the parameters related to anti-yaw suspension components and wheel-rail contact interactions has been made through a parametric estimation approach and a Random Walk Model technique, respectively, exploiting the augmented state technique. The Random Walk Model technique allows for disengaging the nonlinear estimator from a specific wheel-rail contact model, and track irregularities knowledge is not needed. Two tests have been carried out, with five and three sensors, both in no-fault and fault conditions of anti-yaw dampers. The proposed methodology has been extended through two additional tests carried out with anti-yaw dampers in both no-fault and fault conditions, while the anti-yaw springs have been considered in the no-fault one. Only the five sensors configuration has been employed for these last tests. The estimated results obtained by the proposed technique have been compared with simulated data produced by a more complex and detailed railway vehicle model developed with the SIMPACK software. The obtained results demonstrated the suitability of the CUKF to estimate accurately both the anti-yaw damping and stiffness in different operative conditions, confirming the reliability of this tool for the health condition monitoring purpose of anti-yaw suspension components.

The applicability of constraints to the system state variables gives advantages from the estimation convergence point of view, reducing the estimation error due to the unmodelled effects in the estimator design model. Furthermore, the physical operative limits can be taken into account through the application of state constraints;

- **automotive field:** two different estimation approaches based on the Extended Kalman Filter (EKF) have been proposed to estimate the sideslip angle and for tire-road condition monitoring. In the first one, an estimator design model based on a double-track vehicle model, coupled with a four-parameter Pacejka Magic Formula, has been integrated into the Extended Kalman Filter. In the first one, an estimator design model based on a double-track vehicle model, coupled with a four-parameter Pacejka Magic Formula, has been integrated into the Extended Kalman Filter. Lateral tire-road friction coefficients, related to both sides of the vehicle, have been estimated, and the sideslip angle has been included in the estimation process. Estimations obtained through the EKF have been compared with the dynamical response of a multibody vehicle model developed in the Adams/Car environment. The obtained results confirmed the employability of the proposed approach for improving the performances of active safety systems of vehicles by monitoring changes in tire-road conditions. Despite the advantage of estimating friction coefficients on both sides of a vehicle, the parameters related to the Pacejka Magic Formula must be calibrated through expensive experimental tests and deep offline procedures. Therefore, in the second proposed approach, a single-track vehicle model constituting the estimator design one has been developed to make the EKF able to estimate both lateral tire-road friction and forces with a priori no knowledge of specific tire models, avoiding expensive experimental tests for their characterization. The presented results demonstrated the capability of the EKF to correctly estimate the desired variables capturing, faithfully, the dynamical behaviour of the vehicle in both noisy and non-noisy conditions;

- **seismic engineering field:** an estimation procedure based on the Constrained Unscented Kalman Filter (CUKF) combined with the random walk method (RWM) has been proposed to identify the friction coefficient of the sliding surfaces of single and double CSS isolators based on global response quantities observed in testing. The method uses, as input data, experimental recorded force–displacement time-histories, and provides the estimation of the coefficient of friction at each sliding surface and of its time-dependent variation during bi-directional motions. The methodology has been applied to CSS units comprising only two sliding surfaces, with either equal or different radii of curvature, but it can be extended in principle to isolators with any number of sliding surfaces, such as the DCSS with an internal hinge or the Triple Friction Pendulum System. The main advantage of this approach is the ability to identify the instantaneous friction coefficients without any a-priory information on the properties of the sliding materials and any assumption on the relevant friction behaviour. The method was firstly assessed using bi-directional thermo-mechanical FE simulations, proving its suitability to estimate the friction coefficient activated at the two sliding surfaces of either a single or a double CSS even in case of very different friction levels. Then, the method was tested against experimental data measured in bi-directional tests carried out on a full-scale DCSS isolator. The coupled CUKF- RWM approach demonstrated to be a viable tool for the identification of the friction behaviour of sliding surfaces using only the overall/effective response of the CSS unit (i.e., weighted average of the friction forces developed at the two sliding surfaces) recorded in the prototype/qualification tests required by the Standards. Its potential applications include both the assessment of design as well as quality control purposes.

Future developments will deal with the following purposes:

- further experimental validations of the proposed model-based approach for monitoring mechanical systems;
- possibility of developing embedded solutions for integrating model-based estimators in hardware units for making real-time monitoring of investigated systems functional for condition-based maintenance operations;
- possibility of applying the model-based approach for monitoring purposes to other mechanical and mechatronics systems.

References

[1] Kaiser, I., Strano, S., Terzo, M., & Tordela, C. (2021, January). Anti-yaw damping monitoring of railway secondary suspension through a nonlinear constrained approach integrated with a randomly variable wheel-rail interaction. Mechanical Systems and Signal Processing, 146, 2021, 107040.

[2] I. Kaiser, S. Strano, M. Terzo and C. Tordela, Railway anti-yaw suspension monitoring through a nonlinear constrained estimator, International Journal of Mechanics and Control, Vol. 22, No. 02, pp. 35-42, December 2021.

[3] Lenzo, B., Ottomano, G., Strano, S., Terzo, M., & Tordela, C. (2020, September). A Physical-Based Observer for Vehicle State Estimation and Road Condition Monitoring. In IOP Conference Series: Materials Science and Engineering (Vol. 922, No. 1, p. 012005). IOP Publishing.

[4] Strano, S., Terzo, M., & Tordela, C. (2022, September). A Nonlinear Estimation Approach for Vehicle and Tire-Road Monitoring with No Interaction Modelling. In The International Conference of IFToMM ITALY (pp. 389-396). Springer, Cham.

[5] Gandelli, E., Lomiento, G., Quaglini, V., Strano, S., Terzo, M., & Tordela, C. (2021, December). Estimation of the instantaneous friction coefficients of sliding isolators subjected to bi-directional orbits through a nonlinear state observer. Engineering Structures, 249, 113374.

[6] Gadhave, R., & Vyas, N. S. (2022). Rail-wheel contact forces and track irregularity estimation from on-board accelerometer data. Vehicle System Dynamics, 60(6), 2145-2166.

[7] Ye, Y., Huang, P., & Zhang, Y. (2022). Deep learning-based fault diagnostic network of high-speed train secondary suspension systems for immunity to track irregularities and wheel wear. Railway Engineering Science, 30(1), 96-116.

[8] Ward, C. P., Goodall, R. M., Dixon, R., & Charles, G. A. (2012, July). Adhesion estimation at the wheel–rail interface using advanced model-based filtering. Vehicle System Dynamics, 50(12), 1797-1816.

[9] I. Hussain, T. Mei, Multi Kalman filtering approach for estimation of wheel-rail contact conditions, Proceeding of UKACC International Conference on CONTROL, Coventry, UK, 7-10 September 2010, paper ThC4.2.

[10] C. Ward, R. Goodall, R. Dixon, Creep force estimation at the vehicle wheel-rail interface, Proceedings of 22nd International Symposium on Dynamics of Vehicle on Roads and Tracks, Manchester, UK, 14 – 19 August 2011, paper 13.1.

[11] Charles, G., Goodall, R., & Dixon, R. (2008). Model-based condition monitoring at the wheel–rail interface. Vehicle System Dynamics, 46(S1), 415-430.

[12] P. Li, R. Goodall and V. Kadirkamanathan, Parameter estimation of railway vehicle dynamic model using Rao-Blackwellised particle filter, in: 2003 European Control Conference (ECC), Cambridge, UK, September 2003, pp. 2384–2389.

[13] P. Li, R. Goodall and V. Kadirkamanathan, Estimation of parameters in a linear state space model using a Rao-Blackwellised particle filter, in: IEEE Proceedings - Control Theory and Applications, vol. 151, no. 6, pp. 727–738, 22 Nov. 2004.

[14] Ping Li, Roger Goodall, Paul Weston, Chung Seng Ling, Colin Goodman, Clive Roberts, Estimation of railway vehicle suspension parameters for condition monitoring, Control Eng. Pract. 15 (1) (2007, January) 43–55.

[15] Zhang, Z., Xu, B., Ma, L., & Geng, S. (2014, July). Parameter estimation of a railway vehicle running bogie using extended Kalman filter. In Proceedings of the 33rd Chinese Control Conference (pp. 3393-3398). IEEE.

[16] Zoljic-Beglerovic, S., Stettinger, G., Luber, B., & Horn, M. (2018, September). Railway suspension system fault diagnosis using cubature Kalman filter techniques. IFAC-PapersOnLine, 51(24), 1330-1335.

[17] Lebel, D., Soize, C., Funfschilling, C., & Perrin, G. (2020). High-speed train suspension health monitoring using computational dynamics and acceleration measurements. Vehicle System Dynamics, 58(6), 911-932.

[18] Mathias Jesussek, Katrin Ellermann, Fault Detection and Isolation for a Railway Vehicle by Evaluating Estimation Residuals, Procedia IUTAM, Volume 13, 2015, Pages 14-23, ISSN 2210-9838, https://doi.org/10.1016/j.piutam.2015.01.004.

[19] Strano, S., & Terzo, M. (2019, Febraury). Review on model-based methods for on-board condition monitoring in railway vehicle dynamics. Advances in mechanical engineering, 11(2), 1687814019826795.

[20] H. Tsunashima, H. Mori, Condition monitoring of railway vehicle suspension using adaptive multiple model approach. In: Proceedings of the international conference on control, automation and systems, Gyeonggi-do, South Korea, 27–30 October 2010, pp. 584–589. New York: IEEE.

[21] Y. Hayashi, T. Kojima, H. Tsunashima, et al, Real time fault detection of railway vehicles and tracks, IET Semin, Digest 2006 (2006, November) 20–25.

[22] M. Jesussek, K. Ellermann, Fault detection and isolation for a nonlinear railway vehicle suspension with a hybrid extended Kalman filter, Vehicle Syst. Dyn. 51 (2013, June) 1489–1501.

[23] V.K. Garg, R.V. Dukkipati, Dynamics of Railway Vehicle Systems, Academic Press, Don Millis, ON, Canada, 1984.

[24] Niola, V., Strano, S., Terzo, M. (March 27, 2018). A Random Walk Model Approach for the Wheel-Rail Contact Force Estimation. ASME. J. Dyn. Sys., Meas., Control. July 2018; 140(7): 071016.

[25] Kaiser, I., Strano, S., Terzo, M., & Tordela, C. (2020, September). A Constrained Nonlinear Approach for Monitoring the Railway Anti-yaw Damping. In The International Conference of IFToMM ITALY (pp. 749-757). Springer, Cham.

[26] Salvatore Strano, Mario Terzo, Constrained nonlinear filter for vehicle sideslip angle estimation with no a priori knowledge of tyre characteristics, Control Eng. Pract. 71 (2018, February) 10–17.

[27] Julier, S. J., Uhlmann, J. K., & Durrant-Whyte, H. F. (1995, June). A new approach for filtering nonlinear systems. In Proceedings of 1995 American Control Conference-ACC'95 (Vol. 3, pp. 1628-1632). IEEE.

[28] Julier, S. J. (2002, May). The scaled unscented transformation. In Proceedings of the 2002 American Control Conference (IEEE Cat. No. CH37301) (Vol. 6, pp. 4555-4559). IEEE.

[29] D. Simon, Optimal State Estimation: Kalman, H Infinity, and Nonlinear Approaches, John Wiley and Sons Inc., 2006.

[30] Julier, S., Uhlmann, J., & Durrant-Whyte, H. F. (2000, March). A new method for the nonlinear transformation of means and covariances in filters and estimators. IEEE Transactions on automatic control, 45(3), 477-482.

[31] R. Kandepu, B. Foss, L. Imsland, Applying the unscented Kalman filter for nonlinear state estimation, J. Process Control 18 (7–8) (2008, August–September) 753–768.

[32] Kolås, S., Foss, B. A., & Schei, T. S. (2009, August). Constrained nonlinear state estimation based on the UKF approach. Computers & Chemical Engineering, 33(8), 1386-1401.

[33] Mandela, R. K., Kuppuraj, V., Rengaswamy, R., & Narasimhan, S. (2012, April). Constrained unscented recursive estimator for nonlinear dynamic systems. Journal of Process Control, 22(4), 718-728.

[34] Wu, B., & Wang, T. (2014, December). Model updating with constrained unscented Kalman filter for hybrid testing. Smart structures and systems, 14(6), 1105-1129.

[35] Calabrese, A., Strano, S., & Terzo, M. (2018). Adaptive constrained unscented Kalman filtering for real-time nonlinear structural system identification. Structural Control and Health Monitoring, 25(2), e2084.

[36] Bosch R 2018 Bosch Automotive Handbook 10th ed.

[37] Rajamani, R.: Vehicle Dynamics and Control. Springer, New York (2012). https://doi.org/10.1007/978-1-4614-1433-9.

[38] Ziaukas, Z., Busch, A., & Wielitzka, M. (2021, August). Estimation of Vehicle Side-Slip Angle at Varying Road Friction Coefficients Using a Recurrent Artificial Neural Network. In 2021 IEEE Conference on Control Technology and Applications (CCTA) (pp. 986-991). IEEE.

[39] Song, R., & Fang, Y. (2022, July). Estimation of Vehicle Sideslip Angle based on Modified Sliding Mode Observer and Recurrent Neural Network. In 2022 7th Asia-Pacific Conference on Intelligent Robot Systems (ACIRS) (pp. 135-139). IEEE.

[40] Chindamo, D., Lenzo, B., & Gadola, M. (2018, March). On the vehicle sideslip angle estimation: a literature review of methods, models, and innovations. applied sciences, 8(3), 355.

[41] Sasaki, H., & Nishimaki, T. (2000, January). A side-slip angle estimation using neural network for a wheeled vehicle. SAE transactions, 1026-1031.

[42] Kim, J. (2009, March). Identification of lateral tyre force dynamics using an extended Kalman filter from experimental road test data. Control Engineering Practice, 17(3), 357-367.

[43] Gao, L., Xiong, L., Lin, X., Xia, X., Liu, W., Lu, Y., & Yu, Z. (2019, September). Multi-sensor fusion road friction coefficient estimation during steering with lyapunov method. Sensors, 19(18), 3816.

[44] Ryu, J., & Gerdes, J. C. (2004, June). Integrating inertial sensors with gps for vehicle dynamics control Journal of Dynamic Systems. Measurement, and Control, 243-254.

[45] Zhang, Z., Zheng, L., Wu, H., Zhang, Z., Li, Y., & Liang, Y. (2022). An estimation scheme of road friction coefficient based on novel tyre model and improved SCKF. Vehicle system dynamics, 60(8), 2775-2804.

[46] Hu, J., Rakheja, S., & Zhang, Y. (2020, June). Real-time estimation of tire–road friction coefficient based on lateral vehicle dynamics. Proceedings of the Institution of Mechanical Engineers, Part D: Journal of Automobile Engineering, 234(10-11), 2444-2457.

[47] Wang, L., Pang, H., Zuo, R., & Liu, J. (2022, July). Estimation of vehicle sideslip angle based on strong tracking unscented Kalman filter approach. In 2022 41st Chinese Control Conference (CCC) (pp. 116-121). IEEE.

[48] Farroni, F., Lamberti, R., Mancinelli, N., & Timpone, F. (2018, March). TRIP-ID: A tool for a smart and interactive identification of Magic Formula tyre model parameters from experimental data acquired on track or test rig. Mechanical Systems and Signal Processing, 102, 1-22.

[49] Farroni, F. (2016, May). TRICK-Tire/Road Interaction Characterization & Knowledge-A tool for the evaluation of tire and vehicle performances in outdoor test sessions. Mechanical Systems and Signal Processing, 72, 808-831.

[50] Boulkroune, B., Aalst, S. V., Rademakers, E., Sannen, K., & El Ghouti, N. (2015, November). Vehicle sideslip angle estimation using nonlinear parameter-varying observers. In 2015 International Automatic Control Conference (CACS) (pp. 108-113). IEEE.

[51] Farroni, F., Pasquino, N., Rocca, E., & Timpone, F. (2015, July). A comparison among different methods to estimate vehicle sideslip angle. In Proceedings of the World Congress on Engineering (Vol. 2).

[52] Antonov, S., Fehn, A., & Kugi, A. (2011, March). Unscented Kalman filter for vehicle state estimation. Vehicle System Dynamics, 49(9), 1497-1520.

[53] Doumiati, M., Victorino, A., Lechner, D., Baffet, G., & Charara, A. (2010, October). Observers for vehicle tyre/road forces estimation: experimental validation. Vehicle System Dynamics, 48(11), 1345-1378.

[54] Chen, W., Tan, D., & Zhao, L. (2018, December). Vehicle sideslip angle and road friction estimation using online gradient descent algorithm. IEEE Transactions on Vehicular Technology, 67(12), 11475-11485.

[55] Ray, L. R. (1995, March). Nonlinear state and tire force estimation for advanced vehicle control. IEEE Transactions on Control Systems Technology, 3(1), 117-124.

[56] Strano, S., & Terzo, M. (2017, March). Vehicle sideslip angle estimation via a Riccati equation based nonlinear filter. Meccanica, 52(15), 3513-3529.

[57] Hans B. Pacejka, Tire and Vehicle Dynamics (Third Edition), Butterworth-Heinemann, 2012, ISBN 9780080970165, https://doi.org/10.1016/B978-0-08-097016-5.02001-5.

[58] Tass "Tyre testing," https://www.tassinternational.com/tyre-testing.

[59] Kelly, J. M., Naeim, F. (1999). Design of seismic isolated structures: from theory to practice. Germania: Wiley.

[60] Eröz, M., & DesRoches, R. (2013, May). A comparative assessment of sliding and elastomeric seismic isolation in a typical multi-span bridge. Journal of Earthquake Engineering, 17(5), 637-657.

[61] Zayas, V. A., Low, S. S., & Mahin, S. A. (1990, May). A simple pendulum technique for achieving seismic isolation. Earthquake spectra, 6(2), 317-333.

[62] Tsopelas, P., Constantinou, M. C., Kim, Y. S., & Okamoto, S. (1996, January). Experimental study of FPS system in bridge seismic isolation. Earthquake engineering & structural dynamics, 25(1), 65-78.

[63] Fenz, D. M., & Constantinou, M. C. (2006, June). Behaviour of the double concave friction pendulum bearing. Earthquake engineering & structural dynamics, 35(11), 1403-1424.

[64] Constantinou, M. C. (2004, October). Friction Pendulum double concave bearing. NEES report. Available at: http://nees.buffalo.edu/dec304/FP-DC%20Report-DEMO.pdf.

[65] Kim, Y. S., & Yun, C. B. (2005). Analysis and design of double friction pendulum systems for seismic isolation. In The Second International Conference on Structural Health Monitoring of Intelligent Infrastructure.

[66] Jangid, R. S. (1997, February). Response of pure-friction sliding structures to bi-directional harmonic ground motion. Engineering Structures, 19(2), 97-104.

[67] Ponzo, F. C., Di Cesare, A., Leccese, G., & Nigro, D. (2017, April). Shake table testing on restoring capability of double concave friction pendulum seismic isolation systems. Earthquake Engineering & Structural Dynamics, 46(14), 2337-2353.

[68] Quaglini, V., Gandelli, E., & Dubini, P. (2017). Experimental investigation of the re-centring capability of curved surface sliders. Structural Control and Health Monitoring, 24(2), e1870.

[69] Quaglini, V., Gandelli, E., Dubini, P., & Limongelli, M. P. (2017, May). Total displacement of curved surface sliders under nonseismic and seismic actions: A parametric study. Structural Control and Health Monitoring, 24(12), e2031.

[70] Katsaras, C. P., Panagiotakos, T. B., & Kolias, B. (2008, March). Restoring capability of bilinear hysteretic seismic isolation systems. Earthquake engineering & structural dynamics, 37(4), 557-575.

[71] American Society of Civil Engineers. (2017, June). Minimum design loads and associated criteria for buildings and other structures. American Society of Civil Engineers.

[72] American Association of State Highway and Transportation Officials (AASHTO). Guide Specification for Seismic Isolation Design, Washington D.C.; 1999.

[73] European Standard EN 15129. Anti-seismic devices, CEN, Bruxelles; 2009.

[74] Quaglini, V., Dubini, P., & Poggi, C. (2012). Experimental assessment of sliding materials for seismic isolation systems. Bulletin of Earthquake Engineering, 10(2), 717-740.

[75] Kumar, M., Whittaker, A. S., & Constantinou, M. C. (2015). Characterizing friction in sliding isolation bearings. Earthquake Engineering & Structural Dynamics, 44(9), 1409-1425.

[76] Sarlis, A. A., & Constantinou, M. C. (2016, April). A model of triple friction pendulum bearing for general geometric and frictional parameters. Earthquake Engineering & Structural Dynamics, 45(11), 1837-1853.

[77] Calabrese, A., Gandelli, E., Quaglini, V., Strano, S., Terzo, M., & Tordela, C. (2021, January). Monitoring of hysteretic friction degradation of curved surface sliders through a nonlinear constrained estimator. Engineering Structures, 226, 111371.

[78] Calabrese, A., Quaglini, V., Strano, S., & Terzo, M. (2020). Online estimation of the friction coefficient in sliding isolators. Structural Control and Health Monitoring, 27(3), e2459.

[79] Jangid, R. S. (1996, November). Seismic response of sliding structures to bidirectional earthquake excitation. Earthquake engineering & structural dynamics, 25(11), 1301-1306.

[80] Rao, P. B., & Jangid, R. S. (2001, January). Performance of sliding systems under near-fault motions. Nuclear Engineering and Design, 203(2-3), 259-272.

[81] Wang, D., Yu, M., Low, C. B., & Arogeti, S. (2013). Model-based health monitoring of hybrid systems (pp. 119-122). New York: Springer.

[82] J. Lee, J. Ni, D. Djurdjanovic, H. Qiu, Intelligent prognostics tools and e-maintenance. Comput. Ind. 57(6), 476–489 (2006, August).

[83] Iwnicki S., Handbook of Railway Vehicle Dynamics, Second Edition. (2019). United States: CRC Press.

[84] J.H. Luo, M. Namburu, K.R. Pattipati, L. Qiao, S. Chigusa, Integrated model-based and datadriven diagnosis of automotive antilock braking systems. IEEE Trans. Syst. Man Cybern. A Syst. Hum. 40(2), 321–336 (2010, March).

[85] A.K. Samantaray, B. Ould Bouamama, Model-Based Process Supervision: A Bond Graph Approach (Springer, London, 2008).

[86] S.X.Ding, Model-Based Fault Diagnosis Techniques: Design Schemes, Algorithms, and Tools (Springer, Berlin, 2008).

[87] C. Ghiaus, Fault diagnosis of air conditioning systems based on qualitative bond graph. Energy Build. 30(3), 221–232 (1999, August).

[88] Kuipers, B. (1986, September). Qualitative simulation. Artificial intelligence, 29(3), 289-338.

[89] Kuipers, B. (1987, May). Qualitative simulation as causal explanation. IEEE Transactions on Systems, Man, and Cybernetics, 17(3), 432-444.

[90] H.T. Ng, Model-based multiple fault diagnosis of time-varying, continuous physical devices. In the Sixth Conference on Artificial Intelligence Applications, vol. 1, May 1990, pp. 9–15.

[91] S. Subramanian, R. J. Mooney, Qualitative multiple-fault diagnosis of continuous dynamic systems using behavioral modes. In the 13th National Conference on, Artificial Intelligence, August 1996, pp. 965–970.

[92] Shen, Q., & Leitch, R. R. (1992, August). Qualitative model based of continuous dynamic systems. In Proceedings of the First International Conference on Intelligent Systems Engineering (pp. 147-152).

[93] E.E. Hurdle, L.M. Bartlett, J.D. Andrews, System fault diagnostics using fault tree analysis. J. Risk Reliab., Part O (Proc. IMechE) 221(1), 43–55 (2007, April).

[94] M.G.M. Madden, P.J. Nolan, Monitoring and diagnosis of multiple incipient faults using fault tree induction. IEE Proc.-Control Theory Appl. 146(2), 204–212 (1999, March).

[95] V. Venkatasubramanian, R. Rengaswamy, K. Yin, S.N. Kavuri, A review of process fault detection and diagnosis: part I: quantitative model-based methods. Comput. Chem. Eng. 27(3), 293–311 (2003, March).

[96] S. Xia, D.A. Linkens, S. Bennette, Automatic modeling and analysis of dynamical physical systems using qualitative reasoning and bond graphs. Intell. Syst. Eng. 2(4), 201–212 (1993).

[97] Linkens, D. A., & Wang, H. (1994, March). Fault diagnosis based on a qualitative bond graph model, with emphasis on fault localisation. In 1994 International Conference on Control-Control'94. (Vol. 2, pp. 1329-1334). IET.

[98] J. Chen, R. Patton, Robust Model-Based Fault Diagnosis for Dynamic Systems (Kluwer Academic Publishers, Boston, 1999).

[99] S. Ehsan, K. Khashayar, Fault Diagnosis of Nonlinear Systems Using a Hybrid Approach (Springer, New York, 2009).

[100] H. Hammouri, M. Kinnaert, E.H. El Yaagoubi, Observer-based approach to fault detection and isolation for nonlinear systems. IEEE Trans. Autom. Control 44(10), 1879–1884 (1999, October).

[101] X. Ding, P.M. Frank, An adaptive observer-based fault detection scheme for nonlinear systems. In Proceedings of the 12th IFAC World Congress, Sydney, Australia, pp. 63–68, (1993, July).

[102] C. Edwards, S.K. Spurgeon, R.J. Patton, Sliding mode observers for fault detection and isolation. Automatica 36(4), 541–553 (2000, April).

[103] C.P. Tan, C. Edwards, Robust fault reconstruction in uncertain linear systems using multiple sliding mode observers in cascade. IEEE Trans. Autom. Control 55(4), 855–867 (2010, April).

[104] K.Y. Ng, C.P. Tan, C. Edwards,Y.C.Kuang, New results in robust actuator fault reconstruction in linear uncertain systems using sliding mode observers. Int. J. Robust Nonlinear Control 17(14), 1294–1319 (2007, February).

[105] A. Alessandri, M. Caccia, G. Veruggio, Fault detection of actuator faults in unmanned underwater vehicles. Control Eng. Pract. 7(3), 357–368 (1999, March).

[106] J. Sanjay, A new fast converging Kalman filter for sensor fault detection and isolation. Sens. Rev. 30(3), 219–224 (2010, June).

[107] Isermann, R. (1993, July). Fault diagnosis of machines via parameter estimation and knowledge processing—tutorial paper. Automatica, 29(4), 815-835.

[108] I.Hwang, S. Kim,Y. Kim, C.E. Seah, A survey of fault detection, isolation, and reconfiguration methods. IEEE Trans. Control Syst. Technol. 18(3), 636–653 (2010, May).

[109] Chen, J., Patton, R. J., & Zhang, H. Y. (1996). Design of unknown input observers and robust fault detection filters. International Journal of control, 63(1), 85-105..

[110] S.F. Lin,A.P.Wang, Design of observers with unknown inputs using eigenstructure assignment. Int. J. Syst. Sci. 31(6), 705–711 (2000).

[111] D.T. Horak, Failure detection in dynamic systems with modelling errors. J. Guidance Control Dyn. 131(6), 508–516 (1998).

[112] M.A. Djeziri, R. Merzouki, B. Ould-Bouamama, G. Dauphin-Tanguy, Robust fault diagnosis by using bond graph approach. IEEE/ASME Trans. Mechatron. 12(6), 599–611 (2007, December)

[113] Z. Shi, F. Gu, B. Lennox, A.D. Ball, The development of an adaptive threshold for model-based fault detection of a nonlinear electro-hydraulic system. Control Eng. Pract. 13(11), 1357–1367 (2005, November).

[114] A.K.S. Jardine, D. Lin, D. Banjevic, A review on machinery diagnostics and prognostics implementing condition-based maintenance. Mech. Syst. Signal Process. 20(7), 1483–1510 (2006, October).

[115] Kaiser, I., Poll, G., Voss, G., & Vinolas, J. (2019). The impact of structural flexibilities of wheelsets and rails on the hunting behaviour of a railway vehicle. Vehicle system dynamics, 57(4), 564-594.

[116] Zong, L. H., Gong, X. L., Xuan, S. H., & Guo, C. Y. (2013, January). Semi-active H∞ control of high-speed railway vehicle suspension with magnetorheological dampers. Vehicle System Dynamics, 51(5), 600-626.

[117] S. Iwnicki, Manchester benchmarks for rail vehicle simulation, Veh. Syst. Dyn. 30 (3–4) (1998) 295–313, https://doi.org/10.1080/00423119808969454.

[118] European Railway Research Institute, ERRI B 176/DT 290, B 176 / 3 Benchmark Problem – Results and Assessment, Utrecht 1993.

[119] Simulia, 2019, Multi-Body Simulation Software, Simulia, https://www.3ds.com/products-services/simulia/training/course-descriptions/simpack-rail/.

[120] Guiggiani, M. (2014). The science of vehicle dynamics. Pisa, Italy: Springer Netherlands, 15.

[121] MSC: Adams Car. https://www.mscsoftware.com/product/adams-car

[122] Lomiento G, Bonessio N, Benzoni G. Concave sliding isolator's performance under multi-directional excitation. Ingegneria Sismica 2013;30(3):17–32.

[123] Lomiento, G., Bonessio, N., & Benzoni, G. (2013, July). Concave sliding isolator's performance under multi-directional excitation. Ingegneria Sismica, 30(3), 17-32.

[124] Gandelli, E., Penati, M., Quaglini, V., Lomiento, G., Miglio, E., & Benzoni, G. M. (2019, April). A novel OpenSees element for single curved surface sliding isolators. Soil Dynamics and Earthquake Engineering, 119, 433-453.

[125] Peng, Y., & Huang, T. (2019, July). Sliding implant-magnetic bearing for adaptive seismic mitigation of base-isolated structures. Structural Control and Health Monitoring, 26(10), e2431.

[126] Peng, Y., Huang, T., & Chen, J. (2020, May). Experimental study of seismic isolated structures with sliding implant-magnetic bearings. Journal of Earthquake Engineering, 26(5), 2514-2545.

[127] Gandelli E. (2017, March). Doctoral dissertation "Advanced tools for the design of sliding isolation systems for seismic-retrofitting of hospitals". Italy: University Politecnico di Milano.

[128] Mendenhall, W.M., & Sincich, T.L. (2016). Statistics for Engineering and the Sciences (6th ed.). Chapman and Hall/CRC. https://doi.org/10.1201/b19628.

[129] Abaqus 2019 Documentation, Dassault Systemes Simulia Corp., Providence.

[130] Strano, S., & Terzo, M. (2018, May). On the real-time estimation of the wheel-rail contact force by means of a new nonlinear estimator design model. Mechanical Systems and Signal Processing, 105, 391-403.

[131] Bosso, N., & Zampieri, N. (2020). Numerical stability of co-simulation approaches to evaluate wheel profile evolution due to wear. International Journal of Rail Transportation, 8(2), 159-179.

[132] Bruni, S., Vinolas, J., Berg, M., Polach, O., & Stichel, S. (2011, June). Modelling of suspension components in a rail vehicle dynamics context. Vehicle system dynamics, 49(7), 1021-1072.

[133] The Math Works, Inc. MATLAB. Version 2020b, The Math Works, Inc.; 2020. Computer Software.

[134] Quaglini, V., Bocciarelli, M., Gandelli, E., & Dubini, P. (2014, May). Numerical assessment of frictional heating in sliding bearings for seismic isolation. Journal of Earthquake Engineering, 18(8), 1198-1216.

[135] Quaglini V, Gandelli E, Dubini P. Numerical investigation of curved surface sliders under bidirectional orbits. Ingegneria Sismica - Int J Earthquake Eng 2019;2019 (2).

[136] Sarlis AA, Constantinou MC. Model of Triple Friction Pendulum Bearing for General Geometric and Frictional Parameters and for Uplift Conditions. Report No. MCEER-13-0010. Buffalo (NY): Multidisciplinary Center for Earthquake Engineering Research; 2013.

[137] Benzoni G, Seible F. (1998, May). Design of The Caltrans Seismic Response Modification Device (SRMD) Test Facility. USA – ITALY Workshop on Protective Systems. Report No. MCEER-98-0015. Buffalo, New York City: Multidisciplinary Center for Earthquake Engineering Research.

[138] Structural Engineering, UC San Diego, https://structures.ucsd.edu/facilities/laboratory-listing/srmd.